APL Photonics

RESEARCH ARTICLE | SEPTEMBER 21 2023

Terahertz integration platforms using substrateless all-silicon microstructures

Daniel Headland ; Masayuki Fujita ; Guillermo Carpintero ; Tadao Nagatsuma ; Withawat Withayachumnankul

Check for updates

APL Photonics 8, 091101 (2023)
https://doi.org/10.1063/5.0158350
CHORUS

View Online
Export Citation
CrossMark

Articles You May Be Interested In

Midinfrared surface plasmon sensor based on a substrateless metal mesh

Appl. Phys. Lett. (February 2011)

Pronounced field emission from vertically aligned carbon nanotube blocks and bundles

J. Vac. Sci. Technol. B (January 2011)

DNA-binding protein searches for its target: Non-monotonic dependence of the search time on the density of roadblocks bound on the DNA chain

J. Chem. Phys. (March 2015)

27 October 2023 05:17:16

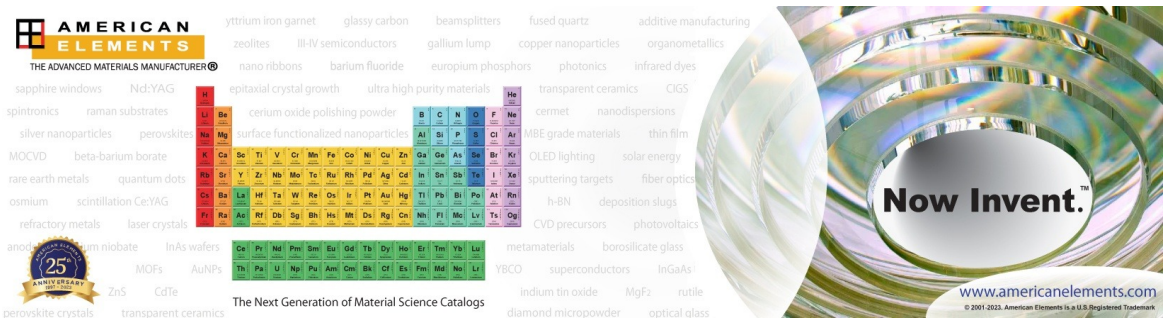

AIP Publishing

Terahertz integration platforms using substrateless all-silicon microstructures

Cite as: APL Photon. 8, 091101 (2023); doi: 10.1063/5.0158350
Submitted: 16 May 2023 • Accepted: 28 August 2023 •
Published Online: 21 September 2023

View Online Export Citation CrossMark

Daniel Headland,[1,a)] Masayuki Fujita,[2] Guillermo Carpintero,[1] Tadao Nagatsuma,[2] and Withawat Withayachumnankul[3]

AFFILIATIONS

[1] Department of Electronic Technology, Universidad Carlos III de Madrid, Madrid 28911, Spain
[2] Graduate School of Engineering Science, Osaka University, Osaka 560-8531, Japan
[3] Terahertz Engineering Laboratory, The University of Adelaide, South Australia 5005, Australia

[a)] **Author to whom correspondence should be addressed:** dheadlan@ing.uc3m.es

ABSTRACT

The absence of a suitable standard device platform for terahertz waves is currently a major roadblock that is inhibiting the widespread adoption and exploitation of terahertz technology. As a consequence, terahertz-range devices and systems are generally an *ad hoc* combination of several different heterogeneous technologies and fields of study, which serves perfectly well for a once-off experimental demonstration or proof-of-concept, but is not readily adapted to real-world use case scenarios. In contrast, establishing a common platform would allow us to consolidate our design efforts, define a well-defined scope of specialization for "terahertz engineering," and to finally move beyond the disconnected efforts that have characterized the past decades. This tutorial will present arguments that nominate substrateless all-silicon microstructures as the most promising candidate due to the low loss of high-resistivity float-zone intrinsic silicon, the compactness of high-contrast dielectric waveguides, the designability of lattice structures, such as effective medium and photonic crystal, physical rigidity, ease and low cost of manufacture using deep-reactive ion etching, and the versatility of the many diverse functional devices and systems that may be integrated. We will present an overview of the historical development of the various constituents of this technology, compare and contrast different approaches in detail, and briefly describe relevant aspects of electromagnetic theory, which we hope will be of assistance.

© 2023 Author(s). All article content, except where otherwise noted, is licensed under a Creative Commons Attribution (CC BY) license (http://creativecommons.org/licenses/by/4.0/). https://doi.org/10.1063/5.0158350

27 October 2023 05:17:16

I. INTRODUCTION AND BACKGROUND

Global demand for wireless data traffic has grown monotonically over the past few decades,[1] owing to the combination of increasing mobile internet access with greater interest in data-intensive services.[2] However, this increase cannot be supported indefinitely using current technologies. Any given wireless communications technology is characterized by its air interface, i.e., the physical medium over which the transmission of information occurs, and at the time of writing, all of our mobile phones employ the microwave and lower millimeter-wave ranges of the electromagnetic spectrum for this purpose. As a consequence, a very large number of users must compete for limited spectrum resources, spurring a considerable amount of research effort into strategies for network congestion mitigation.[3] In the presence of noise, however, there are fundamental limitations to the achievable data throughput with a given fixed bandwidth allocation,[4] and so continued traffic growth must ultimately demand broader available spectrum. It is therefore necessary to explore higher-frequency alternatives in order to meet the future demand, and it is for this reason that frequency allocations are increasing above 100 GHz[5] with the express purpose of catering to the future 6G communications standard. Higher frequencies are envisaged as a means to ease congestion in both air-access networks and backhaul networks alike,[6,7] the latter being enhanced by the prospect of airborne nodes in cases where it is not possible to install a physical cable.[8] In other words, relevant standards committees are gradually turning their attention toward the terahertz range, which is usually defined as the span from 100 GHz to 10 THz. This portion of the electromagnetic spectrum, situated between the microwave and optical ranges, offers extremely wide untapped spectral bandwidth

© Author(s) 2023

that holds significant potential for high-speed wireless communications applications using point-to-point line of sight links between fixed nodes.[9–11]

The viability of high-speed terahertz communications has been validated by a series of experimental demonstrations over the past decade or so. Given that there have been several excellent reviews on the topic,[9–13] only a brief summary is warranted here. The majority of noteworthy demonstrations of terahertz-range communications have utilized carrier frequencies below 500 GHz, with early demonstrations of more than 10 Gbit/s taking place at 300 GHz,[14] and more-gradual adoption in the vicinity of 400 GHz,[15–17] offering single-channel data rates in excess of 100 Gbit/s over distances up to ~10 m. For longer-range transmissions, i.e., over a 100–500-m distance, and with data rates of 50–115 Gbit/s, 300 GHz remains the most popular choice of carrier frequency[18–20] due to higher available power and an atmospheric window. Lower frequencies in the vicinity of 200 GHz are incidentally also receiving attention for similar reasons.[21,22] Conversely, carriers above 500 GHz are limited to data rates below ~30 Gbit/s,[23–26] typically over a distance of centimeters, and at ~1 THz, only basic demonstrations have thus-far been achieved.[27,28] The advantage of lower terahertz frequencies is also supported by link budget analysis[29] that has shown that frequencies in the vicinity of 300 GHz can support 0.3–0.9 Tbit/s for 1-km links, but this falls to less than 1 Gbit/s for links operating from 500 GHz to 1 THz—even if transmit power is kept constant with respect to frequency. Future extension in distance and channel capacity is therefore contingent upon the existence of improved high-power sources and highly efficient devices and systems. Real-world adoption of terahertz-range communications technology will therefore begin at the lower end of the spectrum, and then operation frequencies will be progressively raised, thereby mirroring the trajectory of research advancement. This translation from a laboratory setting toward end-user technologies will require efficient, compact, hand-held systems that can be produced affordably and in large volumes.

Despite the great need and demonstrated potential, the terahertz range is currently lacking in commercially viable real-world applications due to technical challenges, chief among them being signal-to-noise issues due to high losses in existing transmission lines and connectors, as well as significant free-space path losses, and low available power.[30] Second, there is also a lack of a purpose-built integration platform for terahertz waves, and as a result, thorough understanding of a given terahertz experimental setup or demonstration generally requires unorthodox *ad hoc* combinations of several different fields of expertise, making further advancements and innovations challenging. In contrast, a standardized terahertz integration platform would allow developmental and design effort to be consolidated into standard libraries of optimized functional components. Exploration of this possibility is the main subject of this article.

The term "integration" is essentially a guiding principle for streamlined design and manufacture that enables us to build a system through the interconnection of different standard functional building blocks that are fabricated simultaneously on a common semiconductor substrate. This concept was initially pioneered by the electronics industry[31] and was a key enabling factor in the great market penetration of digital electronics, as well as the ubiquity of personal computers and cellular phones in our daily lives. Thereafter, the underlying paradigm of device integration was adapted to light-waves, leading to the development of photonic integrated circuits (PICs) that offer diverse functional building blocks, including laser sources, optical filters, and modulators, which are interconnected through nano-scale optical waveguides.[32]

Speaking of light-waves, it merits mention that infrared-range fiber-optics currently comprise the majority of the backhaul network of the contemporary globalized internet, and so the infrared range is just as critical as integrated electronics to the interconnectedness of our modern globalized digital world. Furthermore, the infrared range is certainly higher-frequency and broader-bandwidth than the congested microwave spectrum, and fiber-based communications technology is already widely available. Taken together, these facts beg the question: why not bypass the terahertz range altogether, and adapt fiber optics to wireless infrared communications in order to support ongoing growth in mobile data traffic? To answer that, we must consider the physical properties of infrared waves. First, the shorter wavelength of infrared waves is highly susceptible to scintillation and other atmospheric effects, such as fog and dust, as well as greater sensitivity to misalignment.[12,33] Furthermore, infrared links will suffer interference from incoherent light sources, such as artificial lighting in indoor environments and sunlight outdoors.[34,35] Finally, and perhaps most importantly, there are safety concerns associated with infrared radiation. Specifically, the manner of coherent, collimated, directional beam that is required to support high data rates is supplied by a laser beam,[36,37] and exposure thereto can cause very serious eye damage and even permanent blindness.[38] This risk is exacerbated by the fact that the human eye will focus infrared radiation onto the retina, combined with the lack of an autonomous aversion response, such as blinking, against this invisible light. For these reasons, it is ill-advised to rely solely upon infrared waves to address the growing demand for increased wireless traffic, and so the terahertz range must be fully exploited if we are to continue the growth of wireless data capacity in mobile networks.

Although our discussion has thus-far been centered around future wireless communications technology, this is not the sole viable use of terahertz waves. Indeed, early interest in terahertz technology was spurred by the prospect of astronomical investigations,[39] with the promise of rich information about the interstellar medium and gas clouds,[40,41] and the capacity to monitor star formation[42] by exploiting key molecular resonances in this range. Terahertz waves have also historically served as a valuable tool to study the cosmic background radiation and the early universe,[43,44] much of which has red-shifted from higher frequencies. Aside from astronomy, the terahertz range also finds several valuable and specialized sensing, imaging, and inspection applications owing to the unique properties of terahertz waves.[45,46] Terahertz radiation is non-ionizing because an individual photon carries little energy. This is in contrast to x rays, for which a single photon carries sufficient energy to ionize atoms, and hence long-duration or intense exposure is injurious to health. On the other hand, terahertz radiation is somewhat akin to x rays because they can penetrate a variety of optically opaque materials, especially non-polar substances,[47,48] and even to a modest degree in biological tissues.[49] A terahertz-range wavelength is also less than a millimeter, which translates to high spatial resolution when deployed in imaging, and radar applications,[50–52] and is an advantage over

27 October 2023 05:17:16

© Author(s) 2023

millimeter-wave and microwave alternatives. Terahertz waves have therefore shown promise as a noninvasive diagnostic tool for diseases, including skin cancers[45,53,54] and dental caries.[55,56] Terahertz imaging may also be applied to the electronics industry, offering detailed inspection of wafer quality and doping profile,[57,58] as well as a tool to visualize semiconductor dynamics on the femtosecond scale.[59] The object-penetrating properties of terahertz waves are also valuable for the automotive industry, offering contactless inspection of multi-layer paint coatings that are subject to stringent quality-assurance requirements.[60,61] Terahertz-range object penetrating imaging can serve to identify internal voids and defects in plastics that are entirely hidden to the naked eye[62,63] and can also monitor the glass-transition of these materials in real-time.[64] The terahertz range is also of interest to the pharmaceutical industry to monitor tablet coating quality[65] and chemical composition.[66] This latter point is of key interest, as the chemical composition of consumer drugs is of critical importance to quality assurance, and can be identified by exploiting certain terahertz-range molecular resonances.[67] Finally, the terahertz range has shown promise for security applications[68] to identify hidden weapons,[69] illicit substances,[70] and explosives.[71]

The lack of a suitable standard terahertz integration platform has meant that the systems that facilitated the most impressive and valuable demonstrations of terahertz-range sensing, imaging, and spectroscopy have historically been oriented toward free-space propagation. In other words, a directed, unguided terahertz beam must serve as the physical link between all components of the system—sources, detectors, beam splitters, modulators or choppers, frequency-dividers, and so on—as well as any analyte or sample of interest. It is a downright cumbersome architecture in which bulky optics must be mounted upon posts, physically separated with respect to their focal lengths, and manually aligned by an experienced operator. The resultant system is only really suited to a laboratory setting and hence can never be adapted to commercial-scale manufacture and distribution. Thus, although these systems have repeatedly shown their worth in a research context, their size, cost, challenging assembly, and the need for intermittent adjustment render them unsuited to real-world applications and operation by

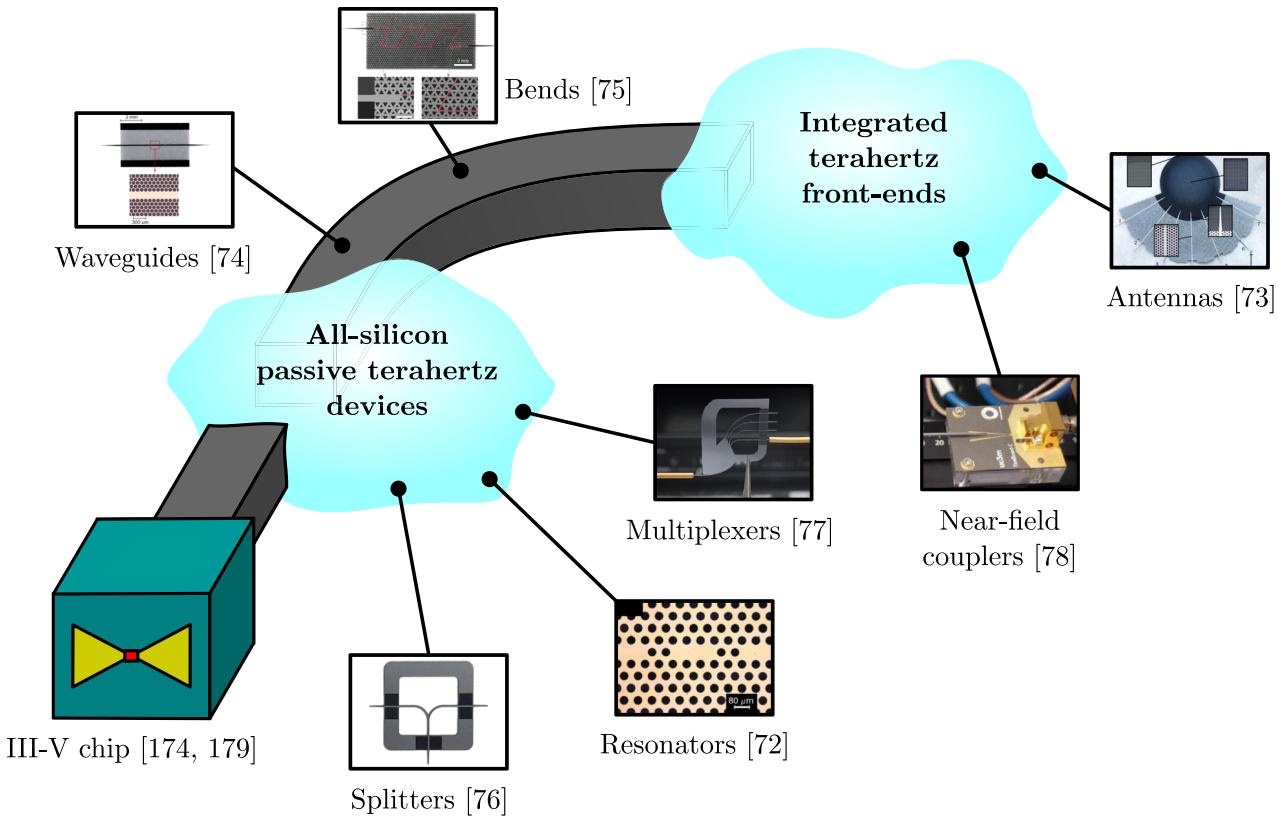

FIG. 1. A vision of a substrateless all-silicon terahertz integration platform based on low-loss all-silicon waveguides to connect various monolithically integrated passive functional building blocks and interfaces, as well as hybrid-integrated active devices. Inset images are reproduced with permission from C. M. Yee and M. S. Sherwin, Appl. Phys. Lett. **94**, 154104 (2009). Copyright 2009 AIP Publishing LLC; Headland *et al.*, APL Photonics **3**, 126105 (2018). Copyright 2018 AIP Publishing LLC; Gao *et al.*, Opt. Express **27**, 38721–38734 (2019). Copyright 2019 The Optical Society; Yang *et al.*, Nat. Photonics **14**, 446–451 (2020). Copyright 2020 Springer; Headland *et al.*, J. Lightwave Technol. **38**, 6853–6862 (2020). Copyright 2020 IEEE; Headland *et al.*, Optica **8**, 621–629 (2021). Copyright 2020 The Optical Society; and Rivera-Lavado *et al.*, IEEE Trans. Terahertz Sci. Technol. **13**, 34–43 (2023). Copyright 2023 IEEE.

27 October 2023 05:17:16

© Author(s) 2023

lay-people. This has been a key impediment to the widespread adoption of terahertz technology, leading to a pronounced asymmetry between the rich litany of promising laboratory demonstrations and the sluggish uptake of real-world uses of terahertz waves. In order to address this problem and achieve the full potential of terahertz technology, it will be necessary to *eschew free-space beams* entirely, and instead transfer terahertz waves with *fixed interconnect*. Put simply, what the terahertz range needs right now is a good integrated waveguide.

Ideally, a terahertz waveguide should be very efficient given intrinsic SNR issues that are faced by terahertz technology, including low available power and high free-space path loss of terahertz waves.[30] This problem would be severely compounded if a poor choice of device platform led to fundamentally lossy interconnect and inefficient components. The ease and compactness of routing, as well as the capacity to incorporate a variety of functional devices, will be significant factors. Compactness is critical given the long wavelength of terahertz waves relative to the optical range. Broadband operation is another essential requirement, as a major part of the appeal of terahertz waves is the large available spectral bandwidth, and so it is important that the device platform itself does not become a bottleneck in this regard. Finally, affordable fabrication cost is also a requirement for widespread adoption. The realization of all of these criteria would open the door to commercially viable terahertz systems, and thereby enable real-world deployment of terahertz-wave technology.

In this tutorial, we will present general considerations regarding appropriate micro-scale waveguides to serve as the basis for an integration platform for the terahertz range. The overarching message is that, due to several factors including markedly lower propagation loss, compactness, monolithic device structure, affordable and scalable manufacture with high yield, structural rigidity, and versatility, dielectric waveguides are the most promising avenue toward suitable terahertz-range interconnect, and this is a conclusion that echoes the contentions of terahertz-range researchers at the turn of the millennium[79,80] and of the millimeter-wave engineers that came before them in the 1970s.[81] We believe that the time has come to put these many-decades-old insights into practice to refine the broad concept of "efficient terahertz-range dielectric waveguides" into a viable general-purpose terahertz-range platform and to use this platform to implement terahertz-range integrated circuits and systems. Toward this end, we will carefully expound and justify our preference for substrateless all-intrinsic-silicon dielectric waveguides, in particular, and we will also present and contrast several different approaches to design and realize them. We will also explore the passive functional devices that may be integrated directly with these waveguides in order to construct useful circuits and systems, as illustrated in Fig. 1. Finally, we offer our perspective on the future of all-silicon substrateless integration platforms for terahertz waves, including the need for hybrid integration techniques to incorporate active terahertz devices, such as sources and detectors of terahertz radiation.

Throughout this article, we employ a phase convention that treats phase delay as negative and phase advance as positive, and is favored in engineering. In physics, the converse convention is generally preferred. Either is valid, but mistakes can arise when we erroneously combine formulas that are drawn from both academic traditions. It is therefore most important to be consistent, and wherever possible, to consider whether the physical interpretations of our results make sense.

II. THE EARLY DAYS

In terms of data transmission speed, the optical fiber represents the apex of human achievement, with staggering demonstrations, such as links in excess of 1 Pbit/s.[82,83] The current ubiquity and importance of optical fibers is therefore hardly surprising. Indeed, the entire earth is currently surrounded by a network of undersea transcontinental links,[84,85] which is necessary infrastructure to support the modern globalized internet. It is not an exaggeration to say that we are currently living in the "optical fiber era" and have been since roughly the 1980s, as the first non-experimental deployment of an optical fiber took place in the mid-1970s, and the first transatlantic cable was laid in 1988.[86] Prior to this, the millimeter-wave range was the only viable avenue to explore high-bandwidth communications technology, e.g., for trunk lines to aggregate several telephone circuits.[87] The millimeter-wave range was also envisaged for short-range communications, high-precision radar, and sensing applications.[88] In order to support these applications, researchers of this pre-fiber era were seeking a suitable integration platform for millimeter-waves, and they noted the many benefits of dielectric waveguides,[81] including lower loss than planar metallic transmission lines and smaller size than hollow metallic waveguides—closely related arguments to those that will be presented in Sec. III C.

The years prior to the fiber era saw significant research effort dedicated to "dielectric image lines,"[81,90,93–95] composed of a dielectric core situated upon a conducting ground plane, as depicted in Fig. 2(a), as well as "nonradiating dielectric waveguides"[89] that were sandwiched between conductive planes, as shown in Fig. 2(b). The metal planes served to suppress of the surface-tangential polarization for truly single-mode operation,[81] but this predictably came at the expense of dramatically increased loss in the terahertz range.[96]

A number of noteworthy demonstrations of useful functional devices were reported in the epoch in question. Some such achievements include microwave-range bends for routing[97] and V-band tapered rod antennas for off-board access,[98] as well as frequency-selective passive devices, such as tunable microwave bandpass filters at ~20 GHz[99] and the ~55-GHz shunt-coupled resonators,[90] shown in Fig. 2(c). Incidentally, these devices are closely related to those which will be reviewed in Sec. VIII A. Another noteworthy passive device demonstration is a 3-dB hybrid coupler, which was used to feed a balanced IF downconversion mixer operating at ~60 GHz.[100] This mixer is an example of an active device that is incorporated directly into the dielectric waveguide-based integrated circuit, which was a topic that was of great interest during that time. A popular active device for this purpose was the Gunn diode, which is capable of exhibiting spontaneous microwave and millimeter-wave oscillation in response to applied DC bias,[101] and has been incorporated into dielectric cavity resonators for stable tunable local oscillators.[102,103] The innate nonlinearity of Gunn diodes can also offer mixing action while simultaneously oscillating, thereby realizing a "self-oscillating mixer" capable of direct downconversion in a

27 October 2023 05:17:16

© Author(s) 2023

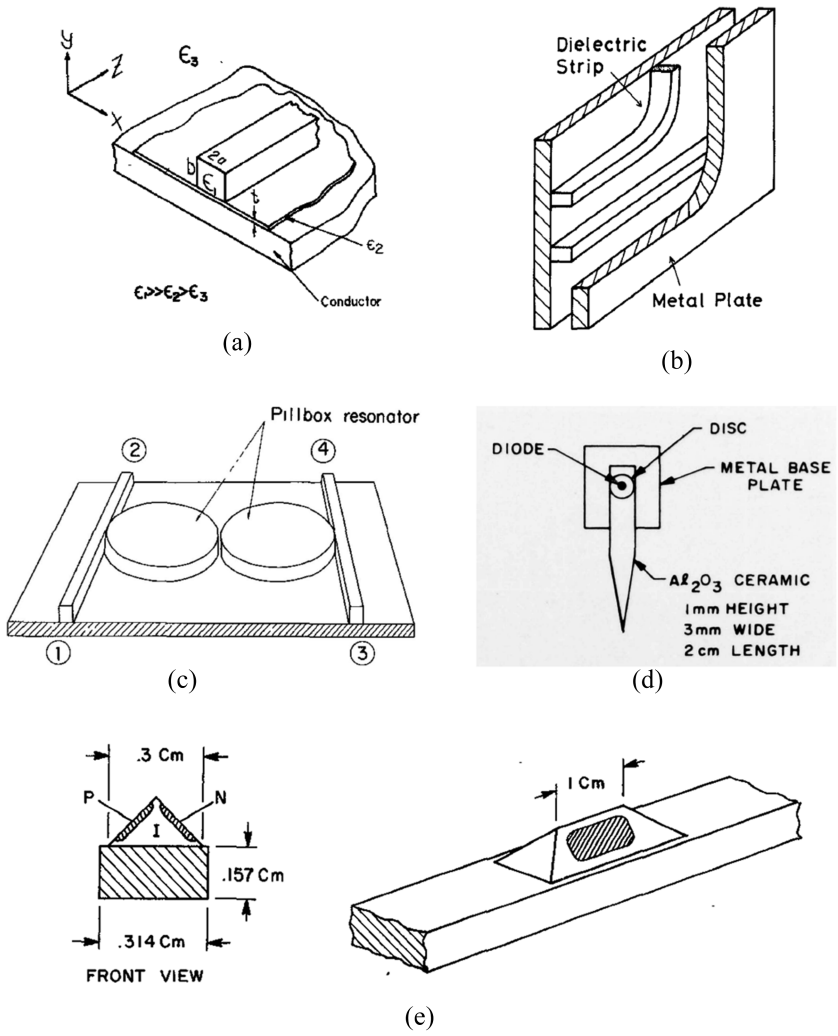

FIG. 2. A selection of noteworthy early millimeter-wave dielectric waveguide works (i.e., up until 1981), showing (a) a depiction of a dielectric image line, reproduced with permission from R. M. Knox, IEEE Trans. Microwave Theory Tech. **24**, 806–814 (1976). Copyright 1976 IEEE; (b) a non-radiating dielectric waveguide, reproduced with permission from T. Yoneyama and S. Nishida, IEEE Trans. Microwave Theory Tech. **29**, 1188–1192 (1981). Copyright 1981 IEEE; (c) a bandpass filter based upon two coupled disk resonators, reproduced with permission from S. Shindo and T. Itanami, IEEE Trans. Microwave Theory Tech. **26**, 747–751 (1978). Copyright 1978 IEEE; (d) the physical structure and measured conversion gain of a Gunn diode-based self-oscillating mixer, operating at 60 GHz, from Ref. 91; and (e) a PIN junction-based phase shifter integrated with a dielectric waveguide, operating at 70 GHz, reproduced with permission from H. Jacobs and M. M. Chrepta, IEEE Trans. Microwave Theory Tech. **22**, 411–417 (1974). Copyright 1974 IEEE.

single compact two-terminal component.[104] This compact hybrid-integrated receiver was incorporated into a 60 GHz image-line,[91] as shown in Fig. 2(d). More classical, circuit-oriented approaches to construct transceiver systems were also pursued,[105] i.e., by interconnecting all required functional blocks of the system, including a dielectric rod antenna and a dielectric ring-based filter, together with millimeter-wave dielectric image lines. Finally, phase shifters using PIN diodes to modulate the cross section area of the dielectric guide were demonstrated at frequencies as high as 70 GHz,[92] as shown in Fig. 2(e). This latter demonstration may be of interest to terahertz-range researchers, as integrated phase shifters are highly sought-after in the terahertz range due to their role in dynamic beamforming front-ends, which are a firm requirement of the majority of wireless applications of terahertz waves.[106] Perhaps we terahertz engineers of the present day can draw inspiration from such five-decades-old millimeter-wave technology.

Interest in millimeter-wave-range dielectric waveguides and circuits predictably diminished from the 1980s onwards because optical fiber has consistently provided a preferable avenue to increase network capacity, i.e., by using as much optical fiber, and as little microwave-range transmission line, as possible. As stated in Ref. 107, "Obviously, the deeper fiber can penetrate toward the

27 October 2023 05:17:16

© Author(s) 2023

subscribers, the more bandwidth can be provided." Thus, the past four decades have seen network operators bringing the optical fibers progressively closer to the consumer; from the trunk and backhaul to the node, then to the curb, to the premises, and finally, into the home or office itself.[107,108] During this time, the nanoscale structures for the manipulation of light-waves have dominated all dielectric waveguide-oriented research, reflecting the priorities of network operators, and this has spurred drastic improvements in optical fibers[109] and in integrated nanophotonics.[32,110] However, there is a final frontier that will not ever be traversed with a fiber, and that is the air interface of wireless devices. As stated in the Introduction, the infrared waves that are carried by fibers are wholly inadequate for this purpose, and this motivates exploration of millimeter-wave and terahertz wireless technology. Thus, we now find ourselves back at the starting point of this brief historical account: searching for a suitable integration platform for high-frequency devices.

III. APPROPRIATE INTERCONNECT FOR THE TERAHERTZ RANGE

An integration platform is characterized first and foremost by the interconnect that connects its constituent functional building blocks together. This section will explore fundamental aspects concerning the appropriate choice of interconnect for the terahertz range.

A. Material properties

The constituent materials that comprise a given waveguide are of critical importance, not just to performance but also to the very nature of the physical confinement mechanism. Thus, we compute the electromagnetic properties of materials of interest using the Drude model,[111] which describes electrical resistance of materials in terms of the random scattering of free charge carriers, i.e., electrons and holes. It is noted that this model applies exclusively to uniform bulk materials, and so it cannot directly account for structural concerns such as physical defects, surface roughness, or disorder in crystalline morphology. The Drude model serves to evaluate complex, frequency-dependent conductivity[112]

$$\tilde{\sigma}(\omega) = \frac{\sigma_{DC}}{1 - j\omega\tau}; \quad \tau = \frac{\sigma_{DC}}{\omega_p^2 \varepsilon_0}; \quad \omega_p = \sqrt{\frac{Nq}{\varepsilon_0 m_{eff}}}. \tag{1}$$

The scattering relaxation time, τ, which is the mean time interval between collisions for a given carrier. Given that frequent collisions are an impediment to the flow of electrical current, τ is related to DC conductivity[113] through the plasma frequency, ω_p. This can be understood as the frequency at which electrons displaced from equilibrium will oscillate due to the attractive force of the surrounding lattice of ions.[114] The free-carrier concentration, unit charge of an electron, and equivalent mass of a carrier are N, q, and m_{eff}, respectively.

Given that there is an essentially limitless number of metals to choose from, we will analyze gold as an exemplar, with DC conductivity of $\sigma_{DC} = 4.1 \times 10^7$ S/m and scattering relaxation time of $\tau = 0.15$ ps.[115,116] The calculated terahertz-range material properties of gold are plotted across the entire terahertz range in Fig. 3(a).

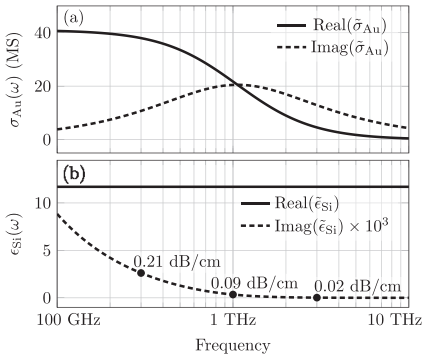

FIG. 3. Drude model of terahertz-range material properties of (a) gold and (b) 2 kΩ cm intrinsic silicon, where the imaginary component is enhanced for visibility, and the bulk material attenuation is indicated at specific frequencies of interest.

It can be seen that the real component of conductivity decreases with respect to frequency, reaching half-maximum in the vicinity of 1 THz, at which the imaginary component reaches its peak. In other words, gold transitions from being a good conductor at the lower end of the terahertz range into a poor conductor at the higher end.

Aside from the complex conductivity in Eq. (1), the Drude model can also determine the frequency-dependent complex relative permittivity[112,113]

$$\tilde{\varepsilon}(\omega) = \varepsilon_\infty - \frac{\omega_p^2}{\omega^2 + j\frac{\omega}{\tau}}, \tag{2}$$

where ε_∞ is the real-valued relative permittivity in the limit of high-frequency. It is noted that Eqs. (1) and (2) are equivalent, as both are complete descriptions of a given material's electromagnetic properties. The reason that we have presented these dual descriptions is that it is generally more intuitive to speak of conductors in terms of conductance and dielectrics in terms of their dielectric constant.

It is of interest to analyze a dielectric using the Drude model, and as before, we select an exemplar material: intrinsic silicon, as it is a high-index, low-loss, non-dispersive material in the terahertz range.[117] Intrinsic silicon wafers of different grades of purity are available, with lower-grade silicon tending to be more lossy because of the presence of impurities acts analogously to doping the silicon with free carriers. A given intrinsic silicon wafer is typically identified by its DC resistivity, $\rho_{DC} = 1/\sigma_{DC}$, which depends upon the concentration, N, of free carriers,[112] as well as the carrier mobility, μ, which has been determined empirically for silicon[118]

$$\sigma_{DC} = qN\mu; \quad \mu_{Si}(N) = \mu_{min} + \frac{\mu_{max} - \mu_{min}}{1 + \left(\frac{N}{N_{ref}}\right)^{\chi}}, \tag{3}$$

where $\mu_{min} = 92$ cm^2/V s, $\mu_{max} = 1360$ cm^2/V s, $N_{ref} = 1.3 \times 10^{17}$ cm^{-3}, and $\chi = 0.91$ is a dimensionless fitting parameter. The constraints given in Eq. (3) are combined and then solved numerically for N, and the result is then used to compute the plasma frequency and scattering relaxation time via Eq. (1). Finally, Eq. (2) serves to determine complex permittivity using $\varepsilon_\infty = 11.7$.

27 October 2023 05:17:16

© Author(s) 2023

We select a conservative nominal resistivity of 2 kΩ cm from which we derive plasma frequency ω_p = 170 Grad/s and relaxation time τ = 0.20 ps.[119] The relative permittivity of intrinsic silicon is shown in Fig. 3(b), and it can be seen that the real component is near-constant over our frequency range of interest, which is indicative of low material dispersion. The imaginary component, which is associated with loss, is close to zero. It can also be seen that material loss monotonically decreases with respect to frequency; the maximum loss-tangent value of $\tan\delta = \mathrm{Imag}(\tilde{\varepsilon}_{Si})/\mathrm{Real}(\tilde{\varepsilon}_{Si}) = 7.6 \times 10^{-4}$ is encountered at the lower-frequency limit of the terahertz range, and at 1 THz, it has reduced to less than half of this value. Thus, the material loss of silicon follows an inverse trend with respect to gold; the former is most lossy at low frequencies whereas the latter is lossiest at high frequencies. Furthermore, while gold transitions from a good conductor to a poor conductor, the properties of silicon are essentially stable and consistent across the entire terahertz range.

B. Propagation loss in-guide

Efficiency is of critical importance to terahertz systems, owing to innate SNR issues associated with terahertz waves,[30] and so the intrinsic loss of interconnect is of utmost importance. Thus, propagation loss in waveguides is the subject of this section. We will begin by analyzing hollow metallic waveguides, as they are currently the dominant form of wired interconnect in the terahertz range, as well as the basis of all terahertz instrumentation systems that offer port-access,[120–122] where the standardization of mating flanges[123] allow for highly convenient and repeatable alignment and modular devices.

1. Metallic waveguides

Reflection at an air–conductor interface is the confinement mechanism of hollow metallic waveguides. A finite air-volume is wholly enclosed by electrical conductors in two dimensions, thereby restricting field propagation to the remaining dimension. Confined fields repeatedly scatter from the guide's walls, and in each case, induced conduction currents mediate the generation of the reflected wave, causing progressive Ohmic loss along the length of the guide. This loss is quantified with the amplitude attenuation coefficient, $\alpha_{\mathrm{ohmic}}^{\mathrm{amplitude}}$,

$$|\tilde{A}(l)| = |\tilde{A}(0)| \cdot \exp\left(-l \cdot \alpha_{\mathrm{ohmic}}^{\mathrm{amplitude}}\right), \tag{4}$$

where l is propagation length, and $|A(l)|$ is signal amplitude. For the fundamental TE_{10} mode of a rectangular metallic waveguide,[124]

$$\alpha_{\mathrm{ohmic}}^{\mathrm{amplitude}} = \frac{R_{\mathrm{surface}}}{a^3 b \beta k_0 \eta}\left(2b\pi^2 + a^3 k_0^2\right), \tag{5}$$

where a is the long-edge width of the guide, $b < a$ is the short-edge height, $k_0 = 2\pi/\lambda_0$ is the free-space wavenumber, β is the in-guide phase constant, $\eta = \sqrt{\mu_0/\varepsilon_0}$ is the impedance of free-space, and R_{surface} is the surface resistance of the lossy metal. In order to extract surface impedance from the complex Drude conductivity that we calculated in Sec. III A, we employ the following expression:[116]

$$Z_{\mathrm{surface}} = R_{\mathrm{surface}} + jX_{\mathrm{surface}} = \sqrt{\frac{j\omega\mu_0}{\tilde{\sigma}(\omega) + j\omega\varepsilon_0}}. \tag{6}$$

Equations (1), (5), and (6) are sufficient to compute the theoretical propagation loss of a hollow metallic waveguide in the terahertz range. All that remains is to select the physical dimensions of the guide, and a typical hollow waveguide will have a 1:2 cross-sectional aspect ratio (i.e., $b = a/2$) in order that the first undesired TE and TM modes will exhibit the same cutoff frequency, as this maximizes single-mode bandwidth. The IEEE recommends[125,126] to operate hollow metallic waveguides in a subset of the single-mode region that spans from ~20% above the fundamental cutoff frequency up until ~5% below the first higher-order mode, in order to avoid strong dispersion and loss. This yields 40% relative bandwidth, which is the total frequency span divided by the center frequency. At this center frequency, $a = 0.8\lambda_0$, and in our analysis, we select this electrical (i.e., wavelength-relative) size, and so an entirely different waveguide is modeled for each and every frequency considered. This is because we are interested in the performance of a *class* of waveguide, as opposed to a single guide of fixed physical size. This also allows for evaluation of propagation loss across the entire terahertz range, as opposed to being restricted to the operation bandwidth of a given waveguide. The result is shown in Fig. 4. It can be seen that the reduction in conductance with respect to frequency, which is shown in Fig. 3(a), causes a corresponding increase in propagation loss in hollow metallic waveguides from ~0.04 dB/cm at the lower-frequency end to >1 dB/cm at 1 THz.

The measured propagation loss of several terahertz-range hollow metallic waveguides is taken from the literature[127–133] and plotted alongside the theoretical calculation in Fig. 4. It can be seen that they follow roughly the same trend with respect to frequency and that measured loss is consistently higher than our theoretical model. Note that the two cases in which the divergence from theory is highest employed 3D printing to fabricate the waveguides,[128,132] which has a tendency to leave an irregular surface finish. For this reason, we conclude that the deviation from theoretical prediction likely due to surface roughness,[134,135] which we did not consider in our analysis because it varies from case to case.

Aside from hollow metallic waveguides, planar metallic transmission lines are also of interest due to their prevalence in active terahertz chips, as they are needed to make electrical contact with terahertz active devices, such as two-terminal diodes.[136–139] It is often not possible to incorporate a groundplane into the transmission line structure at micro-scale, and so all conductors must be in the same plane, as in a coplanar waveguide. A few published reports of propagation loss[140–142] are included in Fig. 4, and it can be seen that the coplanar waveguide is markedly less efficient than hollow metallic waveguides. This is due to the strong concentration of interaction between terahertz waves and lossy metal inside the slots that define a coplanar waveguide's track, and it is a result that generalizes across planar metallic transmission lines. Thus, planar metallic transmission lines should be treated as a terse necessity when dealing with active terahertz devices, but since they cannot practically guide

27 October 2023 05:17:16

© Author(s) 2023

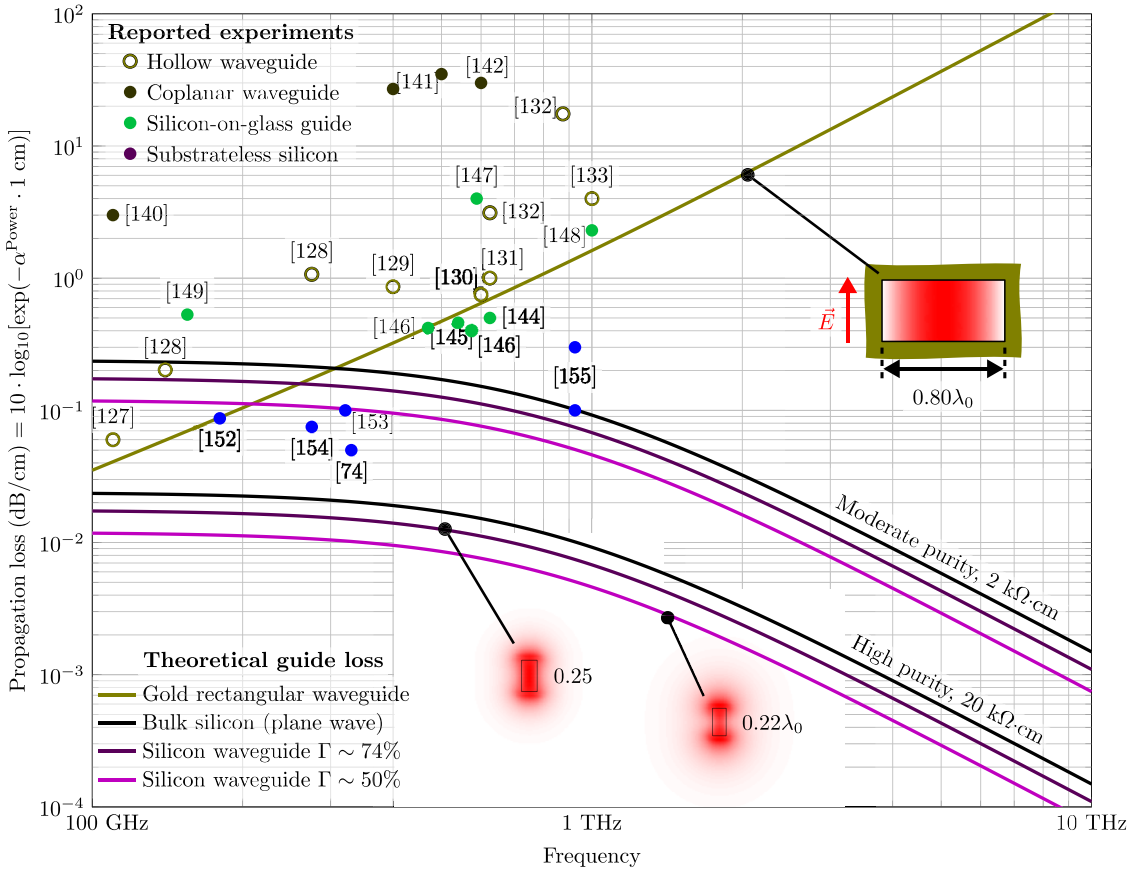

FIG. 4. Theoretical propagation loss of gold hollow rectangular waveguides and substrateless, unclad intrinsic silicon waveguides, across the entire terahertz range. Material properties are derived from the Drude model. Guide dimensions are specified relative to a wavelength in order to isolate the impact of changing Drude loss, and so every single point on each curve should be considered a separate waveguide structure. Reported propagation loss from the literature is also included for verification and to provide insight into realistic performance. The frame-tethered guides discussed in Sec. V, and the valley photonic crystals in Sec. VI C are not included in this plot, as they exhibit increased loss due to structural reasons that are not related to the material-absorption losses that are most relevant to the present section. Inset diagrams are of the same scale, and show modal field distributions in linear scale.

waves over any reasonable distance, it is good practice to utilize as little as possible.

2. Dielectric waveguides

Propagation loss in a dielectric waveguide is closely related to the intrinsic absorption of the dielectric material that comprises the waveguide core. This can be computed from the complex permittivity

$$\alpha_{\text{bulk}}^{\text{amplitude}} = k_0 \cdot \text{Imag}(\tilde{n}) = k_0 \cdot \text{Imag}\left(\sqrt{\tilde{\varepsilon}}\right), \tag{7}$$

as the propagation of a monochromatic plane wave in a lossy dielectric of complex refractive index $\tilde{n}$ is of the form $\tilde{A}(l)/\tilde{A}(0) = \exp(-jk_0\tilde{n}^* l)$, with magnitude component $\exp(-k_0 l \cdot \text{Imag}(\tilde{n}))$. It is noted that the complex index must be conjugated in order to account for the discrepancy between the engineering phase convention and the physics-oriented Drude model. It is also common to describe loss in terms of a power absorption coefficient, $\alpha_{\text{bulk}}^{\text{power}} = 2\alpha_{\text{bulk}}^{\text{amplitude}}$, which relates exponential reduction of power to propagation length.

Unlike hollow metallic waveguides, dielectric waveguides are *unshielded*, meaning the modal field distribution is nonzero in the region outside the waveguide core, and decays exponentially with respect to distance. Thus, the overall loss of guided waves can be found by averaging the bulk absorption coefficient at each point in the transverse plane, weighted by power flux density at that point,

$$\alpha_{\text{guide}}^{\text{power}} = \frac{\iint_S |\vec{P}_{\text{mode}}(\vec{p})| \cdot \alpha_{\text{bulk}}^{\text{power}}(\vec{p})\,\text{d}S}{\iint_S |\vec{P}_{\text{mode}}(\vec{p})|\,\text{d}S}, \tag{8}$$

where S is the infinite-extent transverse plane of the guide, $\vec{P}$ is Poynting vector of guided mode field, and $\vec{p}$ is position in the plane of S. It is noted that this quantity will be frequency-dependent, even if the bulk material absorption is wholly non-dispersive, as the spatial arrangement of modal fields is dependent upon the shape and electrical size of the guide core. In the case considered here,

27 October 2023 05:17:16

© Author(s) 2023

bulk absorption is binary; either $\alpha_{\text{bulk}}^{\text{power}}(\vec{p}) = \alpha_{\text{bulk Si}}^{\text{power}}$ in the guide, or $\alpha_{\text{bulk}}^{\text{power}}(\vec{p}) = 0$ outside. Thus, we may factor out the absorption coefficient and define the "confinement factor," Γ, as the proportion of guided fields that exists within the material of the guide core,

$$\alpha_{\text{guide}}^{\text{power}} = \alpha_{\text{bulk}}^{\text{power}} \cdot \frac{\iint_G |\vec{P}_{\text{mode}}(\vec{p})| \mathrm{d}G}{\iint_S |\vec{P}_{\text{mode}}(\vec{p})| \mathrm{d}S} = \alpha_{\text{bulk Si}}^{\text{power}} \cdot \Gamma(f), \tag{9}$$

where G is a finite-sized surface defined as the intersection between the guide core and the infinite transverse plane S. This assumes the surrounding material is lossless, as in a vacuum, but if the guide were to consist of more than one lossy material, we must take the sum of product of each material's power coefficient with confinement factor.[143] An example of such a guide is the silicon-on-glass platform,[144–149] which is based more-directly upon established nanophotonic conventions.[150,151] This approach bonds a microscale silicon waveguide onto a lower-permittivity glass substrate, yielding improved robustness and convenient handling and positioning, which are highly beneficial. However, the substrate generally exhibits greater bulk absorptivity than high-resistivity intrinsic silicon, and as a result, the reported propagation loss shown in Fig. 4 is essentially equivalent to that of hollow metallic waveguides. The silicon-on-glass platform therefore has no substantive advantage over the efficiency of the current dominant form of terahertz-range interconnect.

Returning to the substrateless all-silicon guide, we consider the simple case of a guide that is clad on all sides with air. Incidentally, this structure is called a "dielectric rod waveguide" and is covered in detail in Sec. IV. For the core dimensions, we select a rectangular cross section with a 1:2 aspect ratio in order to maintain consistency with the previous example of a hollow metallic waveguide. Modal field distributions are computed using the commercial software package CST Studio Suite, and confinement factors are extracted therefrom. It is noted that there is no special significance to the particular values of field confinement that are chosen, other than being in the single-mode region of the waveguide. The result is plotted in Fig. 4, together with the propagation loss in bulk intrinsic silicon, which serves as an upper-bound. We include two different grades of silicon in order to explore the impact of purity upon waveguide performance. It can be seen that, in contrast to the hollow metallic waveguide, the propagation loss of a silicon waveguide actually decreases with respect to frequency, which is of great benefit to high-frequency operation and to scalability across the terahertz range.

Interest in terahertz-range all-silicon dielectric waveguides is more recent than in hollow metallic waveguides, making them less prevalent in the literature. Nevertheless there have been several reports,[74,152–155] which are displayed in Fig. 4 for comparison with the theory. In all of these cases, the resistivity of the monocrystalline silicon wafer deployed was nominally between 10 and 20 kΩ cm, according to the manufacturer. It can be seen that, although they are close, the reported loss is higher than the theoretical prediction that is obtained with high-purity silicon, and in the case at ~0.9 THz,[155] it is higher than even moderate-purity silicon. Reasons for this may include scattering due to an imperfect surface finish, analogous to the impact of surface roughness that is described in Sec. III B 1. Another factor may be absorption of terahertz waves in the nonzero-humidity air that surrounds the guide, which is not accounted for in our analysis. Nevertheless, it remains clear that all-silicon terahertz guides strongly outperform the alternatives. Finally, it merits mention that it is practically challenging to accurately characterize the propagation loss of low-loss integrated guides because propagation loss is extracted by comparison of the transmission loss of different-length straight waveguides, which are limited to a few centimeters. As a consequence, the difference in transmitted power between guides can be less than 0.1 dB, which is comparable to alignment and calibration error. This issue is particularly significant at higher frequencies due to the proportional reduction of all physical dimensions, and hence the results at ~0.9 THz[155] must be treated with caution.

C. The benefits of substrateless all-silicon guides

1. Efficiency

Both the theoretical analysis and the reports from the literature lead us to the same conclusion: all-silicon dielectric waveguides exhibit significantly lower loss than hollow metallic waveguides, and furthermore, this advantage becomes more pronounced at higher frequencies. It is only at the lower-frequency limit of the terahertz range (i.e., below 200 GHz) that performance is comparable. This is the primary reason why we prefer dielectric waveguides over hollow metallic waveguides for terahertz-range operation and is also a key motivation to write this tutorial. It is also observed in Fig. 4 that this advantage is essentially lost if a glass substrate is included. Thus, for the future advancement of terahertz technology, we strongly advocate for *substrateless* all-silicon dielectric waveguides.

2. Compactness

The inset diagrams to Fig. 4 show that the cross-sectional area of an all-silicon dielectric guide's core is significantly smaller than the hollow metallic waveguide's inner volume, at just ~10% of its area. This is because, while a hollow metallic waveguide requires a minimum transverse width of a half-wave above cutoff, a dielectric waveguide of high-index core is miniaturized by the fact that the in-medium wavelength is smaller than in free-space. Additional to that, the physical robustness of a hollow metallic waveguide depends upon metal walls are significantly thicker than the microscale inner volume, especially for higher-frequency guides, and this increases the minimum guide-to-guide separation. Thus, silicon dielectric waveguides exhibit a clear compactness advantage over hollow metallic waveguides.

3. Rigidity and structural robustness

Silicon guides are not the only candidate core material available. Indeed, there have been several reports in the literature of flexible polymer fibers with comparable efficiency.[156–159] However, although fibers of this sort are well suited for long-distance cabling,[160] they do not hold their shape due to their flexibility, making them less suitable for a fixed device platform than the rigid crystalline structure of intrinsic silicon, which is resistant to all forms of deformation. In additiona, silicon has a low coefficient of thermal expansion, which augments its physical stability,[161] as well as high thermal conductivity due to its diamond-like molecular structure,[162] for heat management.

27 October 2023 05:17:16

© Author(s) 2023

4. Cost-effective, scalable fabrication

Silicon is a low-cost and abundant material due to its critical importance in integrated electronics, which has led to a highly streamlined global supply chain. As a result, it its generally not difficult to find suitable high-resistivity single-crystal intrinsic silicon wafers at low cost, making terahertz-range technology an incidental beneficiary of the electronics industry. The fabrication technique that is most commonly deployed in order to shape this low-loss material into micro-scale terahertz waveguides is "deep reactive ion etching," also known as the "Bosch process," as it was pioneered in the 1990s by the corporation of the same name.[163–165] This is a mask-based plasma etching technique that is prized for its ability to define vertical, high-aspect-ratio side-walls with sub-micrometer precision, and was initially developed for compact micro-accelerometers and gyroscopes for use in automotive safety applications.[163,164] Thereafter, deep reactive ion etching has been deployed for a broad variety of micro-structures ranging from gears and watch parts[166,167] to arrays of microscopic needles for transdermal drug delivery,[168] and of course, to terahertz technology. It is noted that as dielectric waveguides are not the sole terahertz-range use for deep reactive ion etching, as it has also facilitated large-scale arrays of terahertz dielectric resonators,[119,169–171] which require a deep etch in order to define micro-scale silicon volumes. In addition, terahertz-range hollow metallic waveguides can be fabricated using deep reactive ion etching, by defining trenches in a series of silicon "platelets," coating their surfaces with metal, and finally stacking the metalized platelets together in order to enclose the hollow internal volume of the guide.[172] The high precision offered by deep reactive ion etching leads to very low surface roughness, which accounts for the fact that the lowest-loss metallic waveguides cited in Fig. 4 (i.e., relative to the theoretical trend-line) were fabricated in this way,[130,133] in contrast to the guides fabricated with more-standard six-axis numerical-control machining.[127,128] Thus, the highest-quality terahertz-range hollow metallic waveguides utilize the same process as substrateless all-silicon dielectric waveguides, albeit with one important distinction: while the former necessarily demands that several layers be etched prior metallization and stacking, the latter only a requires a single layer, and without any metallization or assembly. This represents an intrinsic cost reduction; all components of a given device may be fabricated at the same time, together with the guides that interconnect them, and in a single-mask etch process. Furthermore, this single mask may be re-used in order to fabricate several copies of a given device or system, leading to considerable cost-per-unit reduction provided there is sufficient demand for large-volume manufacture. This, combined with the intensive streamlining of the semiconductor foundries that serve the digital electronics industry, points to the possibility of mass-produced terahertz devices, which will be necessary for the widespread adoption of terahertz technology.

5. Versatility

As will be seen in Sec. VIII, many diverse functional passive devices for terahertz-domain signals processing can be implemented directly with substrateless micro-structured silicon and connected together with integrated dielectric-waveguides. Given that different applications of terahertz waves demand distinct fundamental components, the diversity of the devices reported in Sec. VIII informs the number of different classes of terahertz-range system that may be implemented. Furthermore, monolithic co-integration of different devices avoids the need for interposers to bridge heterogeneous *ad hoc* combinations of components, which increases overall system size and the complexity of assembly, and frequently poses a performance bottleneck. On the other hand, an all-intrinsic-silicon platform is somewhat limited in that only passive devices can be implemented in this way, and hence terahertz waves must be coupled from an external source. This introduces precisely the same issues mentioned above, i.e., increased overall system size and a performance bottleneck at the interface. To address this, there is a rapidly growing body of work in terahertz hybrid integration, in which an active III–V terahertz chip is fabricated separately to the all-passive, all-silicon integrated circuit, and then the two are assembled together.[137,138,173–179] The best approach for hybrid integration currently remains an open question, but it is firmly necessary in order for substrateless all-silicon micro-scale photonics to develop into practical hand-held devices for real-world applications.

IV. DIELECTRIC ROD WAVEGUIDES

Perhaps the most straightforward form of all-silicon waveguide is the dielectric rod waveguide (DRW), which is a micro-scale beam of silicon that is clad with air on all sides, as in the analysis presented in Sec. III B 2. The simplicity of this structure makes it an intuitive starting point to familiarize oneself with the general principles of dielectric waveguides.

A. A brief introduction to dielectric waveguide mode theory

Prior to delving into the terahertz dielectric rod waveguide literature, we will briefly analyze the physical mechanism of field confinement within a dielectric waveguide, as well as the relationship between confinement and dispersion, which is defined as the variation of wave speed with respect to frequency.

The general procedure for analysis of dielectric waveguides, which is adapted from Ref. 180, is as follows: First, a "phase constant," β, is defined as a variable. This quantity relates the change in phase experienced by a guided wave, $\Delta\phi$, to the physical distance traveled, l,

$$\Delta\phi(l) = -l \cdot \beta. \tag{10}$$

Given that this quantity concerns wave-speed, the phase constant can be related to an effective modal index, n_{modal} via the free-space wavenumber, k_0,

$$n_{\text{modal}} = \frac{\beta}{k_0}; \quad \Delta\phi(l) = -l \cdot k_0 \cdot n_{\text{modal}}, \tag{11}$$

and in multi-mode guides, each is associated with a different modal index and phase constant. Second, a mathematical expression for the cross-sectional modal field distribution that is dependent upon β is assumed. Boundary conditions are then applied to the index continuities of the slab guide, for both the electrical and magnetic field components, yielding two constraints for each physical boundary. These restrictions are combined mathematically in order to produce a single equation that is solely dependent upon β and is called the

27 October 2023 05:17:16

© Author(s) 2023

"dispersion relation." Finally, the dispersion relation is solved, producing a full description of the guided slab-mode's dispersion and field distribution.

We consider the modes of a substrateless dielectric slab waveguide, as shown in Fig. 5(a), which exhibits refractive-index discontinuities in only one transverse dimension, and for which analytical solutions are available. The analysis of this simple structure is useful and instructive, which is appropriate to maintain manageable scope in the context of a tutorial, but can be readily generalized to more sophisticated geometries. In contrast to Sec. IV, the material of the guide core is treated as a lossless dielectric material of frequency-independent refractive index $n_{\text{core}} = 3.42$, corresponding to intrinsic silicon. As it is substrateless, the core is enclosed on both sides with empty space, $n_{\text{clad}} = n_0 = 1.00$. These simplifications will essentially decouple the analysis from any specific choice of operation frequency and allow us to present results in more general, relative terms.

Phenomenologically, light rays are confined into the core region by total internal reflection, which occurs each time the ray is incident upon the interface between the core and the cladding. There is a specific, unique angle of incidence for which a given ray will have a 2π phase difference with the twice-reflected ray, and hence they will be in-phase, and this uniquely identifies the fundamental mode of the guide. In contrast, reflection angles that exhibit phase mismatch will progressively lose energy due to the destructive interference that occurs with each reflection, and the lost power is radiated into the cladding material. As a result, non-leaky propagating modes are identified by a well-defined right-angled triangle formed by the wavevector of the ray traveling in the bulk core material, the phase constant of the propagating mode, β, and a quantity that we define as the transverse propagation constant, which is associated with in-guide spatial change within the cross-sectional plane of the guide, and normal to the slab boundaries, i.e., the x-direction,

$$k_x = \sqrt{(k_0 n_{\text{core}})^2 - \beta^2}. \tag{12}$$

If we attempt to construct an equivalent triangle in the cladding region then the result will be an imaginary number, indicating a nonphysical solution; transverse wave propagation does not occur in the cladding material, and so there can be no such wavenumber. However, negating the argument of the square-root operation yields a decay constant that the decrease in evanescent fields with respect to distance from the waveguide core in the transverse dimension,

$$\alpha_x = \sqrt{\beta^2 - (k_0 n_{\text{clad}})^2}, \tag{13}$$

and can be considered a kind of dual to the transverse propagation constant. Note that, for the non-leaky, confined propagating modes that we consider here

$$n_{\text{core}} > n_{\text{modal}} > n_{\text{clad}}, \tag{14}$$

and hence both k_x and α_x are real-valued. This requirement is a direct consequence of the fact that non-leaky confinement in an unshielded dielectric waveguide is founded upon total internal reflection, which only occurs if the ray originates from the higher-index side of a dielectric boundary. If, on the other hand, the cladding were of a higher index than the core, then finite transmission would occur at each instance of ray reflection at the core's edge, causing progressive leakage loss.

1. Slab waveguide, TE-modes

For TE slab-modes, the electric field component is wholly parallel to the slab boundary, i.e., the y-dimension, as shown in Fig. 5(b). Propagation occurs in the z-direction, and the magnetic field has components in both the x- (surface-normal) and z- (propagation) dimensions. The electric field component takes the following form:

$$E_y(x) = \begin{cases} E_{a,1} \cdot \exp\left(-\alpha_x [x - h/2]\right) & \text{if } x \geq h/2, \\ E_c \cdot \cos\left(k_x x + \varphi\right) & \text{if } |x| \leq h/2, \\ E_{a,2} \cdot \exp\left(\alpha_x [x + h/2]\right) & \text{if } x \leq -h/2, \end{cases} \tag{15}$$

where φ is a spatial-shift variable, E_c, $E_{a,1}$, and $E_{a,2}$ are complex amplitudes, and h is the physical thickness of the guide core. The sinusoid pattern in the core is the result of spatial beating between counter-propagating rays, and the exponential decay outside is a regular feature of total internal reflection. To satisfy boundary conditions, this function must be continuous across the index-discontinuities at both surfaces. Thus, by substituting $x = \pm h/2$ into Eq. (15), we obtain the following relationships between the complex amplitude terms:

$$E_{a,1} = E_{a,1} \cdot \exp(0) = E_c \cdot \cos\left(k_x h/2 + \varphi\right), \tag{16}$$

$$E_{a,2} = E_{a,2} \cdot \exp(0) = E_c \cdot \cos\left(-k_x h/2 + \varphi\right). \tag{17}$$

The tangential magnetic field component must also be continuous across the index discontinuities at both surfaces of the slab. Thus, we make use of Faraday's law of induction, having made some simplifications based on the assumption of time time-harmonic waves traveling in nonmagnetic, lossless media free of charges

$$\nabla \times \vec{E} = -\frac{\partial \vec{B}}{\partial t} = -\frac{j\omega}{\mu_0} \frac{\partial \vec{H}}{\partial t}. \tag{18}$$

The curl operation on the left-hand side is also simplified by the fact that the $\vec{E}$-field only has nonzero components in the y-dimension, and so $\nabla \times (\hat{y} \cdot E_y) = -\hat{x} \cdot \frac{\partial E_y}{\partial z} + \hat{z} \cdot \frac{\partial E_y}{\partial x}$, from which we may extract the desired, boundary-tangential component of the magnetic field

$$-\frac{j\omega}{\mu_0} H_z(x) = \frac{\partial E_y}{\partial x} = \begin{cases} -\alpha_x E_{a,1} \cdot \exp\left(-\alpha_x [x - h/2]\right) & \text{if } x \geq h/2, \\ -k_x E_c \cdot \sin\left(k_x x + \varphi\right) & \text{if } |x| \leq h/2, \\ \alpha_x E_{a,2} \cdot \exp\left(\alpha_x [x + h/2]\right) & \text{if } x \leq -h/2. \end{cases} \tag{19}$$

Once again, we equate the terms of this expression at $x = \pm h/2$, from which we obtain, two expressions for the spatial shift term,

$$\varphi = \arctan\left(\pm \frac{\alpha_x}{k_x}\right) \mp \frac{k_x h}{2}. \tag{20}$$

27 October 2023 05:17:16

© Author(s) 2023

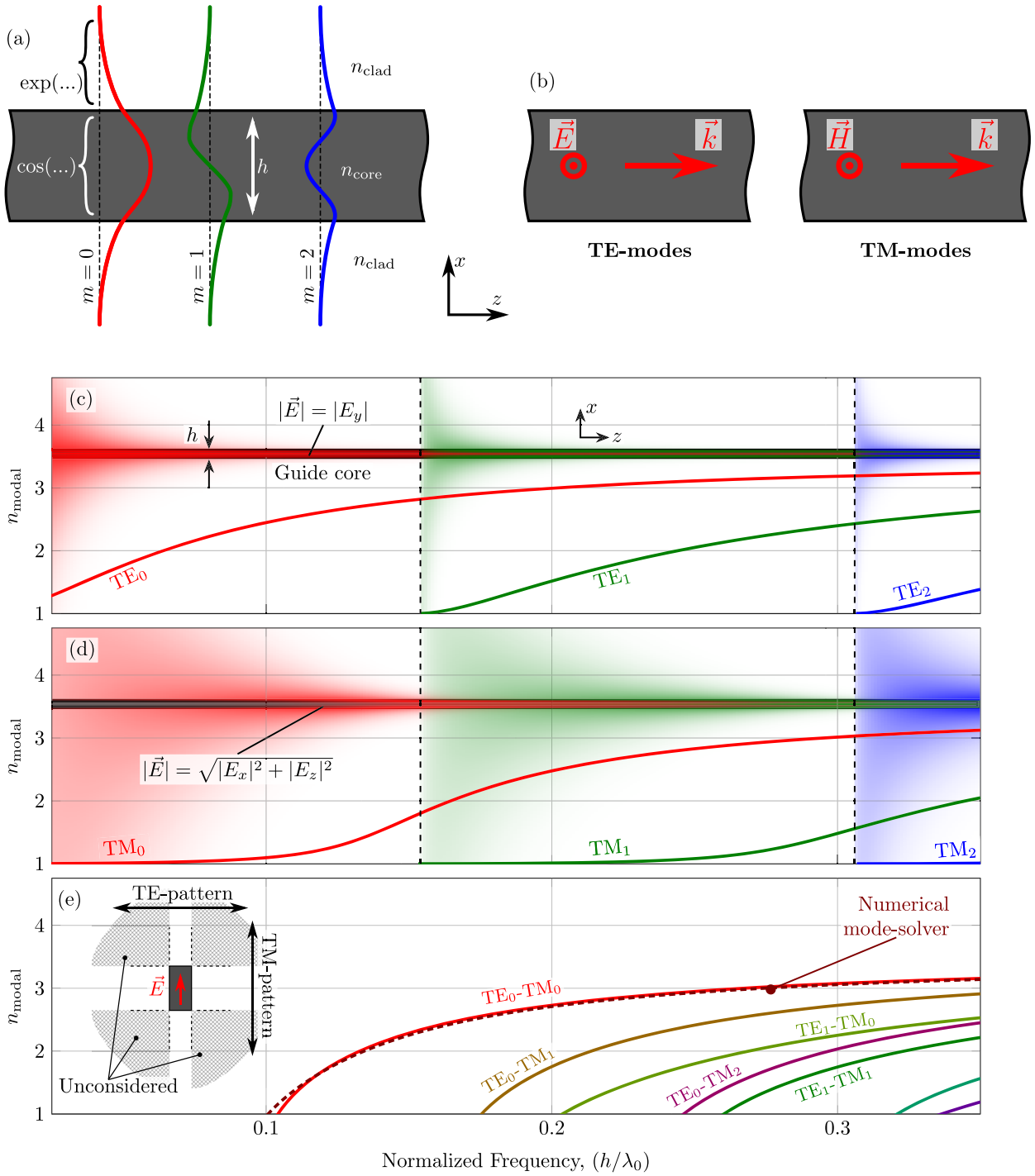

FIG. 5. Illustrated mode definitions for a substrateless dielectric slab, showing (a) numbering convention and assumed function form, and (b) distinction between TE- and TM-modes. Both (a) and (b) share the same Cartesian axis. Modal analysis of (c) a TE, and (d) a TM slab waveguide, with the frequency-dependent modal electric field magnitude distribution shown as inset to the plots. (e) Marcatili's theoretical analysis[181,182] of a dielectric rod waveguide, with the formulation of the problem's geometry illustrated as inset. The fundamental mode is also computed with a full-wave numerical modesolver implemented with CST Studio Suite for comparison. Frequency is given abstractly, in terms of the size of the slab relative to a wavelength, in order to maintain the generality of the theoretical analysis; given that $f = c/\lambda_0$, $f\,[h/\lambda_0] = f\,[\text{Hz}] \cdot h/c$. Thus, the electrical size of slab thickness can be treated as an expression for frequency in alternative units.

27 October 2023 05:17:16

© Author(s) 2023

Equating the two expressions yields the dispersion relation for the fundamental TE_0 mode of the slab waveguide,

$$0 = k_x h - 2 \cdot \arctan\left(\frac{\alpha_x}{k_x}\right). \tag{21}$$

Since Eqs. (12) and (13) show that k_x and α_x are defined by β, the dispersion relation is likewise dependent upon this single variable. The existence of higher-order TE_m modes is accounted for via the observation that each of the two $\tan(\cdots)$ terms in this expression is π-periodic. Thus, there are infinitely many distinct dispersion relations that apply to this guide

$$m\pi = k_x h - 2 \cdot \arctan\left(\frac{\alpha_x}{k_x}\right). \tag{22}$$

The positive integer m designates the number of nodes in the spatial distribution of E_y. This is solved numerically, i.e., by optimizing the value of phase constant, β, to satisfy the dispersion relation. Thereafter, it is straightforward to compute the modal index and field distribution, as shown in Fig. 5(c) for the first three modes: TE_0, TE_1, and TE_2.

There are two salient frequency-dependent effects revealed by the TE modal analysis shown in Fig. 5(c). First, for lower frequencies, modal fields tend to be delocalized outside of the core (i.e., lower value of confinement factor, Γ), which can also be thought of intuitively as a larger wavelength *having trouble fitting* into the waveguide core, being *squeezed* by the slab boundaries, and consequently *spilling out* into the surrounding space. Despite this weakened confinement, these modes are unable to leak or radiate into the surrounding space in the absence of any kind of bend, interruption, or irregularity in the mode volume. It can also be observed that the modal index is decreased alongside the weakening confinement, and this variation in wave speed with respect to frequency is known as *dispersion*. This too makes intuitive sense, as a lesser proportion of modal fields exist within the dielectric volume of the core, and hence we may imagine that the mode is *less slowed-down* by the higher bulk index (i.e., n_{core}) therein. These two phenomena tend to generalize across all-dielectric waveguides of all types; lower frequencies are associated with weaker confinement and faster phase velocity. On the higher-frequency end, the electrical size (i.e., relative to a wavelength) of the slab waveguide is larger, and it can be observed that the TE_1 mode begins to propagate once $h = 0.153 \cdot \lambda_0$. This value is read directly from the modal index plot in Fig. 5(c), as opposed to being obtained through the inversion of a closed-form mathematical expression, because the dispersion relation is itself a transcendental equation that must be solved through numerical optimization. We wish to remark that it is most often favorable to operate a given waveguide below this point, i.e., in its single-mode region. This is because co-propagating modes will travel at different speeds, introducing interference and potentially degrading signal integrity. For intrinsic silicon, the single-mode region of this waveguide is therefore the span from DC up until frequency is equal to $f = 0.153 \cdot c/h$. In practical terms, however, we cannot make use of this entire frequency span because of the extremely weak confinement at low frequencies.

2. Slab waveguide, TM-modes

In addition to TE-modes, it is also of interest to investigate the orthogonal polarization, namely, TM-modes. A very similar procedure of analysis is employed in the latter case, albeit assuming that the only nonzero magnetic field component is in the y-dimension,

$$H_y(x) = \begin{cases} H_{a,1} \cdot \exp\left(-\alpha_x[x - h/2]\right) & \text{if } x \geq h/2, \\ H_c \cdot \cos\left(k_x x + \varphi\right) & \text{if } |x| \leq h/2, \\ H_{a,2} \cdot \exp\left(\alpha_x[x + h/2]\right) & \text{if } x \leq -h/2. \end{cases} \tag{23}$$

The lateral propagation constant terms retain their earlier definitions. In this case, we deploy Ampère's law in order to extract the tangential electric field component, which takes the following form in linear, isotropic, lossless dielectric media of bulk refractive index n,

$$\nabla \times \vec{H} = j\omega\varepsilon_0 n^2 \vec{E}. \tag{24}$$

This leads to the following dispersion relation for the TM-polarized slab mode:

$$m\pi = k_x h - 2 \cdot \arctan\left(\frac{n_{\text{core}}^2}{n_{\text{clad}}^2} \cdot \frac{\alpha_x}{k_x}\right). \tag{25}$$

At this point, the key distinction of this analysis from the dispersion relation of TE-modes [Eq. (22)] becomes apparent; Ampère's law has extracted the bulk index of the core- and cladding-materials, ultimately introducing them as additional factors in the dispersion relation. As a consequence, the TM mode tends to exhibit weaker confinement and a lower modal index for a given slab-thickness, as can be seen in Fig. 5(d).

3. Rectangular dielectric waveguides using Marcatili's approximation

Having analyzed the confined modes of air-clad dielectric slab waveguides, we now return to dielectric rod waveguides. This is a class of channel waveguide, which is a general term for any dielectric waveguide that exhibits index variation in both transverse dimensions. This is in contrast to slab waveguides, which exhibit index variation in only one transverse dimension (the x-dimension), and are therefore wholly unconstrained in the plane of the slab (i.e., the yz-plane), allowing for free-space-beam-like propagation in these two dimensions. For this reason, the guide itself does not clearly define a propagation direction, and the actual trajectory followed by guided waves is the result of the initial y-dimension field distribution launched into the guide, subject to in-plane diffraction according to Huygens' principle.[183] On the other hand, a channel waveguide can indeed constrain the number of propagating modes in both transverse dimensions, and in doing so, restricts propagation to a single well-defined direction that is orthogonal to the two-dimensional cross section of the waveguide. In the context of integrated systems, this means that dielectric channel waveguides are generally of greater value and interest than slabs, as they facilitate convenient routing in a planar circuit, serving as general-purpose interconnect, or "wires," between components. That is not to say that slab waveguides are of no value whatsoever, in fact they have several terahertz-range uses that will be discussed in Secs. VII C and VIII B,

27 October 2023 05:17:16

© Author(s) 2023

and in the nanophotonic range, they are the basis for arrayed waveguide gratings[184,185] and echelle gratings,[186] which are required for frequency-channelization in lightwave technologies. Nevertheless, dielectric channel waveguides are more generally useful. Unfortunately, however, the analysis of channel waveguides is markedly less straightforward than that of slabs, and so we must either employ of fully numerical methods to extract modal fields, as in Fig. 4, or make use of simplifying approximations. Having already pursued the former approach, we now present the latter.

We make use of Marcatili's method,[181,182] which approximates the modal field distribution as a pair of separable spatial functions that each varies in only one transverse dimension, and thereby renders the analysis tractable. The cross-sectional modal field distribution is treated as the product of two one-dimensional functions, one being a function of x and the other a function of y, and both of these spatial functions are simply the field distributions of different slab modes. In order to maintain consistency with the analysis in Fig. 4, we consider a rectangular cross section waveguide of 2:1 aspect ratio, for which the electric field is polarized tangentially to the long-edge, as illustrated in the inset to Fig. 5(e). In this case, the y-dimension function corresponds to the field pattern of a TE slab-mode, and the x-dimension is a TM-mode in a slab of double thickness. The corner-external regions are left unconsidered in this analysis because they do not provide any boundary conditions that are relevant to the constituent slab modes. According to Ref. 182, these conditions/approximations allow us to write

$$\beta_{\text{channel}} = \sqrt{(k_0 n_{\text{core}})^2 - k_{y,\text{TE}}^2 - k_{x,\text{TM}}^2}, \tag{26}$$

where $k_{x,\text{TM}}$ is the transverse propagation constant in the double-thickness TM slab, and $k_{y,\text{TE}}$ is the transverse propagation constant in the orthogonal dimension. Substituting Eq. (12) reduces this expression to

$$\beta_{\text{channel}} = \sqrt{-(k_0 n_{\text{core}})^2 + \beta_{\text{TE}}^2 + \beta_{\text{TM},2\cdot h}^2}. \tag{27}$$

The result of this approximation is shown in Fig. 5(c) for several propagating modes, and it can be seen that the dependence of modal index upon frequency is inherited from the slab waveguides upon which this approximation is based.

It is of interest to validate the analytical model of the channel waveguide, and as the fundamental mode is generally of the most interest to practical applications, we make use of it as an example case. Modal index is computed using the numerical mode solver that is included in the commercial full-wave simulation software package CST Studio Suite, as in the case of the insets to Fig. 4, and the result is plotted in Fig. 5(e). It can be seen that very close agreement is obtained, validating Marcatili's method. Note that higher-order modes are not considered in this comparison as it would introduce visual clutter while providing little additional insight.

The upper limit of the single-mode bandwidth is constrained by the onset of higher-order modes. The lower-frequency end is also constrained by the de-localization of modal fields into the surrounding space, which ultimately renders the guide leaky once the modal index falls below $n_0 = 1$ (i.e., free-space), in a non-leaky-to-leaky transition called "crossing the light-line." Bearing these constraints in mind, a frequency range from $h = 0.11 \cdot \lambda_0$ to $h = 0.175 \cdot \lambda_0$ is given as a guideline for the specific channel-guide geometry considered here. This is a 45% span of relative bandwidth, but it is good practice to leave a modest margin, and so the practical, usable single-mode range is ~40%. Thus, if $h = 200\ \mu$m, then the recommended operation range will be from 165 to 250 GHz, and for $h = 100\ \mu$m, it is from 330 to 500 GHz, although it is noted that these particular values only hold for a pure silicon core of this specific aspect ratio.

B. The development of terahertz-range dielectric rod waveguides

This section describes the engineering advances that supported the translation from the theoretical analyses such as that which is presented above toward practical demonstrations of terahertz-range dielectric rod waveguides composed of pure silicon. Much of the work described here was performed below 100 GHz and made use of dielectrics other than intrinsic silicon, and so it is not all strictly within the topic scope of this article. However, it is included to provide a broader and more complete context for the development of the relevant terahertz-range technology.

1. Tapered termination

Interfaces are required in order to utilize any given waveguide structure as interconnect, or else there will simply be no way to launch or receive the guided mode. In the context of dielectric waveguides, this is a question of index-matching the high effective index of the guide, n_{modal} to the unity-index of free space, $n_0 = 1$, in order to suppress reflections. To this end, we observe in Figs. 5(c)–5(e) that modal index is dependent upon the electrical size of the guide's cross section, with a thinner waveguide having a lower index. In the extreme case, the guided-mode index of a narrow channel guide will cross the light-line and leak spontaneously into the surrounding space. In other words, a sufficiently electrically narrow dielectric waveguide will cease to behave as a waveguide, and will begin to operate as an antenna. Fortunately, it is very convenient to transition between the well-confined wide waveguide and the free-space-matched narrow guide; all we need to is longitudinally taper the guide section over a distance of a few wavelengths, forming a spike. As early as the post-war period of the 1940s, linear tapers were being used to radiate the guided mode of a microwave-range dielectric rod waveguide composed of polystyrene, for end-fire antennas.[187]

Aside from antennas, the tapered-spike structure is also the fundamental basis of port-coupling to hollow metallic waveguides, which is of critical importance as a near-field interface to terahertz instrumentation systems.[120–122] The guided mode of a hollow waveguide is a fast-wave, meaning that its modal index is lower than that of free-space, and hence is certainly lower than that of a non-leaky dielectric waveguide. Thus, from the perspective of a dielectric waveguide, the problem of index-matching is essentially the same as in the case of free-space; we must transition to a faster wave, and so we can likewise use a tapered-spike termination. Efficient coupling is achieved by inserting the spike directly into the empty space that comprises the inner volume of the hollow metallic waveguide such that the energy that is radiated from the tapered spike will be injected directly into the hollow guide. As with tapered dielectric rod antennas, this manner of tapered-spike coupler was first

27 October 2023 05:17:16

© Author(s) 2023

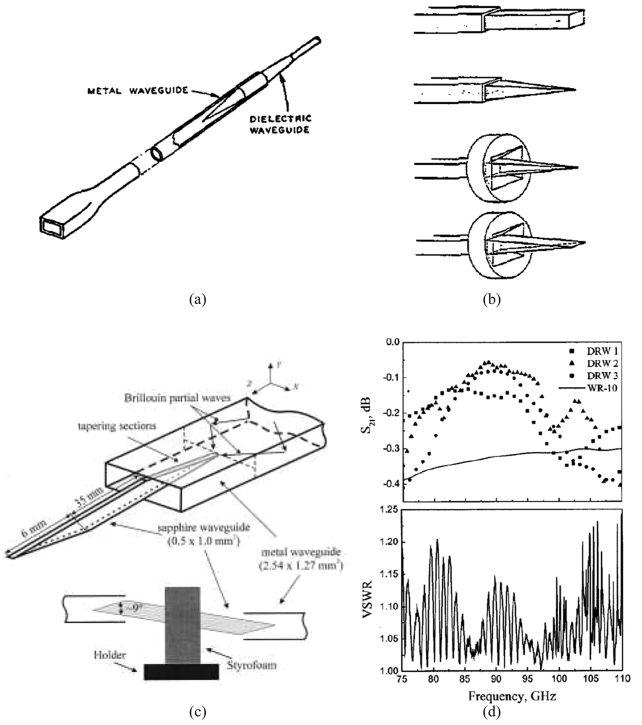

FIG. 6. The historical development of dielectric rod waveguides for terahertz frequencies, showing (a) a cylindrical polystyrene rod that serves as a microwave-range dielectric rod waveguide, and is coupled to a circular hollow metallic waveguide by means of a cylindrical tapered spike for index-matching, reproduced with permission from C. Chandler, J. Appl. Phys. **20**, 1188–1192 (1949). Copyright 1949 AIP Publishing LLC; (b) a systematic study into various different taper and feed-horn shapes for Teflon millimeter-wave end-fire antennas operating in the vicinity of 80 GHz, from S. Kobayashi, R. Mittra, and R. Lampe, *Proceedings of the Antennas and Propagation Society International Symposium*. Copyright 1980 IEEE. Reproduced with permission from IEEE; and [(c) and (d)] a dielectric rod waveguide composed of sapphire that is capable of operation above 100 GHz, i.e., the terahertz-range, reproduced with permission from Lioubtchenko *et al.*, IEEE Microwave Wireless Compon. Lett. **11**, 252–254 (2001). Copyright 2001 IEEE. None of these studies made use of intrinsic silicon as the core dielectric, but they nonetheless cemented many of the engineering conventions of contemporary substrateless all-silicon photonic devices.

demonstrated in the microwave range in the 1940s, using a low-index polystyrene taper inserted into circular metallic waveguides,[188] as shown in Fig. 6(a). This port coupling facilitated the exploration of these dielectric guides as interconnect in microwave-range circuits, with consideration paid to the implementation of resonators and bend structures. Subsequent years saw the same manner of cylindrical tapered-spike coupler used to feed microwave-range dielectric antennas,[191] and by the 1960s, a rectangular cross-sectional profile had been adopted for both guides.[192]

2. Reaching higher frequencies

Following the initial microwave-range demonstrations of dielectric rod waveguides, translation to the millimeter-wave region was facilitated by low-loss polymer dielectrics, such as Teflon,[193] which opened the door to operation at frequencies as high as ~80 GHz. This supported investigations into optimized taper structures for millimeter-wave antennas,[189] as shown in Fig. 6(b). This study, along with others from that period,[194] also looked into flaring the output of the metal waveguide at the launching point of the dielectric waveguide mode in order to avoid the sharp discontinuity in modal cross section area at the mouth of the hollow metallic waveguide, which is a consequence of the weakly confined mode's evanescent fields suddenly expanding into the unconfined surrounding space after the hollow guide is terminated. However, this particular refinement is only really necessary because of the low index ($n \sim 1.4$) of the Teflon dielectric. On the other hand, if a higher-index dielectric were employed then the resultant stronger field confinement would render this flared transition unnecessary.

By around the time of the turn of the millennium, dielectric rod waveguides reached operation frequencies of more than 100 GHz, and thus entered into the terahertz range.[190,195] This was enabled in part by the use of higher-index low-loss dielectric materials, such as sapphire ($n > 3$),[190] as shown in Figs. 6(c) and 6(d), as well as gallium arsenide.[195] It can be seen that, in addition to low propagation loss, highly efficient coupling from the hollow metallic waveguide is indeed achieved without the use of a flared metallic waveguide, owing to the strong field confinement within the high-index core. Not only that ceramics and intrinsic semiconductors also exhibit a more physically rigid and robust structure at the small, micro-scale core dimensions that are required for single-mode operation in the terahertz range. On the other hand, it can also be seen in Fig. 6(c) that the high-frequency sapphire dielectric rod waveguide now requires a dielectric support structure that is composed of styrofoam, as the smaller-core, higher-index dielectric can no longer be simply held by the walls of the hollow guide, as in the low-index-core example in Fig. 6(a).

C. Demonstrations of silicon dielectric rod waveguides in the terahertz range

High-frequency dielectric rod waveguides translate very naturally to intrinsic silicon as its properties are similar to those of sapphire, and this brings dielectric rod waveguides more firmly into the purview of this article. Utilizing silicon for the core dielectric also has notable supply-chain benefits, as silicon is a lower-cost[196] and more-plentiful material. Silicon dielectric rod waveguides were initially utilized for end-fire antennas operating in the frequency range from 110 to 150 GHz,[197] as shown in Fig. 7(a), and it can be seen that the device is affixed to the flange-coupler using a low-index styrofoam support structure during characterization of antenna performance. Thus, the first all-silicon waveguide for terahertz waves was an end-fire antenna, which incidentally mirrors the development of the polystyrene microwave-range devices that came before, in the 1940s. This manner of end-fire all-silicon antenna was later deployed in the frequency range from 220 to 325 GHz by reducing the cross-sectional guide dimensions.[198]

Aside from antennas, silicon dielectric waveguides have also been deployed as point-to-point interconnect between hollow metallic waveguides in a manner that is quite similar to that which is illustrated in Fig. 6(c).[190] For instance, one systematic study investigated progressive step transitions as an alternative to linear tapers,[199] as shown in Figs. 7(b) and 7(c). It was found that a

27 October 2023 05:17:16

© Author(s) 2023

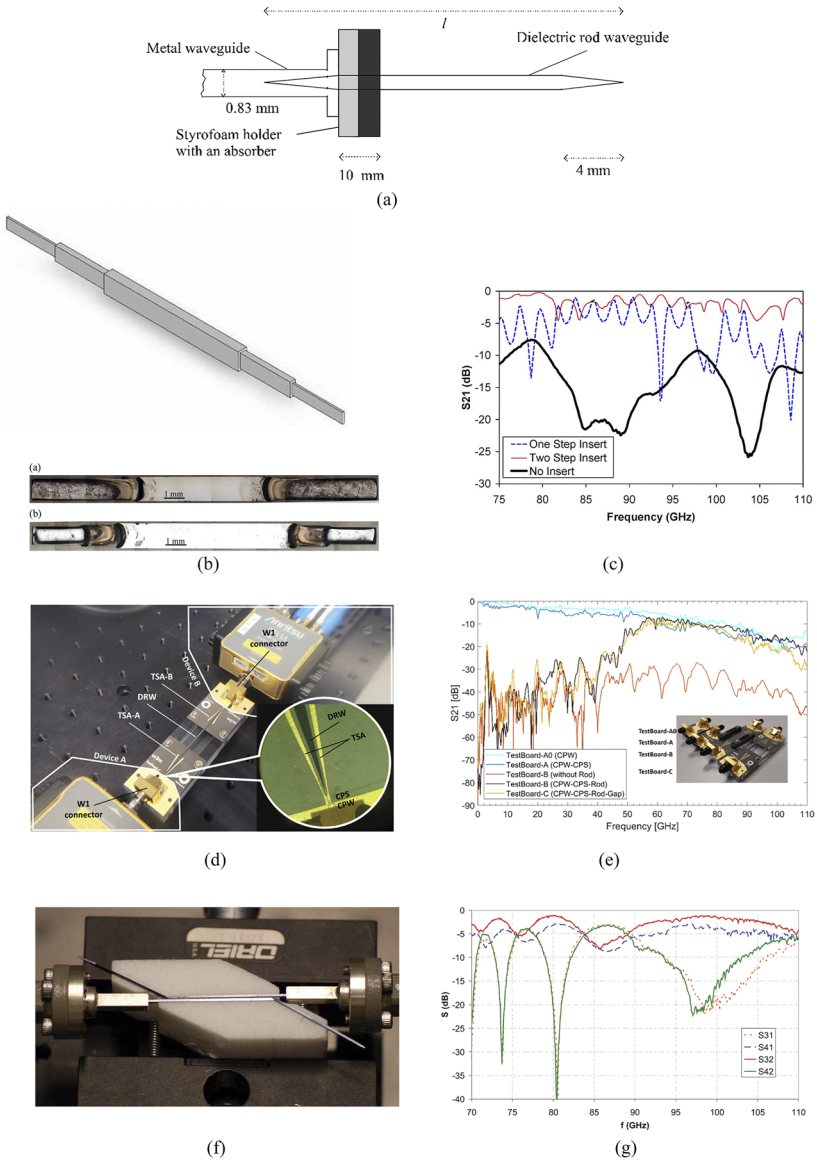

FIG. 7. Demonstrations of all-silicon dielectric rod waveguides that operate at frequencies in the vicinity of 100 GHz and beyond, showing (a) a dielectric rod waveguide as an end-fire antenna, from Ref. 197; [(b) and (c)] an exploration into the possibility of step-taper transitions, as opposed to wedge-shaped linear tapers, reproduced with permission from Marconnet *et al.*, IEEE Trans. Electron Devices **56**, 721–729 (2009). Copyright 2009 IEEE; [(d) and (e)] dielectric rod antenna-based broadband board-to-board interconnect that makes use of a tapered slot antenna structure as opposed to the more-conventional hollow-waveguide launcher, from Ref. 78; and [(f) and (g)] a demonstration of frequency-dependent contactless power transfer between two dielectric rod waveguides that are arranged together upon a polystyrene block, from Ref. 200.

two-step taper outperforms a single step, likely because it is a closer approximation of a progressive linear taper transition. Another study exploited the unshielded nature of the guide for tunable sidewall loading, and demonstrated that a MEMS-actuated high-impedance surface brought into the guide's proximity could serve as a phase shifter with a maximum tuning range of 32°.[201] This technique is wholly dependent upon the existence of evanescent fields that extend outside the bounds of the waveguide core, and so it cannot be extended to shielded guides such as hollow metallic waveguides.

A hollow waveguide is not the sole viable means to launch the guided mode of an all-silicon terahertz dielectric rod waveguide. One recently demonstrated planar alternative is a broadband V-shaped tapered slot antenna,[78] allowing the dielectric rod waveguide to serve as interconnect between two physically separated boards, as shown in Figs. 7(d) and 7(e). The use of a broadband cou-

27 October 2023 05:17:16

© Author(s) 2023

pler accommodated relative bandwidth beyond the 40% of hollow metallic waveguides, but it is noted that this engenders a conscious choice to operate the dielectric rod waveguide in its over-moded region, and so care must be taken to avoid exciting undesired higher-order modes. That study also the possibility of explored contactless power transfer, i.e., with an airgap between the waveguide and the receiving board, which was enabled by the evanescent fields that surround the dielectric waveguide. A similarly contactless power transfer technique may also be achieved between two dielectric rod waveguides by bringing them into proximity, and allowing the frequency-dependent transfer of power via evanescent fields,[200] as shown in Figs. 7(f) and 7(g). It is noted that this airgap-transfer technique will be discussed in greater detail in Sec. VIII B, as its innate frequency-dependence can be exploited to realize frequency-division diplexers, but have included it in in the present section because the study illustrates a certain fundamental and important limitation of dielectric rod waveguides: the absence of any kind of physical support for the waveguide core.

The two lines of the near-field coupler shown in Fig. 7(f) are separate, disconnected, individual pieces of silicon that must be physically placed into close proximity with each other in order to transfer terahertz waves across the airgap. As a consequence, the waveguide core itself must be manually handled during positioning, which innately engenders risk of breakage, as the guide is essentially just a micro-scale "hair" of crystalline material. Furthermore, this risk would be markedly exacerbated if miniaturization of core dimensions were attempted in order to achieve higher-frequency operation. The manual assembly also renders it extremely challenging to accurately ensure a specific micro-scale airgap width, and these difficulties would multiply if more than one such airgap coupler were included in the circuit. As such, an accurate structure could only really be assured in a device without any airgaps, and instead exhibits a single united waveguide core. This significantly restricts the achievable complexity of integrated circuits that may be implemented in this platform, which accounts for the prevalence of straight waveguides in the dielectric rod waveguide literature, both as fixed point-to-point interconnect and as end-fire antennas. Furthermore, the assembly of the two disconnected lines must necessarily be performed upon some form of physical support structure, table, or board, such as the styrofoam support in Figs. 6(c), 7(a), and 7(f), and the circuit board in Fig. 7(d). In electromagnetic terms, this lower-index material can essentially be considered equivalent to a "substrate," and so terahertz-range dielectric rod waveguides cannot be considered "substrateless" in a strict sense.

V. FRAME-TETHERED GUIDE

It would be greatly beneficial to integrate some form of physical support directly together with the waveguide core, without compromising the substratelessness that yields the great efficiency advantage that is shown in Fig. 4. One prospective avenue to achieve this is in-plane support that is *also made of low-loss silicon*, and so it can be fabricated *together with the integrated guide*. The selection of an appropriate means of support is a serious engineering consideration, and so is a major focus for the remainder of this tutorial.

One prospective avenue for in-plane support is to attach the guide to an adjacent frame structure with integrated tethers (also called "anchors"), which are narrow beams of intrinsic silicon, as shown in Fig. 8. This enables handling without the need for physical contact with the guide core, and it also facilitates practical packaging structures,[152,204] as shown in Figs. 8(a) and 8(b). The frame rests upon shelves that are built into the package, holding the guide core suspended above a trench, preventing interaction between the waveguide core and the material of which the package is composed. The supporting tethers have also significantly increased the viable structural complexity, yielding compact bends,[202] as shown in Figs. 8(c) and 8(d), as well as spirals.[203]

Given that the tethers are composed of exactly the same material as the waveguide core with which they are in physical contact, guided waves will experience each pair of tethers as a momentary expansion of the core's cross-sectional width. This irregularity in core dimensions has the potential to introduce loss through radiation, in-guide reflections, and could even form an unwanted waveguide itself if the tethers were wide enough. In order to mitigate this loss, the tethers are generally made as narrow as possible while maintaining physical structural viability; smaller tethers are invariably weaker. This critical trade-off is numerically explored in detail in Ref. 203, as shown in Figs. 8(e) and 8(f), and a tether that is about ten percent of the width of the guide is found to be appropriate. For the chosen configuration, each pair of tethers causes ~0.04 dB loss, and the separation between adjacent pairs is 1.5 mm. Thus, the tethers alone contribute ~0.3 dB/cm to progressive loss. For comparison, the propagation loss of a moderate-purity silicon guide surrounded by free-space would be ~0.1 dB/cm, according to Fig. 4. Conversion to linear units reveals that, after 1 cm of propagation, ~7% of the initial power has been lost due to the tethers, while only ~2% is intrinsically dissipated by the guide core. The total loss is therefore ~9%, and Fig. 4 shows that the computed loss of a hollow metallic waveguide over the same distance is ~13%. We may conclude from this rough analysis that the physical structure of the frame-tethered guide contributes significantly higher loss than the absorption of the materials from which it is constructed, rendering its performance broadly comparable to that of a hollow metallic waveguide—and in a markedly more fragile structure. This fragility may be improved somewhat by strengthening the tethers, but this will inevitably increase the progressive loss; if either the tether width is increased to 50 μm or the pitch is reduced to 0.7 mm, then the loss due to the tethers alone will exceed that of a hollow metallic waveguide. Thus, the use of integrated supporting tethers unfortunately appears to largely undermine the primary advantage of substrateless all-silicon guides, i.e., efficiency. On the other hand, other advantages such as compactness, cost-effective manufacture, convenient routing, and the versatility of viable functional devices, still apply.

VI. PHOTONIC CRYSTAL TECHNIQUES

It is desirable to provide support to the waveguide core without compromising the low loss that makes all-intrinsic-silicon so attractive. It would therefore be beneficial to avoid irregularities in the guide core, and instead clad the guide width some manner of homogeneous medium. However, this article is solely concerned with *all-silicon* structures; how might we construct a suitable cladding using only a single material? The answer is to use *regular lattice* structures, such as a photonic crystal. In this section, we explore the possibility of cladding an all-silicon terahertz guide with such

27 October 2023 05:17:16

© Author(s) 2023

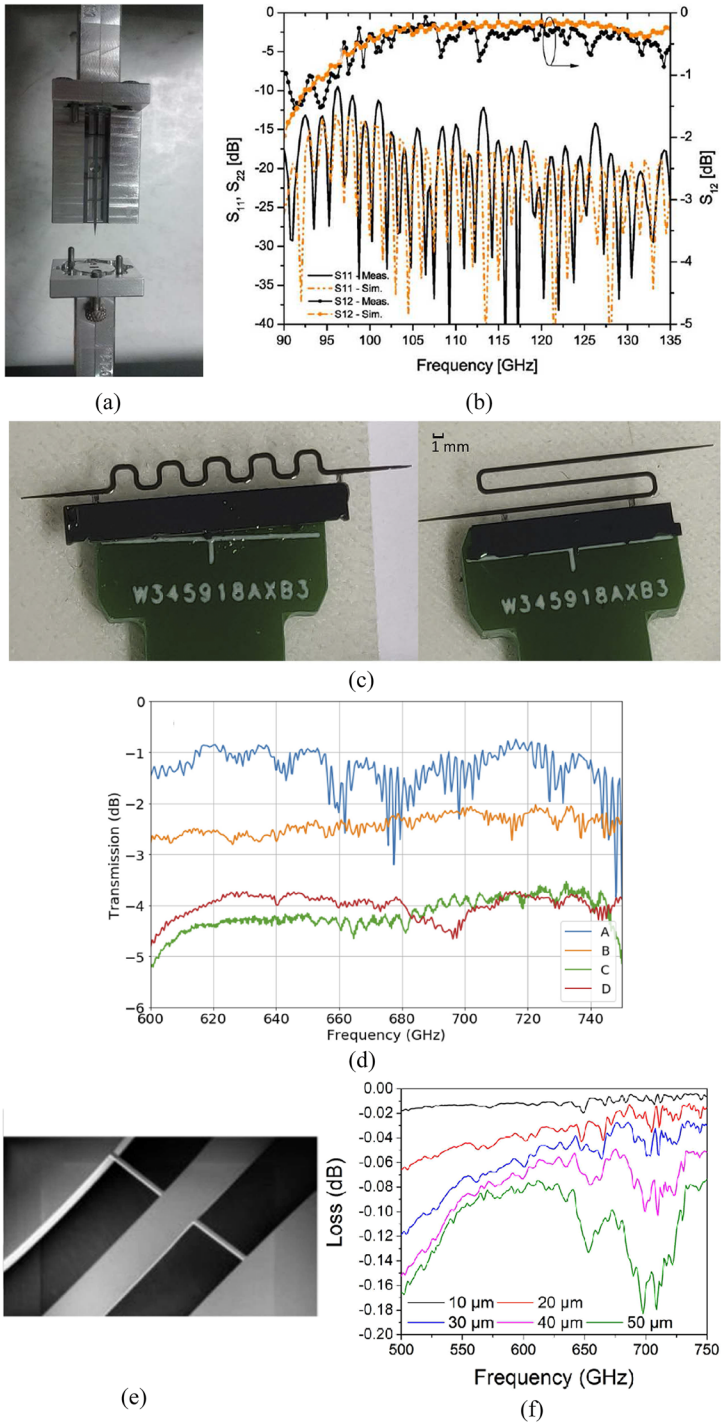

FIG. 8. A selection of waveguide devices that are affixed to supporting frames using arrays of narrow integrated tethers, showing [(a) and (b)] a straight waveguide for the millimeter-wave range, reproduced with permission from Malekabadi *et al.*, IEEE Trans. Terahertz Sci. Technol. **4**, 447–453 (2014). Copyright 2014 IEEE; (c) bend structures and (d) associated measured transmission, reproduced with permission from Verstuyft *et al.*, Opt. Express **30**, 6656–6670 (2022). Copyright 2022 Author(s), licensed under a Creative Commons Attribution 4.0 License; (e) an micrograph of a supporting tether for a terahertz-range waveguide; and (f) associated numerical study into the relationship between tether width and insertion loss, for a guide that is 90 μm-thick and 210 μm-wide, reproduced with permission from Akiki *et al.*, IEEE Trans. Terahertz Sci. Technol. **11**, 42–53 (2021). Copyright 2021 IEEE.

27 October 2023 05:17:16

© Author(s) 2023

a medium, but first we must introduce the concept of photonic crystals.

A. A brief introduction to terahertz-range photonic crystals

Photonic crystals are a light-wave adaptation of the wave mechanics of quantum particles within the crystalline structure of a semiconductor material, and, in particular, the phenomenon known as an "electronic bandgap."[209] The fundamental concept of a photonic crystal is to *artificially pattern* a given dielectric material with a periodic lattice structure in order to mimic the phenomenon of an electronic bandgap at a larger physical scale, yielding a medium in which light within a certain wavelength range cannot propagate. This idea was concurrently conceived of in 1987 by two independent scientists with different motivations. Eli Yablonovitch was seeking to improve the efficiency of lasers, which suffered significant loss due to spontaneous emission of undesired photons, and so a "photonic bandgap" offered as a way to inhibit this phenomenon.[210] John, on the other hand, sought to trap light within a defect in the lattice.[211] These two remarkable gentlemen jointly agreed that "photonic crystal" was the appropriate term for this theoretical medium, and with that, an entire field of research was born. A few years later, Yablonovitch reported the first artificial photonic crystal, complete with an experimentally verified photonic bandgap, by drilling a three-dimensional periodic hole structure into alumina,[205] as shown in Figs. 9(a) and 9(b). In later years, the concept was adapted to a perforated two-dimensional slab structure,[212,213] and facilitated the experimental realization of Yablonovitch's original vision and motivation, namely, the inhibition and control of spontaneous photon emission,[206,214] as shown in Figs. 9(c) and 9(d).

The first experimental demonstration of a terahertz-range photonic crystal was reported[207] during the intervening half-a-decade between the first microwave-range photonic crystal[205] and early light-wave photonic crystals.[212,213,215] As shown in Figs. 9(e) and 9(f), this demonstration made use of a three-dimensional microscale woodpile structure composed of intrinsic silicon. We will henceforth focus upon terahertz-range demonstrations of photonic crystals, as opposed to optical-range, as such work is somewhat tangential to the focus of the review, and is only included due to its historical significance. If readers are interested in the topic, a number of exemplary review articles have been dedicated to nanoscale photonic crystals for the manipulation of light-waves.[216–218]

Following the initial demonstration of a terahertz-range three-dimensional woodpile photonic crystal,[207] a two-dimensional photonic crystal was implemented by drilling an array of through-holes into a low-loss plastic dielectric.[219] This two-dimensional through-hole lattice was later implemented in an intrinsic silicon wafer,[220] essentially hybridizing the two aforementioned early terahertz-range demonstrations, and it was at this point that the photonic crystal structures that are most directly relevant to the subject of this tutorial began to take shape. In that work, the photonic crystal medium was enclosed within a metallic parallel-plate waveguide in order to allow for excitation with a free-space beam. However, the presence of metal engenders undesired Ohmic dissipation, and so subsequent work employed specialized quasi-optical apparatus in order to impinge a terahertz beam upon the edge of an all-intrinsic-silicon photonic crystal slab, for a truly substrateless photonic crystal structure that is wholly free of metals,[208] and is shown in Figs. 9(g) and 9(h). This paved the way for demonstrations of bandgap tailoring via physical lattice parameters,[221] drawing attention to the versatility of terahertz photonic crystals. In terms of practical applications, it has been found that the light-trapping properties of photonic crystal can serve for a high-quality absorber of terahertz waves,[222] in order to suppress standing waves in applications of terahertz-range communications. In addition, the aforementioned bandgap-tailoring techniques can be combined with this manner of absorber in order to realize a terahertz-range version of a contactless tag reader.[223]

B. Demystifying photonic band diagrams

Photonic band diagrams are the primary tool for understanding the electromagnetic properties of a photonic crystal in an abstract way, i.e., as a medium, as opposed to studying wave propagation through a finite-sized piece, as in Fig. 9. This manner of plot was originally developed to study the behavior of quantum-mechanical particles in a crystalline medium,[224,225] and was later adapted to photonic crystals,[226,227] and so is not just a useful tool; it is also evidence of the lineage of this field, and the translation from semiconductor physics to lightwave engineering. That said, photonic band diagrams are a fairly esoteric plotting convention that is not always immediately intelligible to non-experts, and for this reason, we will provide a brief explanation here.

Photonic band diagrams are founded upon Bloch's theorem,[228] which states that all solutions to the wave equation in a periodic lattice must also be periodic, and of the same manner of periodicity and symmetry as that lattice, albeit allowing for finite phase shift between adjacent cells. His original work pertained to the quantum-mechanical behavior of electrons in a molecular crystal lattice, but the result generalizes to the behavior of electromagnetic waves in the larger-scale artificial crystals that are of interest to us here. As a consequence, the field distributions within a photonic crystal can be decomposed into the product of a periodic "envelope" distribution and a phase shift term. This latter term is determined by the Bloch wavevector, $\vec{\beta}$, which is the phase shift across adjacent cells divided by the physical separation there between. The Bloch wavevector can therefore be viewed as equivalent to the phase constant that is given in Eq. (10), but as a multi-dimensional quantity with components in all lattice vector directions. The explanatory example given in Fig. 10(a) is a two-dimensional square lattice for the sole reason that the lattice vectors map to Cartesian dimensions, making the analysis markedly more intuitive. However, we wish to remark that the same treatment can readily be applied to other classes of periodic structure, such as the triangular lattices displayed in Figs. 9(c) and 9(g).

Bloch's theorem allows us to extract a complete description of wave propagation within a photonic crystal of infinite extent by simply analyzing a single unit cell of the structure. All we need do is interpret Bloch's theorem as a set of electromagnetic boundary conditions that enclose that single period: the field must be expressible as the product of a complex amplitude term and a spatial phase shift given by the Bloch wavevector. The resultant solution is a set of eigenmodes, each at specific frequencies, which are indexed by

27 October 2023 05:17:16

© Author(s) 2023

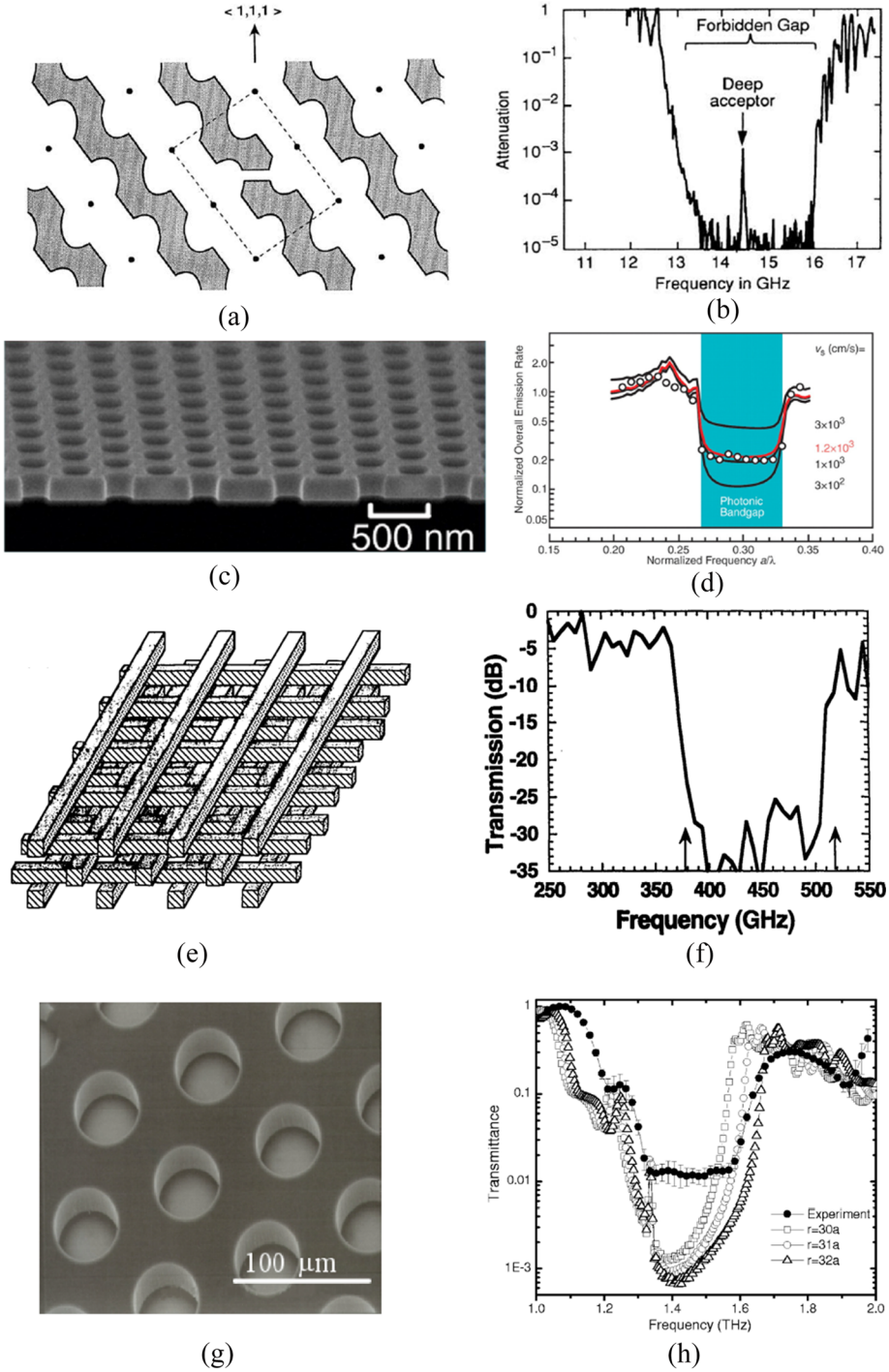

FIG. 9. Evolution from the original demonstration of a photonic crystal structure to the first all-silicon substrateless photonic crystal slab, showing [(a) and (b)] the world's first artificial photonic crystal, which exhibited a microwave-range bandgap, reproduced with permission from Yablonovitch *et al.*, Phys. Rev. Lett. **67**, 3380 (1991). Copyright 1991 American Physical Society; [(c) and (d)] experimental demonstration of inhibited spontaneous emission within a two-dimensional photonic crystal slab, where measured data points are shown as circles, and exhibit closest correspondence to theoretical prediction when surface recombination velocity is $v_s = 1.2 \times 10^3$ cm/s, from Ref. 206; [(e) and (f)] the first terahertz photonic crystal, made of silicon, Reprinted with permission from Özbay *et al.*, Opt. Lett. **19**, 1155–1157 (1994). Copyright 1994 Optical Society; [(g) and (h)] the first substrateless all-silicon photonic crystal slab medium for terahertz waves, reproduced with permission from C. Yee, N. Jukam, and M. Sherwin, Appl. Phys. Lett. **91**, 194104 (2007). Copyright 2007 AIP Publishing LLC.

27 October 2023 05:17:16

© Author(s) 2023

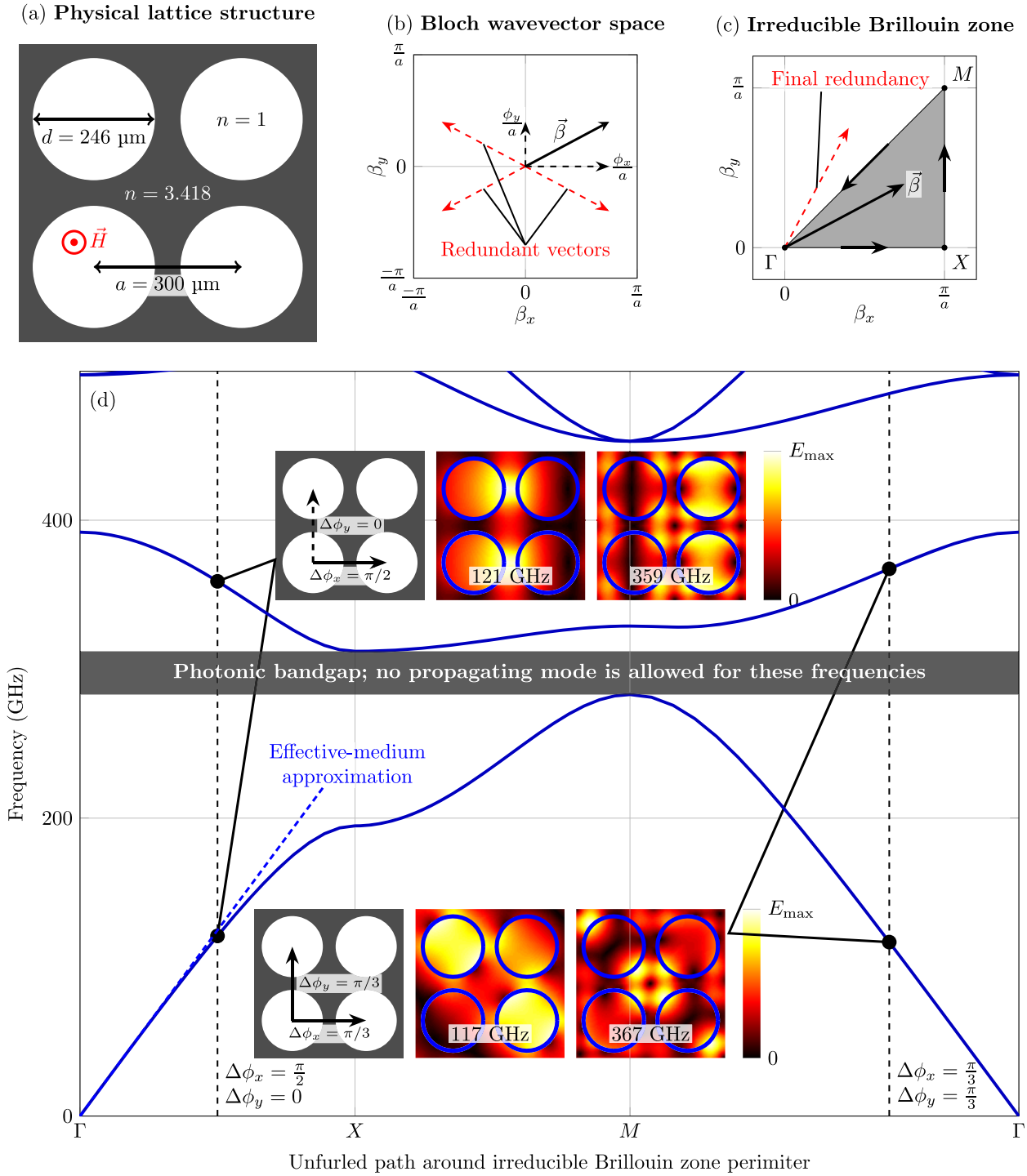

FIG. 10. An explanatory example of a simple square-lattice 2D photonic crystal, showing (a) the physical structure in question, showing the orientation of the magnetic field vector component; (b) the Bloch wavevector space, including an example Bloch wavevector and illustration of other vectors that are redundant therewith due to various symmetries in the lattice; (c) the irreducible Brillouin zone within the Bloch wavevector space, with an illustration of the final redundancy to be removed in order to arrive at this irreducible zone; and (d) the resultant photonic band diagram, calculated with CST Studio Suite's eigenmode solver. Each point on the horizontal axis is associated with one of the two-dimensional Bloch wavevectors on the perimeter of the irreducible Brillouin zone. Insets show the phase shift across adjacent cells together with the first two propagating modes.

27 October 2023 05:17:16

© Author(s) 2023

Bloch wavevectors. By repeating this procedure for the set of all possible Bloch wavevectors, we obtain the aforementioned complete description.

At this point, it is useful to note certain forms of degeneracy that enable us to reduce the problem space. First, in terms of boundary conditions, a phase shift of $\Delta\phi$ between adjacent cells is equivalent to $\Delta\phi + 2\pi$, and so there is an infinite number of higher-order modes that also satisfy the same boundary condition. Thus, the Bloch wavevector is wrapped in the range from $-\pi/a$ to π/a, never exceeding a 2π phase shifts between adjacent cells. In this way, we obtain the finite-sized Bloch wavevector space that is shown in Fig. 10(b). The second form of degeneracy that we exploit is rotational symmetry, as the backward-propagation is equivalent to forward-propagation when viewed from a different angle (i.e., 180° rotation of the lattice), and so the negation of a given Bloch wavevector can be disregarded as redundant. This allows us to exclude the entire double-negative quadrant of the Bloch wavevector space (i.e., $-\pi/a < \beta_x, \beta_y < \pi/a$). In a similar way, the spatial mirror symmetry of the square lattice in the x and y dimensions allows us to disregard the two remaining negative-valued quadrants, leaving us with positive-valued Bloch wavevectors. The final form of lattice symmetry that may be exploited in the remaining double-positive quadrant is reflection in the diagonal line $y = x$, and this leaves us with the triangle that is shown in Fig. 10(c), which is known as the "irreducible Brillouin zone," and is so-named because no further exploitable symmetries remain. Every single Bloch wavevector that is *outside* of this reduced space will therefore be redundant with one that is *inside*, and so the set of eigenmodes that correspond to all Bloch wavevectors inside the irreducible Brillouin zone are a complete description of permissible wave propagation in the photonic crystal lattice structure.

In the context of photonic band diagrams, it is generally considered sufficient to consider only the Bloch wavevectors around the perimeter of the irreducible Brillouin zone, as features of interest will most often occur at the edges, and especially at corners.[229,230] The established convention is to label each vertex of the perimeter of the irreducible Brillouin zone, and then "unfurl" this perimeter into a straight line segment that serves as a unitless, numberless visual index of all Bloch wavevectors under consideration. Finally, solving the eigenmodes of all Bloch wavevectors along this line, and plotting the frequencies at which these modes propagate against the unfurled path around the irreducible Brillouin zone's perimeter, will yield a photonic band diagram such as that which is shown in Fig. 10(d). Because of the aforementioned phase-wrapping of the Bloch wavevector, each such propagating mode exhibits an infinite number of harmonics at higher frequencies, which is why more than one line, or "band," is plotted in the photonic band diagram.

At low frequencies, the fundamental band presents as a straight, diagonal line. This is because the physical structures that comprise the lattice are too small to behave as individual features or scatterers, and so the medium is experienced by an electromagnetic wave as a kind of average of the two constituent media. This is also known as an "effective medium," which is a concept that will be covered in more detail in Sec. VII. As frequency is increased, the fundamental band begins to curve downward, away from the diagonal line of the effective medium approximation, and the physical interpretation of this band-curvature is dispersion. It can also be observed that, due to this curvature, the first and second modes never meet. Thus, not all frequencies are assigned to a specific propagating mode, and this is evident in the photonic band diagram as a *gap* in-between two adjacent bands of propagating modes. This is termed a "photonic bandgap," with the physical interpretation being that wave propagation is not permitted within the photonic crystal for this span of frequencies. This is also the cause of the stopbands that are observed in the transmission responses given in Fig. 9. It merits mention that the photonic bandgap occurs in the vicinity of 300 GHz, and that the 300-μm pitch approximately corresponds to a wavelength in bulk-silicon at this frequency, and to a third of a wavelength in the air medium that fills the holes, and so we may roughly interpolate to a half-wavelength period. We may therefore say that the periodicity of the lattice is of "wavelength-scale," which is a general requirement for the formation of a photonic bandgap, but will correspond to a different absolute physical scale in each specific case, depending upon the materials employed and their physical arrangement.

C. Photonic crystal waveguides

We return now to the topic of waveguiding platforms for terahertz waves. In view of the above discussion, a photonic crystal may seem an unusual choice for this purpose given that its main interesting property is the photonic bandgap, which forbids the propagation of electromagnetic waves, and hence is essentially the opposite of a waveguide. On the other hand, we may think of a photonic crystal as a kind of all-dielectric mirror; a counterpart to the metal walls that enclose hollow metallic waveguides. This allows us to construct very well-defined boundaries that will confine propagating waves within a waveguide core. The core itself is implemented by leaving a single row of cylindrical through-holes absent, thereby creating a narrow track along which the bandgap medium is interrupted, and hence terahertz waves may be allowed to propagate.[231–233] This is called a "defect row," which is a class of "line defect." Similar to the tether structures presented in Sec. V, the photonic crystal is an all-silicon periodic support structure, but in this case, the electromagnetic behavior is more akin to a uniform medium that is impenetrable to terahertz waves, and thus it avoids periodic scattering loss due to irregularities. On the other hand, the fact that this waveguiding mechanism depends upon the existence of a photonic bandgap limits operation to the span of frequencies over which this bandgap can be maintained. Not only that, the cumulative action of the periodic scatterers at either side of the line defect has a tendency to produce dispersion that can accelerate the phase velocity of guided waves beyond that of free-space, thereby crossing the light-line, and becoming leaky. Thus, in practice, a photonic crystal waveguide's operation bandwidth is generally in the vicinity of 10%, meaning that the ratio of operation bandwidth spanned to center frequency is ~ 1/10. For context, the recommended operation range of a hollow metallic waveguide is ~40%.

Photonic crystal waveguides have been demonstrated in the vicinity of 1 THz using 44 μm-thick silicon,[72] as shown in Fig. 11(a), which shows that this material and lattice structure are strong enough to be self-supporting for thickness below 50 μm. Not only that, to our knowledge this is the world's first demonstration of a substrateless all-silicon terahertz waveguide in the literature, as the

27 October 2023 05:17:16

© Author(s) 2023

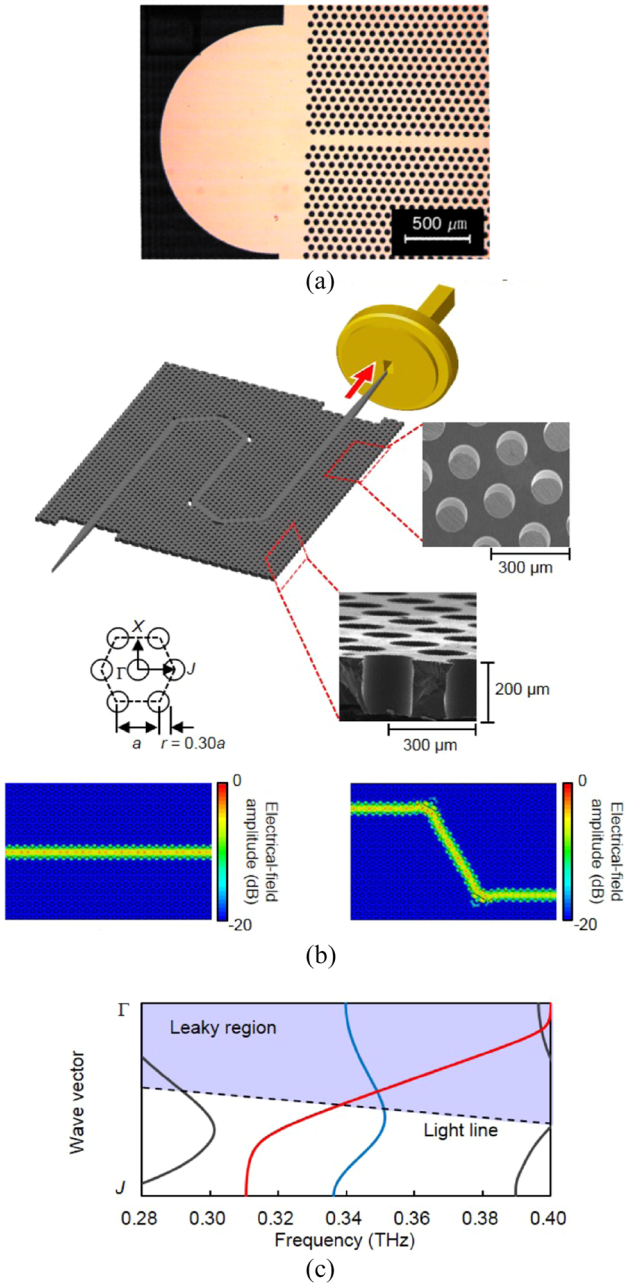

FIG. 11. Self-supporting 2D photonic-crystal waveguides at terahertz frequencies. (a) The world's first terahertz-range photonic crystal waveguide reported in the literature, which operated at ~1 THz, showing curved slab boundary that served as input coupling for a free-space beam, reproduced with permission from C. M. Yee and M. S. Sherwin, Appl. Phys. Lett. **94**, 154104 (2009). Copyright 2009 AIP Publishing LLC; (b) physical structure and simulated propagation of a photonic crystal waveguide, both with and without bends; and (c) the band diagram structure of the photonic crystal waveguide in (b), where the fundamental guided mode is shown in red, the first higher-order mode is in blue, and the bounds of the photonic bandgap are black, from Ref. 153. It is also noted that this plot is transposed with respect to the convention shown in Fig. 10, as we are unable to substantially alter previously images taken directly from previously published work in order to suit our current plotting convention.

silicon dielectric rod waveguides that pre-date it[190,197] required physical support, and so they are not technically substrateless. This early photonic crystal waveguide study did not report propagation loss, and it is noted that an accurate reading of propagating loss would have been very challenging given that terahertz waves were coupled to the guide by focusing a free-space beam to the slab edge, rendering repeatable alignment challenging, and generating non-negligible reflections at the high index-step at the edge. However, a guide of a similar sort with 200 μm-thick silicon was later reported to exhibit 0.04 dB/cm propagation loss at 330 GHz, and less than 0.1 dB/cm from 326 to 331 GHz.[153] The structure of this latter photonic crystal waveguide can be seen in Fig. 11(b), together with an illustration of the hollow-waveguide interface that supplies terahertz waves. It can be seen that the tapered-spike coupler is essentially identical to those which were introduced in Sec. IV B 1, for dielectric rod waveguides. The adaptation of this efficient near-field interface to photonic crystal waveguides offered sufficient precision to characterize the propagation loss of the guide due to repeatable alignment and low reflection. Additional to facilitating hollow-waveguide coupling, the tapered spike has also been exploited to couple to terahertz polymer fibers,[176] as the strong field delocalization that occurs at the narrow tip is closely correlated with the loosely confined, wide-area mode of the fiber. This structure can also serve as antenna,[234] in much the same manner as described in Secs. IV B 1–IV C, or even as a feed antenna for a high-gain dish.[235] Aside from tapers, other far-field interfaces that have been integrated with photonic crystal waveguides in the 300 GHz-band include grating couplers[236,237] and matched dielectric resonator antennas.[238] Finally, contactless evanescent coupling can be exploited for board-to-board connectors between separate photonic crystal waveguide devices, and thereby opening the door to modular systems.[239]

A band diagram for the 300 GHz-band photonic crystal waveguide reported in Ref. 153 is given in Fig. 11(c), showing that the fundamental mode begins to propagate at ~310 GHz, and becomes leaky at ~340 GHz, for a ~9% relative bandwidth. The band diagram also reveals another important detail: highly pronounced curvature, which indicates strong dispersion that can negatively impact performance and degrade signal integrity. For this reason, subsequent work on photonic crystal waveguides has sought to alleviate this dispersion by means of dispersion engineering mediated by optimization of the lattice and track width,[240] and by suppression of the Bragg mirror effects associated with the periodic modulation of waveguide track width.[241] However, both of these studies were solely concerned straight guides, and so it is not clear whether necessary routing structures such as bends may be incorporated into these refined photonic crystal waveguides. In contrast, the prior study in Ref. 153 included 60° bends, which can be seen in Fig. 11(b), and are an essential fundamental component for routing terahertz waves. This facilitated terahertz-wave transmission through a folded 50-cm length of guide with 28 bends. However, the bandwidth of these bend structures was strictly limited, and, in general, it is challenging to implement bend structures in defect-row-based photonic crystal waveguides.

Aside from defect rows, there are other viable approaches to construct a line defect-based waveguide within a photonic crystal medium. We may make use of a photonic crystal that exhibits broken inversion symmetry, and hence the unit cell has a clearly defined "up" and "down." If this structure is mirrored and placed into direct

27 October 2023 05:17:16

© Author(s) 2023

contact with its mirror-image as shown in Fig. 12(a), the interface between the two forms another kind of line defect that may be employed for single-mode terahertz-range waveguiding,[75,242–245] as can be seen in the photonic band diagram shown in Fig. 12(b). This manner of waveguide is called a "valley photonic crystal," which is a class of "photonic topological insulator," and it guides electromagnetic waves at the boundary between two impenetrable photonic crystal media. This particular configuration is known as a "zigzag interface" in which the edge of the large triangle is in proximity to the symmetry plane, but if the points of the triangles were interleaved then a "bearded interface" would be realized,[246] yielding a different edge state with a distinct band structure. In contrast to the above-discussed conventional photonic crystal waveguides, this interface-guided structure does not have a finite waveguide core volume, which is a unique property among dielectric waveguides, in general. Thus, although the propagating mode is bound to the line defect at the interface, the guided waves must necessarily exist in the surrounding photonic crystal medium at adjacent sides, as can be observed in Figs. 12(b) and 12(c). This may seem counter-intuitive, and so it merits mention that the existence of a photonic bandgap does not mean that terahertz waves are not permitted in the photonic crystal medium *at all*, but rather, that *wave propagation* is not permitted, and so the guided waves cannot propagate away from the line defect.

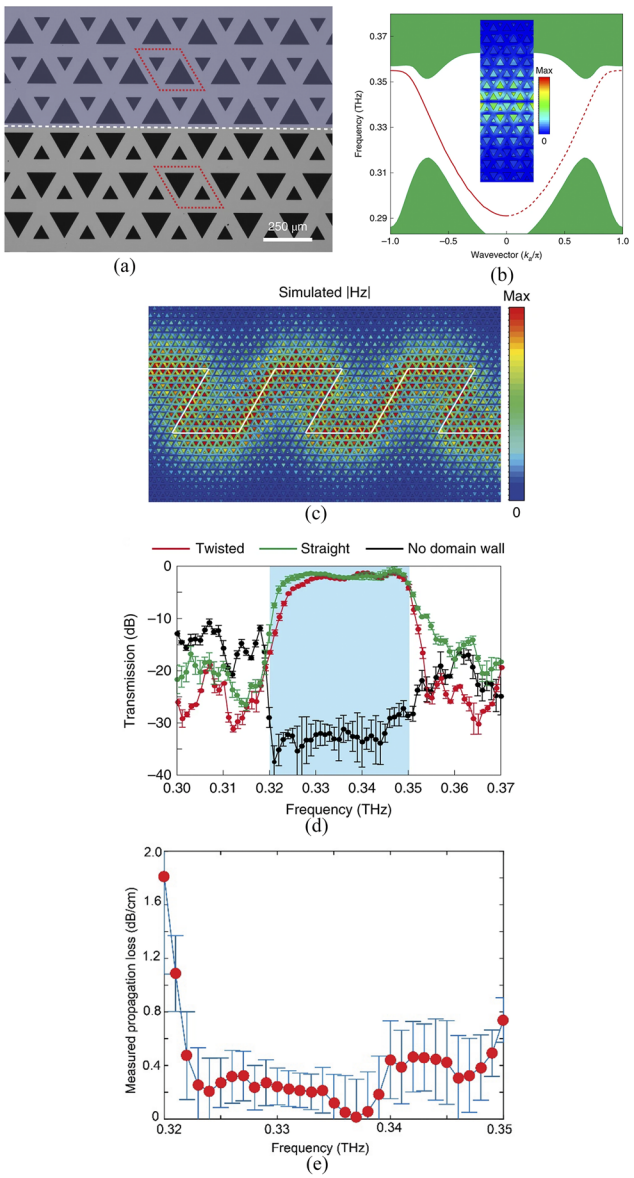

FIG. 12. Terahertz-range valley photonic crystal waveguides, showing (a) the mirror-symmetry of the periodic structure, reflected in the plane of the line defect; (b) the associated photonic band diagram, where the propagating mode is shown in red, and the regions in which propagating modes exist in the photonic crystal are colored in green; (c) a simulation of wave propagation in a guided-wave structure with ten bends; (d) measured transmission through the ten-bend structure, an equivalent straight waveguide, and a photonic crystal sample that lacks a line-defect; and (e) measured propagation loss. All of these materials are from Ref. 75.

The valley photonic crystal waveguide has one very interesting property; unlike conventional photonic crystal waveguides, it is essentially immune to bending loss. This property was tested in Ref. 75 with a structure with ten bends, shown in Figs. 12(c) and 12(d), and it can be seen that the loss contributed by the bends is essentially negligible away from band-edges. On the other hand, the absence of a waveguide core presents a drawback: modal fields are not well-localized within a core, and so it is challenging to directly launch the propagating mode of a given valley photonic crystal device. This is generally addressed with a mode converter, which is essentially a short length of conventional defect-row photonic crystal waveguide after the spike coupler that acts as a transition, and introduces minor additional coupling loss. Another issue is that, because the modal fields of the null-core guide are wholly within the cladding lattice structure, terahertz waves will be strongly affected by disorder and in that lattice. This may be a contributing factor to the vulnerability of photonic topological insulators to back-scattering from structural defects that can arise from non-ideal fabrication, as reported in Ref. 247, although it is noted that this study employed a slow-light waveguide, and was carried out at nano-scale, where fabrication is generally less reliable, and so it is not entirely clear whether the conclusions thereof directly apply here. Furthermore, that article was published in the same year of writing, which indicates that the precise nature of propagation loss in photonic topological insulators remains an open questions. The propagation loss of the terahertz valley photonic crystal is given in Fig. 12(e), and it can be seen that it is low in the vicinity of 337 GHz, but for the majority of the operation bandwidth, it is in the range from 0.2 to 0.5 dB/cm. This renders the valley photonic crystal's propagation loss comparable to the frame-tethered guides discussed in Sec. V—and with markedly reduced, ~10% relative bandwidth, as in the case of the conventional photonic crystal waveguides discussed above. Thus, although valley photonic crystal are an effective solution to the issue of bending loss in photonic crystal waveguides, they do not address all limitations and also present certain additional issues of their own.

VII. EFFECTIVE MEDIUM TECHNIQUES

Section VI C showed that, while photonic crystal medium is a very effective and low-loss means to provide robust support to the

27 October 2023 05:17:16

© Author(s) 2023

waveguide core in an all-silicon structure, the fact that confinement depends upon a photonic bandgap limits operation bandwidth to ~10%. It would be beneficial to devise an all-silicon cladding lattice structure that can maintain the ~40% bandwidth of the dielectric rod waveguides that are presented in Sec. IV, i.e., by using total internal reflection-based confinement *in lieu* of a bandgap. In this Section, we will explore an alternative form of periodic lattice, namely, effective medium, which is capable of tailoring a desired effective index across a broad range of values between that of intrinsic silicon and free-space. Fortunately, the associated theory is markedly more straightforward and intuitive than that of photonic crystals, and this simplicity translates to enhanced freedom in the design of terahertz-range devices, as the functionality and behavior of the lattice structure may be conceptualized more readily.

A. A brief introduction to effective medium theory

An example of a commonly used effective medium structure is given in Fig. 13(a). Similar to the photonic crystals shown in Figs. 11(c) and 11(g), it is an equilateral triangular lattice of cylindrical through-holes that is wholly parameterized by hole pitch, a, and hole diameter, d. However, the lattice constant of an effective medium is significantly smaller than a guided wavelength within the medium, λ_g, and this critical distinction leads to markedly different electromagnetic behavior. While a photonic crystal relies on the collective action of an array of scatterers in order to produce a photonic bandgap, an effective medium simply mixes the two media together, and the resultant composite structure is experienced by a terahertz wave as a (fictional) third medium with an intermediate effective refractive index that is mediated by the geometry of the lattice. Crucially, the lattice geometry may be tailored, offering freedom to engineer a given desired effective index.

It is possible to analyze an effective medium using a photonic band diagram, as in the example given in Fig. 10, where the subwavelength requirement simply translates to small values of Bloch wavevector, corresponding to small phase change across the span of a single period of the lattice. In this region, the fundamental band appears as a diagonal straight line with no curvature whatsoever, as shown. However, the level of detail afforded by a full band diagram is simply not required to model an effective medium, as the subwavelength approximation allows us to compute an effective index based solely upon the volume fraction of the constituent media, which is expressed as a filling factor, ξ. In the case of the lattice that is illustrated in Fig. 13(a), this is found by taking the ratio of a semicircle's area to that of an equilateral triangle

$$\xi = \frac{\pi}{2\sqrt{3}} \cdot \left(\frac{d}{a}\right)^2. \tag{28}$$

This may be employed to compute a bulk effective index using the Maxwell–Garnett approximation, which is dependent upon the orientation of the holes[248]

$$n^2_{\text{bulk},\perp} = \varepsilon_{\text{bulk},\perp} = \varepsilon_{\text{Si}} \cdot \frac{(\varepsilon_{\text{air}} + \varepsilon_{\text{Si}}) + (\varepsilon_{\text{air}} - \varepsilon_{\text{Si}})\xi}{(\varepsilon_{\text{air}} + \varepsilon_{\text{Si}}) - (\varepsilon_{\text{air}} - \varepsilon_{\text{Si}})\xi}, \tag{29}$$

$$n^2_{\text{bulk},\parallel} = \varepsilon_{\text{bulk},\parallel} = \varepsilon_{\text{Si}} + (\varepsilon_{\text{air}} - \varepsilon_{\text{Si}})\xi. \tag{30}$$

The label "$\parallel$" indicates that the electric field vector is oriented in parallel to the axis along which the cylindrical through-holes are aligned, and conversely, "$\perp$" identifies the orthogonal field component. It is also noted that the absolute scale of the lattice (i.e., a) does not play a role in the analysis of bulk effective index nor does the actual frequency of operation. This great simplicity is providence of the effective-medium approximation; once a structure is firmly in the realm of "electrically small," i.e., $a \ll \lambda$, it no longer really matters exactly *how small*—our sole concern is the volume fraction of the constituent materials. Incidentally, this also renders the effective medium somewhat robust against minor deviations, imperfections, and defects in the lattice structure, as their impact upon this volume fraction is minimal.[249]

Finally, we may substitute the values of bulk index given in Eqs. (29) and (30) for the core index, n_{core}, which appears in Eq. (12), in order to obtain a dispersion relation for the perforated slab. Solving the TE dispersion relation in this way yields the results given in Fig. 13(b), where it can be seen that the effective modal index of the perforated slab medium is mediated by the hole size. The achievable range of effective index under variation of filling factor is diminished for lower frequencies due to the dispersion effects associated with dielectric slab waveguides. This may be understood intuitively as the delocalized modal fields interacting more with the surrounding air, which is not dependent upon the hole geometry, and less with the perforated slab itself.

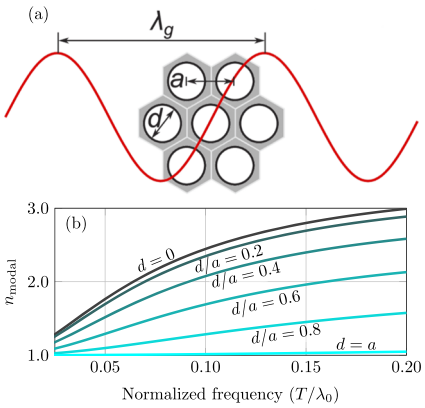

FIG. 13. Effective medium theory, showing (a) an illustration of the geometry of an equilateral lattice of cylindrical through-holes, as well as the requirements of the effective medium theory approximation, i.e., the lattice period a must be significantly smaller than a guided wavelength λ_g, from Ref. 74; and (b) the computed effective modal index of a TE slab mode within a lattice of through-holes that is perforated through a finite-thickness slab.

B. Channel waveguides enabled by effective medium

Surrounding a solid silicon core with a lower-index effective-medium lattice realizes an efficient waveguide with ~40% single-mode bandwidth,[74] as shown in Figs. 14(a)–14(c). This performance is equivalent to that of the wholly unclad dielectric rod waveguides discussed in Sec. IV, while at the same time incorporating a supporting frame for convenient handling. Unlike the frame-tethers in Sec. V, the effective medium causes no progressive loss, which is why the overall propagation loss per-centimeter shown in Fig. 14(c) is equivalent to that of a single tether shown in Figs. 8(e) and 8(f).[203] Furthermore, as the confinement mechanism is total

27 October 2023 05:17:16

© Author(s) 2023

internal reflection, we avoid the bandwidth limitations and strong dispersion imposed by bandgap-based confinement, which were the primary disadvantages of the photonic crystal waveguides presented in Sec. VI. The effective medium-clad guide is capable of supporting both TE and TM polarizations, whereas photonic crystal guides will most often only support TE. On the other hand, effective medium tends to be a less physically robust cladding material than photonic crystal, as there is a preference for a low effective index in order to maximize contrast with the core, leading to a highly porous medium.

Effective medium-cladding was initially demonstrated with straight waveguides,[74] and has since proven compatible with routing structures, such as bends[154] and planar crossings.[251] The latter cited work shows that the geometry of the effective-medium lattice offers an additional degree of design freedom, as hole-size in the vicinity of the crossing was engineered in order to tailor the propagating mode's behavior for reduced crosstalk. On the other hand, the cladding lattice presents certain restrictions upon viable geometries, as the morphology of viable guide-core dimensions and curvature are essentially pixelated by the lattice, either a hole is filled or it is not. Efforts have been made to compensate for this limitation by means of progressive distortion in the vicinity of a bend structure, such that a specific desired filling factor can be maintained, as shown in Fig. 14(d).[154] However, this was implemented with circular-bend geometry, and so it may not translate especially naturally to other curves such as spirals[203] and adiabatic bends.[252] Additional to that, the lattice distortion makes bend-internal features finer, leading to potential issues in fabrication, and makes bend-external holes larger, which may push the limits of the effective-medium approximation. It is significantly more straightforward to simply strip-back the lattice geometry in the vicinity of bends and other routing structures, leaving regular lattices for support where required, and allowing designers to concern themselves solely with the contours of the solid silicon core, as shown in Fig. 14(e). This approach opens the door to "unclad microphotonics"; a general approach for constructing all-silicon substrateless photonic circuits with unclad waveguides that are housed within a solid protective frame and are clad with effective medium over short lengths wherever physical structural support is required.[76] In terms of performance, both the effective-medium clad and unclad microphotonics are essentially equivalent, with the sole trade-off being that unclad microphotonics offers greater convenience of routing at the cost of reduced physical robustness. Both approaches were initially introduced in the frequency band from 260 to 400 GHz, using 200 μm-thick silicon, but have since been proven to operate as high as high as 1.1 THz, and remain self-supporting, if the slab thickness is reduced to 80 μm.[155]

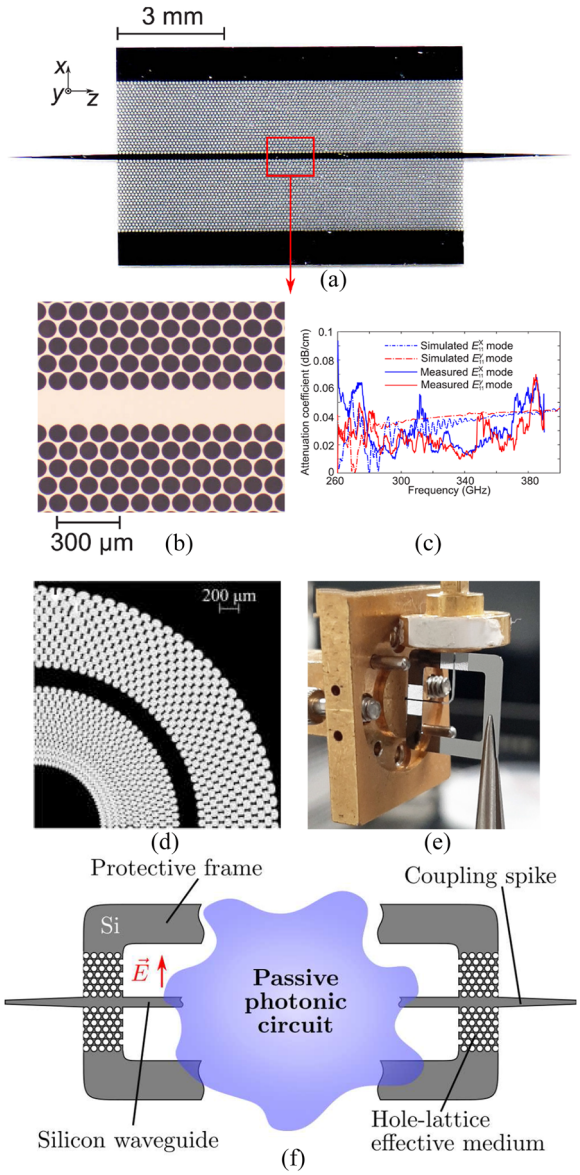

FIG. 14. Channel waveguides enabled by effective-medium cladding that is implemented using a through-hole lattice, showing (a) a straight waveguide, together with (b) a micrograph that shows the detail surrounding the core, and (c) characterization of propagation loss, from Ref. 74; (d) a micrograph of an effective medium-clad bend structure that requires lattice distortion in the vicinity of the bend, from Ref. 154; (e) a photograph of an unclad microphotonic bend structure, which is held by the frame using ordinary tweezers during characterization, from Ref. 250; and (f) an illustration of the concept of unclad microphotonics, in which a passive photonic circuit composed of unclad guides is surrounded by a protective frame, and is structurally supported using effective medium, from Ref. 76.

C. Integrated quasi-optics

While Sec. VII B above has considered effective medium solely as cladding, here we will explore the possibilities availed by propagation within the effective medium itself, i.e., as a slab waveguide, with engineerable index mediated by lattice geometry. In such an arrangement, there is no reason in particular to restrict ourselves to a uniform lattice, but rather, hole radius may vary with respect to position, thereby attaining a gradient-index (GRIN) structure capable of manipulating, redirecting, and steering the flow of guided waves, for integrated optics.[253] It is also noted that this manner of GRIN beam-steering device can be made extremely broadband as it is founded upon the principle of optical ray-tracing, which is frequency-independent.

27 October 2023 05:17:16

© Author(s) 2023

The first use of GRIN media in substrateless integrated all-silicon photonics was to construct wide-aperture lens antennas for photonic crystal waveguide devices.[73,254] In both cases, an end-fire antenna offering ~20 dB gain was obtained, and in Ref. 73, seven distinct ports shared a single Luneburg lens, for a multi-beam antenna with a 120° field of view, shown in Fig. 15. The operation bandwidth of these antennas was limited by the choice of photonic crystal waveguide feed as they were published in 2018—before the advent of effective medium-clad guides in 2019. It is noted that effective medium-clad waveguides are also entirely compatible with integrated lens-based antennas,[255] offering broader bandwidth and the potential for dual-polarization operation. Aside from beamforming, a GRIN medium can also serve as a progressive index transition from the high-index silicon to the low-index surrounding space in order to suppress reflections at the radiation surface of the slab-edge.[73,255,256] On the other hand, the choice of the slab's edge as the radiator surface leads us to the primary limitation of antennas of this sort; a slab-edge can only have appreciable aperture size in *a single dimension* that is parallel to the plane of the slab, and so strong diffraction occurs in the out-of-plane dimension, causing a fan-beam. This effect fundamentally limits achievable gain for GRIN-slab antennas of this sort, as truly high-gain antennas must exhibit large aperture in both dimensions.

Antennas are not the sole viable usage for integrated GRIN optics. If the terahertz waves are maintained within the silicon slab, without interfacing to free-space, it is possible to launch a collimated wavefront directly into a silicon slab waveguide of the sort that is described in Secs. IV A 1 and IV A 2. Thus, terahertz waves are confined to a slab-mode in the out-of-plane dimension, but within the plane of the slab, they behave as an unconfined beam. This paradigm allows us to mimic classical free-space optics setup in a wholly integrated format, in which a slab-guide medium replaces free-space, and the lenses that capture and direct terahertz radiation are fabricated together and in perfect alignment. The concept of terahertz slab-mode beams was first demonstrated using a photonic crystal feed integrated together with a half-Maxwell fisheye lens,[258] but it was found that strong reflections from the photonic crystal adjacent to the feed-point led to trapped radiation within the slab, ultimately causing interference that degraded signal quality. This was later addressed by replacing the photonic crystal medium, with an effective medium-clad dielectric slot waveguide, as shown in Fig. 16(a). This achieves broadband matching to the lens while strongly localizing guided waves at the feed-point, for a well-defined focal spot that is suited to this manner of GRIN lens.[257] The motivation behind the invention of this slab-mode beam platform is related to certain points that were raised in the Introduction: a large portion of the most impressive demonstrations of terahertz-range technology have taken place upon an optics table, using bulky, manually aligned lenses, which is simply untenable in real-world applications. On the other hand, slab-mode beam devices allow us to mimic such classical optics setups in an integrated, mass-producible, hand-held format. One such example is an integrated liquid sensor that was adapted from the well-known classical method of optically probing liquids known as attenuated total reflection, as shown in Figs. 16(b) and 16(c).[257] This technique depends upon oblique reflections that make it possible to separate the forward- and backward-traveling waves, and for this reason, it cannot be realized using ordinary channel waveguides.

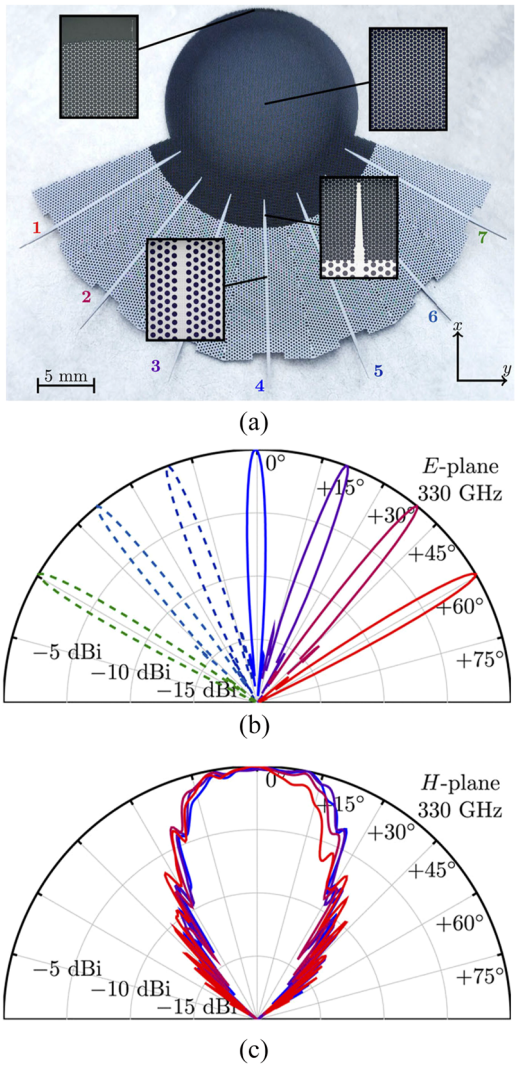

FIG. 15. The first Luneburg lens for the terahertz range, showing (a) physical structure, in which seven distinct photonic crystal waveguide feeds simultaneously interface with a single GRIN lens and [(b) and (c)] measured radiation patterns, showing multi-beam operation in the E-plane, and broader beamwidth in the H-plane, from Ref. 73.

VIII. FUNCTIONAL PASSIVE DEVICES FOR TERAHERTZ-DOMAIN PROCESSING

At this point, we will shift the focus of our discussion away from the various guided-wave structures that are amenable to substrateless all-silicon micro-scale photonics, and move toward passive devices that may be integrated directly into the platform. Thus, this section is not dedicated to the structure and performance of a single waveguiding platform, but rather, it draws from all of them. The

27 October 2023 05:17:16

© Author(s) 2023

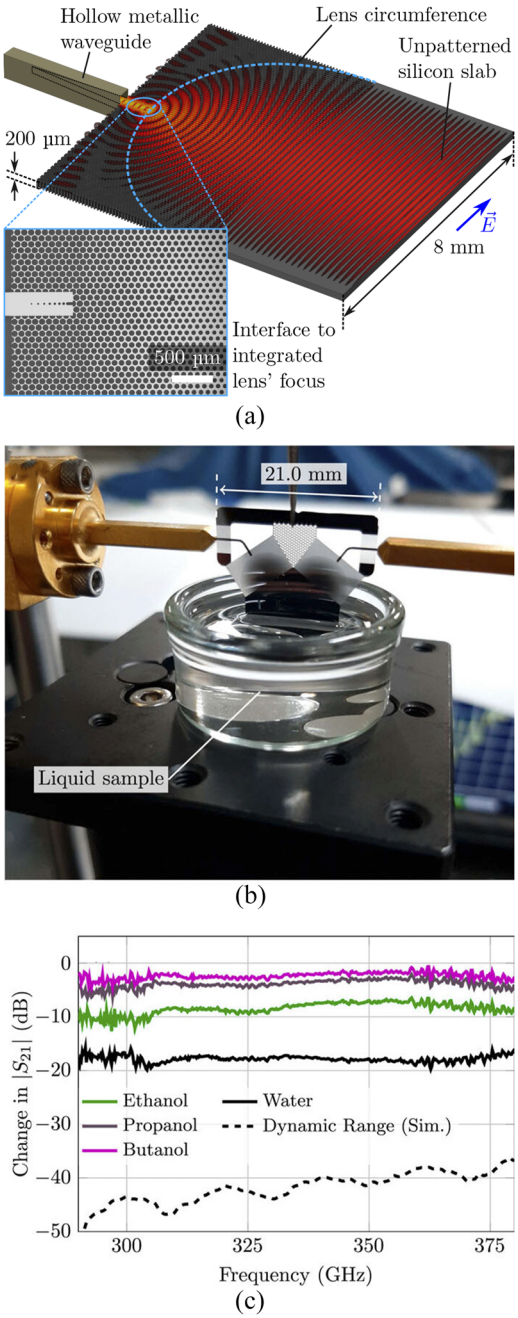

FIG. 16. Miniaturization and integration of classical terahertz optical setups using slab-mode beams, showing (a) an illustration of an integrated half-Maxwell fisheye lens, with inset micrograph of the feed structure; and [(b) and (c)] an attenuated total reflection-based liquid sensor device enabled by the fact that oblique reflections are supported in a slab-guide, from Ref. 257.

operation of these devices can be viewed as a form of signals processing, albeit directly in the terahertz frequency range. This sort of signals processing is markedly more basic and limited than digital and even analog signals processing, which incidentally cannot operate at such high frequencies. Thus, we must instead rely on the physical interaction of guided waves with certain engineered irregularities in the guide geometry, in a manner that is closely related to the broad discipline of microwave engineering[124] albeit with dielectric structures instead of metal.

The ability to incorporate functional devices is a decisive factor in the viability of a given microstructure as a platform for terahertz waves. This is because, taken in isolation, a waveguide is just a pipe that cannot do anything other than convey electromagnetic waves from one point to another. The real strength of waveguides is their capacity to interconnect different functional components in order to form a *terahertz circuit*. In other words, without the devices described in this section, a waveguide is just a waveguide—not a platform.

A. Filters, resonators, sensors, and switches

A cavity resonator is a volume defined by reflective walls that surround it on all sides. Terahertz waves may be confined within this structure provided the internal field pattern, or mode of resonance, which is constructively reinforced by reflections from these walls. Whether or not this condition is met depends upon the size of a wavelength relative to the cavity, and hence it is a frequency-dependent effect. At least one of these walls must be only partially reflective in order to allow coupling into the cavity, and due to reciprocity, any pathway inwards is also a way out. In other words, the capacity to excite a given mode of resonance is directly related to progressive leakage of the trapped energy within said mode of resonance. For this reason, there is no such thing as a "perfect resonator" that can confine energy indefinitely without leakage, as this would make it impossible to couple energy *into* the cavity in order to excite the mode of resonance; it would not resonate, and thus cannot be called a resonator. A true resonator is therefore able to trap energy, but only partially. The degree to which energy is trapped is related to the amount of power that is admitted by the partially reflecting walls; strong rejection will confine radiation more strongly, leading to more-stringent frequency selectivity and slower decay of the trapped power, but also renders coupling into the resonator more challenging.

The dielectric mirror-like properties of photonic crystal make it ideal for the reflective boundaries of a dielectric cavity resonator, and the cavity volume enclosed thereby is defined by simply removing a small cluster of holes to realize a point defect in the lattice. The realization of a resonant cavity of this sort was incidentally the primary motivation behind the development of the first substrate-less all-silicon integrated waveguide,[72] which initiated the line of inquiry to which this tutorial is dedicated. In that work, the cavity is placed between two truncated sections of waveguide, and the mode of resonance was excited by non-propagating evanescent waves that extend through two periods of the photonic bandgap medium, as shown in Fig. 17(a). In this way, the resonator interrupts the guide in series. Only at the frequencies at which strong resonance occurs can energy remain in the cavity for long enough to allow progressive leakage to accumulate appreciable power at the other side of the defect, leading to the stringent frequency selectivity that can be seen in Fig. 17(b). The quality-factor may also be enhanced further by means of optimized lateral offset to the point defect in order to fine-tune the evanescent interaction with guided waves.[261,262] Aside

27 October 2023 05:17:16

© Author(s) 2023

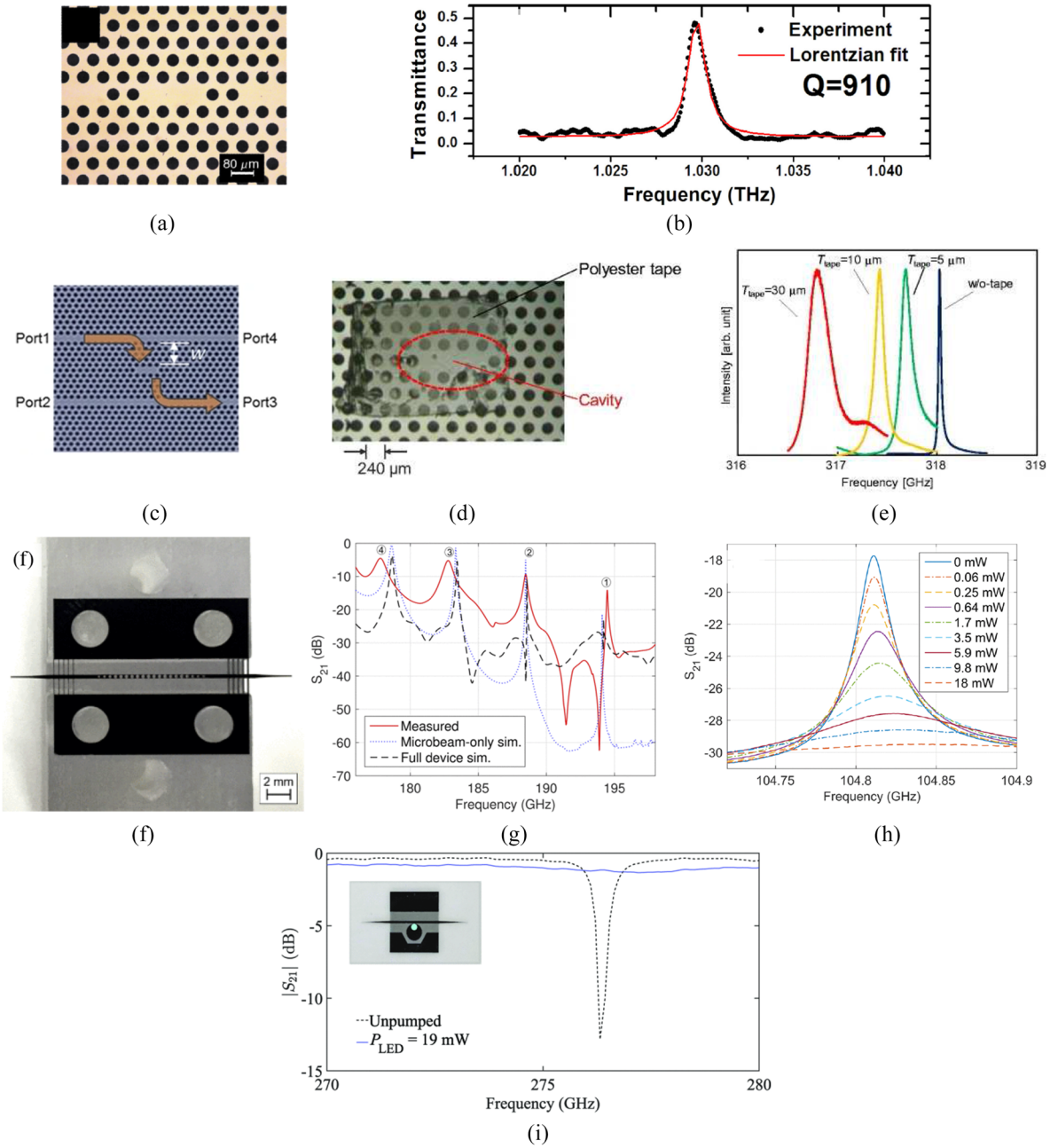

FIG. 17. Resonator structures and their applications, showing (a) and (b) a series-fed photonic crystal resonator operating at ~1 THz, reproduced with permission from C. M. Yee and M. S. Sherwin, Appl. Phys. Lett. **94**, 154104 (2009). Copyright 2009 AIP Publishing LLC; [(c)–(e)] a parallel-fed photonic crystal resonator-based sensor device at ~300 GHz, from Ref. 259; [(f) and (g)] a defected Bragg mirror-based resonator implemented in a frame-tethered waveguide structure at ~200 GHz; (h) a demonstration of photo-switchability of resonance in a closely related resonator at ~100 GHz, where the legend denotes optical illumination power, reproduced with permission from Hanham *et al.*, IEEE Trans. Terahertz Sci. Technol. **7**, 199–208 (2017). Copyright 2017 Author(s), licensed under a Creative Commons Attribution 4.0 License; and (i) a photo-switchable terahertz micro-disk resonator at ~300 GHz implemented with an effective medium-clad waveguide, from Ref. 260.

from series-feeding, it is also possible to realize shunt-configuration by placing the cavity adjacent to the photonic crystal waveguide, and interfacing with the evanescent fields that extend laterally away from the guide core, and this has been demonstrated at ~300 GHz, as shown in Fig. 17(c).[259] The pathway taken by terahertz waves at the resonance frequency is indicated in the diagram, but this configuration also allows for dual operation; frequencies that are unable to resonate within the shunted cavity simply remain

27 October 2023 05:17:16

© Author(s) 2023

in the original waveguide for a notch-filter response from ports 1 to 4.

It is possible to implement photonic crystal cavities in other classes of substrateless all-silicon terahertz waveguide. For instance, if a periodic series of irregularities is introduced into a broadband channel waveguide, this creates a Bragg mirror, which can also be thought of as a one-dimensional photonic crystal. This effect has been exploited in order to realize a terahertz-range bandstop filter in an effective medium-clad waveguide structure, by means of periodic modulation of the waveguide core width,[249] offering strong in-band rejection and steep roll-off at ~300 GHz. Aside from bandstop filters, it is also possible to use this manner of one-dimensional photonic crystal medium to define the partially reflective boundaries of a linear resonant cavity. This has been implemented using arrays of through-holes in frame-tethered guides,[203,204] as shown in Fig. 17(f), for a device operating at ~200 GHz, and subsequently in effective medium-clad guides.[260]

In terms of applications, the strong frequency-selectivity of cavity resonators can be of great assistance when locking to coherent active devices, such as oscillators and mixers,[175,177] as it offers a stable reference for the local oscillator. Unshielded dielectric cavity resonators are also natural sensors, as the mode of resonance will incorporate evanescent fields that extend into the air-filled surrounding space, but are unable to propagate away. For this reason, the empty space occupied by these evanescent fields must also be considered part of the volume of the resonant cavity. Thus, bringing an analyte or sample close to the resonator will detuning or dampen the resonant response. In this way, liquid sensors capable of detecting very small, nanoliter volumes have been implemented using an offset series-fed photonic crystal resonator, by passing a narrow polymer pipe through a hole adjacent to the point-defect.[262] A related demonstration showed that a shunt-feed photonic crystal cavity is capable of detecting a thin piece of polymer tape placed directly onto the cavity,[259] as shown in Figs. 17(d) and 17(e). This manner of resonant polymer-tape sensor demonstration was later adapted to valley photonic crystals,[263] which employed a ring resonator[264,265] instead of a linear cavity. Incidentally, a ring resonator does not make use of reflections to trap energy, but rather, it bends a linear section of waveguide track around upon itself in order to form a closed loop, and resonance occurs at frequencies for which a round-trip around the ring track is in-phase with the original wave. As in the case of cavity resonators, energy is coupled to the ring by means of evanescent interaction, but in this case, only shunt configuration is viable.

As an aside, we wish to remark that resonator structures are not the sole viable means to realize an integrated all-silicon terahertz sensor device. On the contrary, an unshielded dielectric waveguide can readily interact with a given analyte that is either placed in contact with the core, or in the vicinity of the surrounding evanescent fields, and the properties of the analyte will be reflected in a change in transmission through that waveguide. However, the lack of a resonator decreases the strength of interaction, and so this must be compensated by prolonging the interaction with a longer, straight section of waveguide as sensor. This approach has previously been demonstrated for an unclad microphotonic biosensor,[266] i.e., by functionalizing the silicon core's surface with streptavidin molecules that immobilize antibodies. A related demonstration utilized a dielectric rod waveguide to probe the contents of a sealed microfluidic liquid channel,[267] with no physical contact between the guide and the liquid.

Returning to integrated resonators, it is noted that resonance may only be sustained in low-loss materials, such as intrinsic silicon, as a lossy material would rapidly absorb the confined radiation. Thus, if it were possible to modulate material loss, this would avail us of switchable resonators. The photoelectric effect may be exploited to this end. When visible light is incident upon silicon, a portion of the energy absorbed by this semiconductor excites free carriers, thereby raising the conductivity of the material.[268] This phenomenon may also be thought of as photo-induced doping. Thus, a sufficiently intense visible light source shone upon a given all-silicon terahertz resonator can switch its resonance off. This was initially demonstrated using the waveguide-tethered structure described above,[204] as shown in Fig. 17(h), and then with effective medium-clad disk resonators,[260] as shown in Fig. 17(i), and valley photonic crystal ring resonators.[269]

B. Frequency-domain channelization

As stated in the Introduction, one of the primary motivations for the development of terahertz technology is to exploit the vast, untapped spectrum as RF bandwidth for high-speed wireless communications applications. For practical reasons, it is advisable to divide a given terahertz link's broad bandwidth into a set of contiguous, smaller-bandwidth manageable channels that can be downconverted and processed separately. This is because, if a single wideband channel were utilized, the associated intermediate-frequency (IF) circuitry would also need to accommodate the exact same absolute spectral bandwidth, which translates to far greater relative bandwidth after the link is received and down-converted. For argument's sake, if a link with 80 GHz bandwidth is operating at 400 GHz, then the relative RF bandwidth, i.e., the ratio of bandwidth to carrier frequency, is just 20%. However, if an IF frequency of 50 GHz is employed, the relative bandwidth of the down-converted signal increases in proportion to the ratio of the carrier and IF frequencies to 160%, or 9:1, necessitating advanced, expensive, wideband equipment. On the other hand, if the same RF bandwidth were divided into four to ten equal allocations that are down-converted independently, the downconverted relative bandwidth would be in the range from 15% to 40%, which is much more manageable.

Terahertz-range frequency–domain multiplexing may be performed by applying an optical signal with more than two laser lines to a single optoelectronic source.[178,273,274] In this scheme, at least two optical laser signals are modulated and linearly combined together with an unmodulated, CW laser signal. All of these signals are of different frequencies, and the beat between each modulated signal and the unmodulated signal corresponds to a terahertz-range frequency, which the optoelectronic source extracts via optical rectification to extract the envelope of the overall light-wave signal. However, this has the potential to introduce undesired nonlinear effects, such as inter-modulation distortion and shot noise, which can degrade channel quality.[178] On the other hand, such nonlinear effects can be avoided entirely if we instead make use of a passive multiplexer to divide the terahertz–domain signals directly, as opposed to a nonlinear device. Furthermore, a passive multiplexer can make use of

27 October 2023 05:17:16

© Author(s) 2023

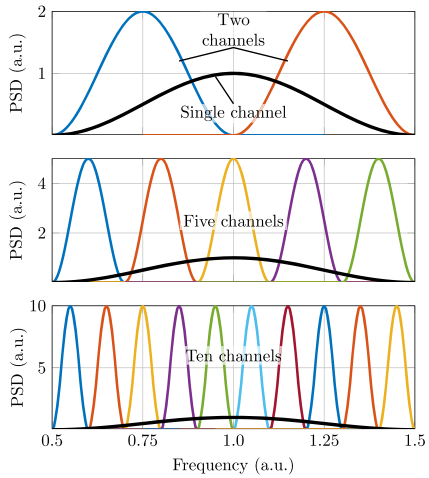

FIG. 18. An abstract illustration of the claim that passive multiplexing of multiple independent sources can increase overall transmit power in a broadband spectrum allocation. The output power of a single source is fixed, but the amount of bandwidth that it occupies is variable. Thus, spreading a single channel across the entire bandwidth reduces the peak power spectral density (PSD) of that channel. Conversely, reducing the channel's bandwidth will concentrate this fixed amount of transmit power within a narrower set of frequencies, thereby increasing the peak power spectral density, and leaving room for more channels, as observed in these plots. This is one of the primary motivations to realize passive frequency–domain multiplexers for the terahertz range.

an independent terahertz source for each individual channel, and in doing so, essentially combine the power from all of those sources. In other words, a larger number of channels leads to a higher amount of total link power, as shown in the abstract scenario given in Fig. 18. Incidentally, the link-budget analysis[29] that is cited in the Introduction makes implicit usage of this manner of multiplexer-based power-combining because it models the link as a contiguous set of 1-GHz channels carrying 10 mW. Thus, when modeling a 76-GHz span in the atmospheric transmission window from 300 to 376 GHz, for instance, this means that *76 individual sources* are combined into a single high-power 760 mW link using a *76-channel passive multiplexer*. Although such a passive multiplexer does not yet exist in the terahertz range, there have been several noteworthy efforts of related devices implemented with all-silicon microstructures, which will be described below. In this context, a device that splits terahertz waves into two channels is termed a "diplexer," three channels is a "triplexer," and any number larger than that is a "multiplexer."

Several dielectric waveguide-based passive terahertz frequency splitters exploit the principle of frequency-dependent delocalization of modal fields, which is observed in Figs. 5(a) and 5(b). According to the analysis presented in Sec. IV A, lower frequencies are weakly confined in an unshielded dielectric waveguide, meaning that a greater proportion of modal fields occupies the surrounding space. A consequence is that, if a given object is placed into the vicinity of the guide, then lower frequencies will tend to interact with that object more strongly than the more-stringently confined high frequencies. This effect can be exploited for frequency-dependent power transfer,[200,239] i.e., by bringing two waveguides into close proximity and allowing them to exchange energy via evanescent interaction. Low frequencies are transferred more readily, but are also coupled back into the originating waveguide quickly, making it possible to tailor the length of the coupled-line section to select a given specific desired wavelength. In the context of substrateless all-silicon terahertz devices, this was pioneered using photonic crystal waveguides,[270,275] as shown in Figs. 19(a) and 19(b), and it can be seen that lower frequencies (i.e., below ~325 GHz) are indeed transferred out of the originating guide with this short-length coupler. This defines a lower-frequency "cross" channel of 6.5 GHz bandwidth, as well as a higher-frequency "bar" channel, which spans 16.7 GHz. Evanescent couplers have also been deployed to realize valley photonic crystal-based frequency-division diplexers,[271] and isolation was enhanced in that work using a shunt-coupled ring resonator of the same sort that was described in Sec. VIII A, as shown in Fig. 19(c). As before, only the lower frequencies (i.e., below ~340 GHz) are able to interact strongly with the ring resonator, as can be seen in Fig. 19(d), thereby allowing a coupled channel to be defined at ~330 GHz. However, the choice of this resonator stringently limits the achievable bandwidth of this coupled path to ~0.6 GHz, in contrast to the ~14-GHz "bar" channel. Another demonstration of a valley photonic crystal-based device exploited the fact that that evanescent couplers in this platform essentially place one mirror-image "edge" in close proximity to another, and if the distance is sufficiently small then the structure approaches the state of having no edge, as there are insufficiently many rows of photonic crystal in-between the edges to sustain the bandgap. This effect is frequency-dependent, and has been exploited to construct an integrated terahertz triplexer[276] that operates from ~300 to ~350 GHz, with individual channels offering 13, 7, and 5 GHz bandwidth.

Evanescent interaction between parallel dielectric channel waveguides can be exploited to transfer terahertz waves across a micro-scale airgap,[200,239] and this translates very naturally to the unclad microphotonics platform that is presented in Sec. VII B, as the exposed, lattice-free sections of waveguide offer the freedom to structure the junction as-needed. This was initially demonstrated at ~300 GHz[76] using a short-length evanescent coupler to transfer low frequencies into a ~45 GHz "cross" channel and maintain the un-transferred high frequencies in a >70 GHz "bar" channel. The span of these channels shows that the broader bandwidth of this class of waveguide, in comparison to photonic crystal techniques, translates to diplexers that are implemented in the platform. It is for this reason that this exact diplexer structure was later repurposed to a hybrid-integrated dual-channel receiver module,[178] and it is also noted that closely related structures have been implemented in effective medium-clad waveguides,[154] albeit as part of a fundamental investigation into cross-talk. On the topic of cross-talk, poor isolation is a disadvantage of this structure. In Ref. 178, for instance, isolation of just 7 dB is reported for the "bar" channel, meaning that the transmission of the desired signal is only ~2.2-times greater than that of the undesired, and this is generally considered insufficient for practical communications applications. Efforts to address this have included utilizing a longer coupled-line section, as shown in Figs. 19(e) and 19(f), for a diplexer operating at ~700 GHz,[272] which exhibited 101 GHz for the "cross" channel and 37 GHz for the "bar." As a result, the lower frequencies are transferred twice across the junction, to form the "bar" channel, and the high-frequency "cross" channel is transferred once. The fact that a full transfer of power

27 October 2023 05:17:16

© Author(s) 2023

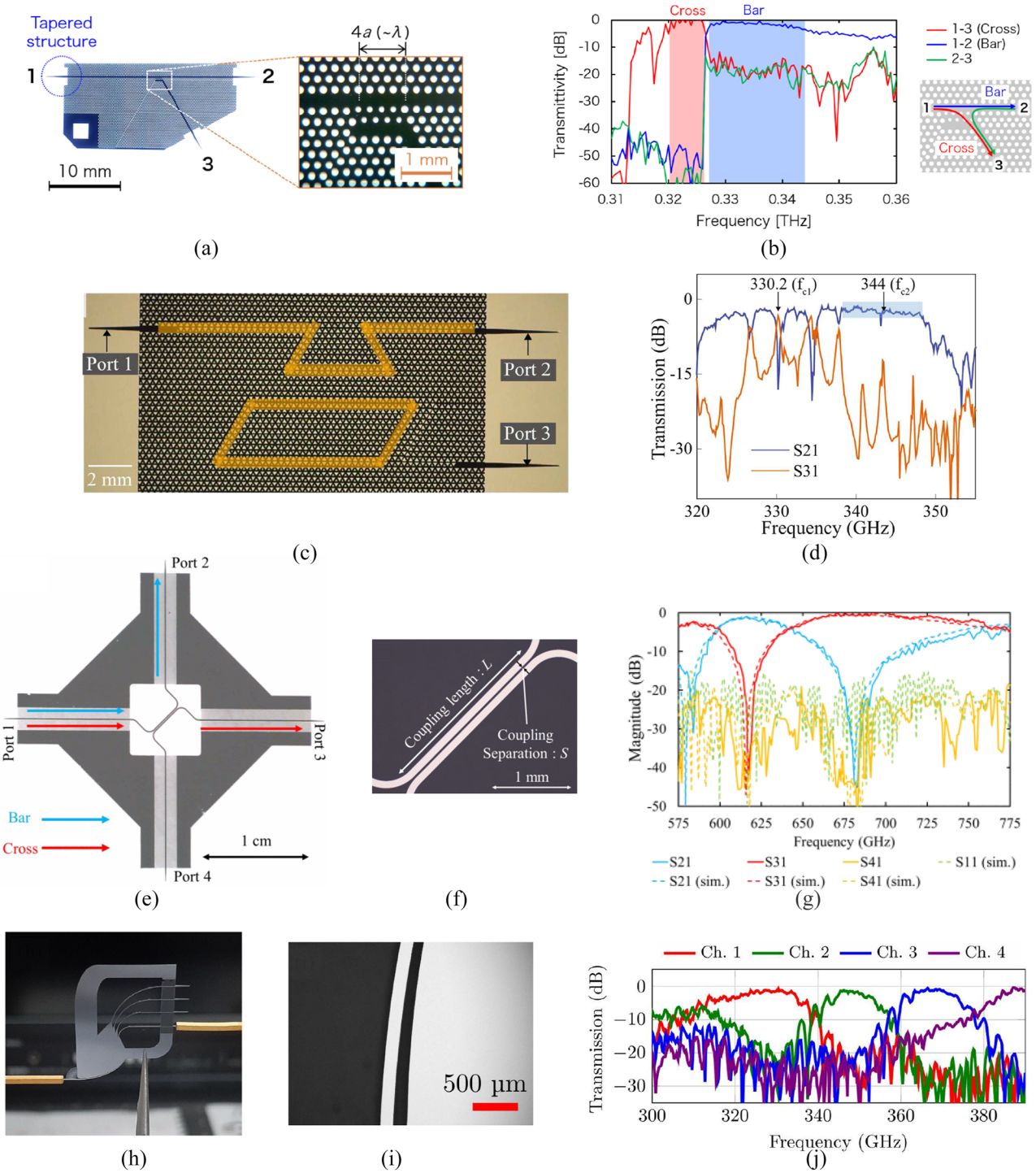

FIG. 19. A selection of integrated passive diplexers and multiplexers, showing [(a) and (b)] an evanescent coupler-based diplexer implemented in a photonic crystal waveguide platform, from Ref. 270; [(c) and (d)] a coupled ring resonator-based diplexer implemented in a valley photonic crystal waveguide, reproduced with permission from Kumar *et al.*, Nat. Commun. **13**, 5404 (2022). Copyright 2022 Author(s), licensed under a Creative Commons Attribution 4.0 License; [(e)–(g)] an evanescent coupler-based diplexer using unclad microphotonics, from Ref. 272; and [(h)–(j)] a gratingless integrated tunneling multiplexer offering four ports, from Ref. 77.

27 October 2023 05:17:16

© Author(s) 2023

from one guide to another has been completed innately engenders strong isolation, as there is simply no power left in the originating guide. This is evidenced by the two strong minima in the frequency response shown in Fig. 19(g), each being at the center of the opposing channel's bandwidth. However, this effect only holds for a single specific frequency, and so the strong ~45-dB maximum isolation is not observed over the entire 3-dB bandwidth of either channel. An alternative approach has integrated all-silicon filters together with the diplexer,[277] and thereby achieved strong cross-talk suppression across the entire bandwidth of each channel.

All of the devices presented in the paragraphs above have, in one way or another, made use of the principle of frequency-selective evanescent interaction between adjacent lengths of channel waveguide. This is the most common approach toward channelization of terahertz waves, but it is not the sole means, as the integrated quasi-optics principles introduced in Sec. VII C have facilitated some interesting and useful specialized devices. For instance, an integrated Bragg-mirror based stopband filter[249] has previously been implemented in a dielectric slab waveguide as an array of effective-medium stripes that intercept a collimated slab-mode beam.[257] If this filter was implemented in a channel waveguide, the reflected power would simply be sent back toward the source, but the use of slab-mode beams allows for oblique incidence, i.e., by orienting the stripes diagonally. Thus, the stopband of the filter is deflected away from the originating waveguide and is collected by an integrated lens. This enables a broadband diplexer operating at ~300 GHz with channels of ~50 and 115 GHz bandwidth, as well as strong isolation. Another example of an integrated quasi-optical device totally eschews lenses of any kind, instead relying on evanescent coupling from a channel waveguide to a slab waveguide, and so power that is coupled thereto from the channel waveguide will propagate away as a slab-mode beam. The geometry of the junction is tailored in order to realize a frequency-scanning focused beam in the slab, which is collected with a series of inverse flares in order to define separate channels. This approach has been utilized to realize a four-channel integrated multiplexer operating a ~350 GHz, with 13–20 GHz per-channel, as shown in Figs. 19(h)–19(j).[77] To our knowledge, this is the highest number of channels ever reported in a terahertz-range passive multiplexer device to-date.

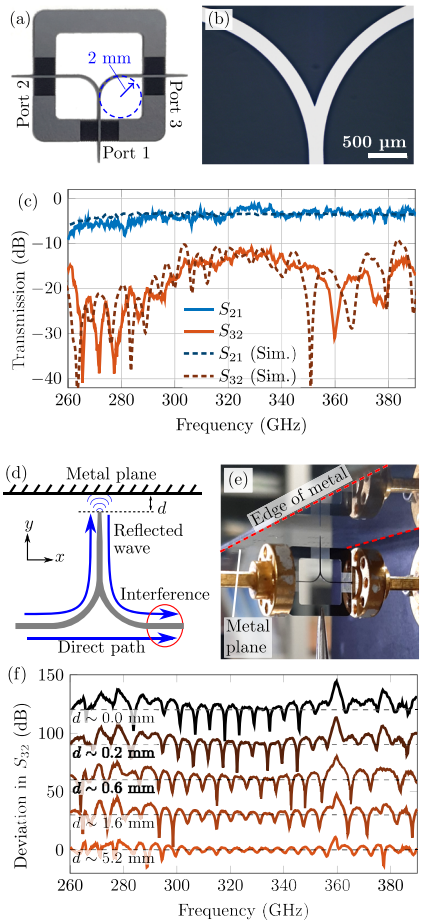

FIG. 20. An integrated Y-junction implemented in an unclad microphotonics platform, showing (a) a photograph of the entire device, (b) a micrograph that shows the details of the junction itself, (c) transmission response, (d) an illustration of the principle of an interferometric sensing experiment that uses the Y-junction as a depth guage, where the port coupler serves as near-field sensor, (e) a photograph of the sensor in deployment, and (f) measured response, where the distance to the plane may be estimated by the free spectral range of the interference fringes. All of these materials are from Ref. 76.

C. Power splitters and combiners; directional couplers

While the devices presented in Sec. VIII B have purposely defined separate paths for different frequency bands, those to which we will dedicate the remainder of this Section aim to split the entire operation bandwidth across two paths. This broadband division of terahertz power within an integrated circuit allows for two copies of a given signal to be propagated independently and input to different components. This finds uses in quadrature modulation communications schemes, as a local oscillator may be distributed to independent I- and Q-modulators concurrently. Another example is for synchronization in order to provide a stable reference to estimate the phase change through a device under test. Power-splitting is also a necessary building block to construct larger components, such as Mach–Zehnder modulators,[278,279] which independently delay the two copies of a signal prior to recombining in order to effect controllable selective destructive interference. This latter example avails us of the second main use of broadband power dividers: due to reciprocity, any structure that can split a signal can also merge independent signals together, and so a Mach–Zehnder modulator will generally make use of two of the same structure, i.e., one to split and one to merge following the delay stage. The latter mode of operation can also be employed to combine power from multiple synchronized sources. Thus, devices of this sort can both split and merge power. There is also a third mode of operation that essentially combines the prior two configurations; a source is attached to one of the branching paths, as in the power-combining mode, and a detector to the other, as in a splitter. This latter configuration is essential for instrumentation systems that are intended to measure reflection, e.g., in vector network analyzers can measured a two-port device's S_{11} as well as S_{21}, as the amount of the source's power that is incident upon the detector depends upon reflection that occurs following the merger

27 October 2023 05:17:16

© Author(s) 2023

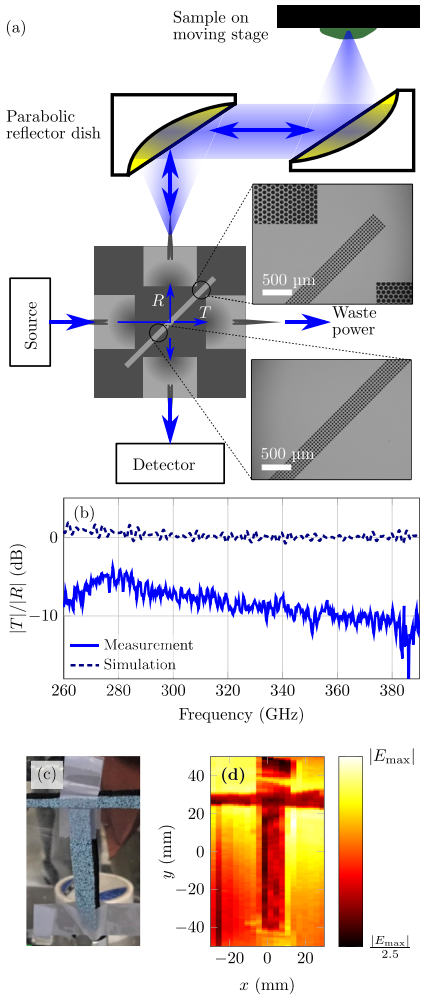

FIG. 21. An integrated quasi-optical beam splitter device, showing, (a) an illustration of the device structure and deployment in an imaging experiment, with inset micrographs, (b) measured and simulated splitting ratio, (c) the simple imaging target employed, composed of absorptive foam taped to a reflective mirror, and (d) the result of the imaging experiment.

of the two paths. This can also be employed for monostatic radar, i.e., in which electromagnetic waves are emitted and received by a single antenna.[280]

The most straightforward form of substrateless all-silicon integrated power splitter is a Y-junction, which is essentially a waveguide track that is progressively widened until it is ultimately forked into two symmetrical paths. This physical structure is visually evocative of the even-division that it is intended to perform, and so students of integrated photonics rarely experience difficulty in understanding its functionality; it appears to split into two even paths it does indeed do just that. Electromagnetically, the widening of the track is necessary to allow higher-order modes to propagate, leading to modes with exhibit maxima that are not situated in the center of the waveguide track. These higher-order maxima ultimately form the individual single-mode paths following splitting. Y-junctions of this exact sort have been implemented in unclad microphotonics,[76] as shown in Figs. 20(a) and 20(b), and were shown to exhibit less than 0.5 dB splitting loss from 280 to 390 GHz, as observed in Fig. 20(c). It is also noted from the results in Fig. 20(c) that the transmission between the two branched paths is non-negligible, and although this is generally undesirable for most applications, it was exploited in the cited work to supply a reference signal in a demonstration of an interferometric near-field depth-guage sensor, as shown in Figs. 20(d)–20(f). The Y-junction structure was later adapted to operation in the vicinity of 1-THz in a thinner wafer,[155] and the same interferometric sensing technique was enhanced with external optics to serve as a 3D-imaging radar.

Aside from Y-junctions, broadband power splitters have also been implemented using free-space optical principles by leveraging what is known as a "half-mirror," which is a diagonally oriented, partially reflective structure that has previously been retrofitted to terahertz time–domain spectroscopy systems in order to allow for simultaneous probing of transmission and reflection of a given sample.[281] When combined with the integrated quasi-optics techniques presented in Sec. VII C, this principle allows for a broadband integrated four-port directional coupler. As shown in Fig. 21(a), a collimated slab-mode beam is impinged obliquely upon a single diagonal stripe of effective-medium, which serves as a partially reflective barrier that is intended to reflect roughly half of incident power toward a 90° angle, and the reflected and transmitted paths are independently collected by separate integrated optics.[282] However, the half-mirror's reflectivity is dependent upon the size of the holes that comprise the effective-medium structure, and in this case, this renders the device quite sensitive to tolerances. From the measurement results shown in Fig. 21(b), it is clear that the reflection is markedly stronger than transmission, and this is ascribed to over-etching of the holes. Thus, further refinement and innovation is required in order to enhance this concept's robustness to tolerance. Despite this asymmetrical response, however, the integrated beam splitter proved sufficient for a simple demonstration of terahertz imaging, as shown in Figs. 21(c) and 21(d).

IX. CONCLUSION

A. Summary and comparison

This tutorial article presents an overview of efforts toward the realization of a suitable general-purpose integration platform for terahertz-wave devices and systems. Section III justified our preference for substrateless dielectric waveguides composed of high-purity intrinsic silicon, Secs. IV–VII present different waveguiding structures that have been developed, and Sec. VIII describes several functional devices that may be directly integrated therewith. We have also presented key aspects of relevant electromagnetic theory, which we hope will be instructive and useful to readers, as well as a number of historical accounts on the development of the current state-of-the-art (see Secs. II and VI A).

In summary, dielectric waveguides for millimeter-wave circuitry had a brief "heyday" as a prospective high-volume communications technology for trunk and backhaul systems prior to the widespread adoption of optical fiber, as discussed in Sec. II. Contemporarily, terahertz-wave technology is envisaged as a viable means to

27 October 2023 05:17:16

© Author(s) 2023

TABLE I. A comparison of the different all-silicon substrateless waveguide structures reported in the literature, which contrasts key salient aspects of suitability as a general-purpose platform for terahertz waves. It is noted that these rankings are subjective, based upon our own appraisal in view of the entire content of this tutorial, and hence the distinction between the individual labels are not based directly upon numerical data.

Guide	Efficiency	Single-mode bandwidth (%)	Dispersion	Bends/routing	Robustness and handling	Compactness
Hollow metallic waveguide	Poor	40	Good	Good	Excellent	Poor
Dielectric rod waveguide	Unreported	40	Good	Poor	Poor	Fair
Frame-tethered guide	Fair	40	Good	Good	Poor	Good
Conventional photonic crystal waveguide	Good	<10	Poor	Poor	Great	Great
Valley photonic crystal	Fair	<10	Fair	Great	Great	Fair
Effective-medium-clad waveguide	Excellent	40	Good	Good	Fair	Good

provide high-volume short-range wireless links, and thereby offer an air access network that is complementary to fiber. Terahertz waves are also envisaged for a broad variety of useful and attractive sensing and spectroscopy applications. The practical real-world uptake of all of these applications of terahertz waves is contingent upon the availability of a general-purpose integration platform, and selection of the appropriate platform is itself a consideration that hinges upon the specific choice of waveguide that serves as interconnect. Hollow metallic waveguides are currently the dominant form of terahertz-range interconnect, but it is our strongly held contention that a substrateless, all-intrinsic-silicon approach has more potential. When testing this contention, it is appropriate to benchmark performance against that of more-mature hollow metallic waveguides; if there is no significant benefit, we will simply be "reinventing the wheel." This is incidentally the same reason why we have omitted silicon-on-glass guides from our review, as Fig. 4 shows the efficiency is comparable to hollow metallic waveguides. The benchmarked comparison of all-silicon guides is summarized in Table I.

Section III showed that the low absorption, low material dispersion, and high refractive index of pure intrinsic silicon is innately suited to produce efficient, compact waveguides. This was shown theoretically using a simple, idealized arrangement in which a beam of silicon is surrounded by free-space on all sides, and Sec. IV explored terahertz-range implementations of such a structure. In reality, however, physical support is always required, and so a dielectric rod waveguide cannot be considered "substrateless" in a strict sense, and the supporting medium may introduce absorption and leakage losses due to the unshielded nature of the guide. Fixed-width airgaps between guides are also precluded, the overall complexity of routing in the circuit is limited, and the guide core itself must be physically handled during assembly, which are all practical drawbacks. Thus, it is clear that a substrateless all-silicon integration platform must have some form of in-plane structural support. As described in Sec. V, the guide may be connected to a supporting frame by means of narrow integrated silicon tethers. However, these structures cause progressive loss due to scattering, leading to performance close to that of hollow metallic waveguides; frame-tethered guides have been reported with 0.45–0.85 dB/cm propagation loss in the range of 500–750 GHz.[203] This partly defeats the primary purpose of an all-dielectric platform, i.e., superior efficiency. The tethers are also innately fragile, as reinforcement would innately engender further loss, making for an unfortunate trade-off between efficiency and stability.

The photonic crystal waveguides discussed in Sec. VI avoid the lossy tethers and instead utilize a supporting hole-lattice structure that leverages a photonic bandgap for in-plane field confinement, and this approach achieved <0.1 dB/cm propagation loss in the range 326–331 GHz.[153] The lattice structure is quite robust and is the only class of substrateless all-silicon waveguide to have been implemented in a silicon wafer of less than 50 μm thickness.[72] However, bends severely restrict the operation bandwidth in conventional photonic crystal waveguides, which limits the routing freedom. Valley photonic crystals address this limitation with sharp, lossless, zero-radius bends that are unique among dielectric waveguides and drastically reduces the footprint area in comparison to gradual (e.g., conventional circular) bends. On the other hand, this compactness advantage is diminished by the large lateral area that the domain-wall-guided, core-less mode occupies, which demands that adjacent tracks must be spaced far apart. This wide-area mode is incidentally also vulnerable to any irregularity in the lattice that it occupies. Aside from these points, the most significant drawback of photonic crystal waveguides is their reduced, ~10% single-mode bandwidth, in contrast to the 40% single-mode bandwidth offered by dielectric rod waveguides, frame-tethered waveguides, and hollow-metallic waveguides like. Not only that, waveguides of this sort generally suffer from strong dispersion, which further reduces usable bandwidth in applications, such as communications. The consequences of this bandwidth-reduction issue merit a moment's consideration. As stated in the Introduction, the great spectral bandwidth offered by terahertz waves is a major motivation for the development of terahertz communications technology, and the bulk of noteworthy demonstrations of terahertz-range communications have taken place below 400 GHz. In view of these two facts, we wish to remark that 10% bandwidth at 400 GHz (i.e., 40 GHz) is the same amount of spectrum as 40% at 100 GHz, where Fig. 4 shows that the efficiency-advantage of dielectric waveguides over metallic waveguides becomes negligible. Thus, moving from millimeter-wave hollow metallic waveguides to terahertz-range photonic crystal waveguides does not actually yield broader bandwidth; we have reinvented the wheel once more. On the other hand, one could argue that the available relative bandwidth is less critical than the management of network resources within each band. Viewed from that perspective, an upward shift, e.g., from 100 to 400 GHz, may be beneficial to

27 October 2023 05:17:16

© Author(s) 2023

ease congestion at lower frequencies, even if there is no increase in absolute bandwidth.

The terahertz-range effective-medium techniques waveguides presented in Sec. VII were developed specifically to address the bandwidth limitation of photonic crystal while maintaining an in-plane supporting frame—all that we need do is simply shrink the supporting hole-lattice. This not only recovers the 40% single-mode bandwidth and achieves propagation loss as low as ~0.05 dB/cm from 260 to 400 GHz[74] but also opens the door to gradient-index integrated optics for wide-aperture antennas and integrated quasi-optical systems. Bends and routing structures are also offered, and the design of such features can be made more convenient by simply stripping back the in-plane effective-medium support prior to curving the guide, yielding the unclad microphotonics platform. On the other hand, these bends are necessarily of gradual curvature and hence occupy greater footprint area than those of valley photonic crystals. Another advantage of photonic crystal is that it tends to exhibit more physical strength than effective medium for more-robust devices.

B. Recommendation for future platform

Our survey of the literature has led us to the conclusion that micro-scale all-silicon effective-medium-clad waveguides are currently the most promising candidate for a general-purpose terahertz integration platform. It is the only reported solution for which the in-plane support does not compromise the intrinsic efficiency of high-resistivity float-zone silicon, while exhibiting 40% single-mode bandwidth on-par with hollow metallic waveguides. In addition to that, the innate compactness, ease-of-routing, and the great variety of useful viable passive functional devices will all be of great benefit to future integrated systems for terahertz waves. That said, alternative waveguiding structures do have some advantages, such as the compact resonators of photonic crystal waveguides and the zero-radius bends offered by valley photonic crystals. Fortunately, none of these waveguiding structures are mutually exclusive, as all are fabricated from the same material, and in the same way. Thus, we can imagine a combined approach that is primarily composed of effective-medium-clad waveguide, but is capable of transitioning to another class whenever relevant specialized functionality is required.

C. Further work

There remain several gaps in the current capabilities that are offered by substrateless all-silicon microstructures, and so further exploration and research effort is required. It would be highly beneficial to interface two separately fabricated all-silicon circuits together without creating a bottleneck, and to this end, compact, broadband and efficient interposer structures between dielectric waveguides are highly desirable. Related to that, it would be particularly attractive and convenient to allow for an out-of-plane, vertical-coupling access mechanism, in order that terahertz waves may be supplied or extracted at positions other than the circuit's edge. Unfortunately, however, initial efforts toward this aim have made use of coupled-line techniques, which ultimately limited the bandwidth,[239] and so fresh new ideas are required for a broadband out-of-plane coupling solution. Other gaps are revealed by perusal of the functional devices that are detailed in Sec. VIII; while the largest number of channels offered by any passive terahertz multiplexer is currently just four,[77] we should ideally have closer to a 100 channels,[29] but there is no clear pathway toward the realization of this aim with a realistically compact form-factor. Section VIII also shows that, among the classes of passive functional devices considered, namely resonators, frequency–domain channelizers, and power splitters, comparatively little research has been dedicated to the latter. Given the key usefulness that this structure offers instrumentation and spectroscopy applications, i.e., the capacity to simultaneously measure the transmission and reflection of a given sample,[281] it would be of great benefit to extend the operation bandwidth to beyond 40%. This would, however, engender operating dielectric waveguides beyond their single-mode bandwidth, and hence special consideration would be required in order to suppress undesired effects associated with higher-order modes, such as the potential for dispersion and interference.

Active devices such as sources, detectors, and mixers of terahertz radiation may be incorporated by means of *hybrid integration*, in which fundamentally heterogeneous integrated circuits based on different semiconductor processes are fabricated separately and then assembled together. In this way, it is possible to combine a III–V semiconductor-based chip that bears a terahertz active device together with a substrateless all-silicon terahertz circuit, and allow them to exchange terahertz waves via direct physical contact. At the lower end of the terahertz range, dielectric waveguides have been backside-coupled to optoelectronic sources at 137 GHz,[174] and connected to surface-mounted bolometers,[173] with the latter achieving broadband operation by utilizing the guide in its multimode region. Aside from dielectric rod waveguides, photonic crystal waveguides have been coupled to surface-mounted Schottky barrier diodes, for a subharmonic mixer operating at ~100 GHz.[177] In that work, the robust in-plane lattice of the photonic crystal is beneficial for physical support, which is a critical concern for this manner of assembly. It is for this reason that, at higher frequencies in the vicinity of ~300 GHz, the majority of demonstrations of hybrid integration have made use of photonic crystal waveguides,[137,138,175,176,178] using a Vivaldi antenna-like coupler as an adiabatic transformation. On the other hand, this choice of guide also limits achievable bandwidth, and to address this, the concept of hybrid integration has been extended to the more-broadband unclad microphotonics platform, with a small chip of the same cross section as the waveguide core is accurately positioned in a corresponding recess in the waveguide's cladding.[179] In this arrangement, the chip's substrate essentially behaves as a short length of dielectric waveguide, and hence allows terahertz waves across the full operation bandwidth to pass naturally between the chip substrate and the guide core. As a result, this hybrid-integration junction can support the entire 40% single-mode relative bandwidth offered by unclad microphotonics. That said, the cited work is only a proof-of-concept study for this technology, and so there are many challenges that must be addressed in order to extend it into a full terahertz-range hybrid-integrated chipset.

We offer one final thought for your consideration. From the perspective of communications, the ultimate aim of terahertz-range engineering is to produce an air interface that is worthy of optical fiber. Does it not stand to reason that we should base it upon the self-same optical waveguide principles?

27 October 2023 05:17:16

© Author(s) 2023

ACKNOWLEDGMENTS

Daniel Headland acknowledges support from the CONEX-Plus programme funded by Universidad Carlos III de Madrid and the European Union's Horizon 2020 Research and Innovation Programme under Marie Sklodowska-Curie Grant Agreement No. 801538. This work was supported by Australian Research Council Discovery Project Nos. DP180103561 and DP220100489. G. Carpintero acknowledges the Research Executive Agency (REA) Grant Agreement No. 862788 (TERAmeasure project) under Horizon 2020 Excellent Science, Fostering Novel Ideas FET-open program. This work was supported in part by Japan Science and Technology Agency through the Core Research for Evolutional Science and Technology (CREST; Program No. JPMJCR21C4), in part, by the National Institute of Information and Communications Technology (NICT), Japan (Grant No. 03001), and by KAKENHI, Japan (Grant No. 20H00249). The authors would also like to thank Mr. Tomoki Sagisaka for performing the imaging experiment that is detailed in Fig. 21.

AUTHOR DECLARATIONS

Conflict of Interest

The authors have no conflicts to disclose.

Author Contributions

Daniel Headland: Conceptualization (equal); Funding acquisition (equal); Software (lead); Visualization (lead); Writing – original draft (lead); Writing – review & editing (equal). **Masayuki Fujita**: Funding acquisition (equal); Supervision (supporting); Writing – original draft (supporting); Writing – review & editing (equal). **Guillermo Carpintero**: Funding acquisition (equal); Supervision (supporting); Writing – original draft (supporting); Writing – review & editing (equal). **Tadao Nagatsuma**: Funding acquisition (equal); Supervision (supporting); Writing – original draft (supporting); Writing – review & editing (equal). **Withawat Withayachumnankul**: Conceptualization (equal); Funding acquisition (equal); Supervision (lead); Writing – review & editing (equal).

DATA AVAILABILITY

The data that support the findings of this study are available from the corresponding author upon reasonable request.

REFERENCES

[1] Cisco, "Global mobile data traffic forecast update, 2018–2023," (2019).
[2] I. Orsolic and L. Skorin-Kapov, "A framework for in-network QoE monitoring of encrypted video streaming," IEEE Access **8**, 74691–74706 (2020).
[3] Q.-V. Pham and W.-J. Hwang, "Network utility maximization-based congestion control over wireless networks: A survey and potential directives," IEEE Commun. Surv. Tutorials **19**, 1173–1200 (2017).
[4] C. E. Shannon, "Communication in the presence of noise," Proc. IRE **37**, 10–21 (1949).
[5] M. J. Marcus, "Progress in opening access to spectrum above 100 GHz," IEEE Wireless Commun. **26**, 2–3 (2019).
[6] M. Polese, J. M. Jornet, T. Melodia, and M. Zorzi, "Toward end-to-end, full-stack 6G terahertz networks," IEEE Commun. Mag. **58**, 48–54 (2020).
[7] A. A. Gargari, M. Pagin, M. Polese, and M. Zorzi, "6G integrated access and backhaul networks with sub-terahertz links," in *Proceedings of the On-Demand Network Systems and Services Conference* (IEEE, 2023), pp. 13–19.
[8] A. A. Raja, M. A. Jamshed, H. Pervaiz, and S. A. Hassan, "Performance analysis of UAV-assisted backhaul solutions in THz enabled hybrid heterogeneous network," in *Proceedings of the Conference on Computer Communications Workshops* (IEEE, 2020), pp. 628–633.
[9] T. Kleine-Ostmann and T. Nagatsuma, "A review on terahertz communications research," J. Infrared, Millimeter, Terahertz Waves **32**, 143–171 (2011).
[10] H.-J. Song and T. Nagatsuma, "Present and future of terahertz communications," IEEE Trans. Terahertz Sci. Technol. **1**, 256–263 (2011).
[11] T. Nagatsuma and G. Carpintero, "Recent progress and future prospect of photonics-enabled terahertz communications research," IEICE Trans. Electron. **E98.C**, 1060–1070 (2015).
[12] J. Federici and L. Moeller, "Review of terahertz and subterahertz wireless communications," J. Appl. Phys. **107**, 111101 (2010).
[13] H.-J. Song and N. Lee, "Terahertz communications: Challenges in the next decade," IEEE Trans. Terahertz Sci. Technol. **12**, 105–117 (2022).
[14] H.-J. Song, K. Ajito, A. Wakatsuki, Y. Muramoto, N. Kukutsu, Y. Kado, and T. Nagatsuma, "Terahertz wireless communication link at 300 GHz," in *Proceedings of the International Topical Meeting on Microwave Photonics* (IEEE, 2010), pp. 42–45.
[15] X. Yu, S. Jia, H. Hu, M. Galili, T. Morioka, P. U. Jepsen, and L. K. Oxenløwe, "160 Gbit/s photonics wireless transmission in the 300-500 GHz band," APL Photonics **1**, 081301 (2016).
[16] S. Jia, G. Jacobsen, M. Galili, T. Morioka, D. Zibar, L. K. Oxenlowe, X. Pang, O. Ozolins, X. Yu, H. Hu, J. Yu, P. Guan, F. Da Ros, and S. Popov, "0.4 THz photonic-wireless link with 106 Gb/s single channel bitrate," J. Lightwave Technol. **36**, 610–616 (2018).
[17] S. Jia, M.-C. Lo, L. Zhang, O. Ozolins, A. Udalcovs, D. Kong, X. Pang, R. Guzman, X. Yu, S. Xiao, S. Popov, J. Chen, G. Carpintero, T. Morioka, H. Hu, and L. K. Oxenløwe, "Integrated dual-laser photonic chip for high-purity carrier generation enabling ultrafast terahertz wireless communications," Nat. Commun. **13**, 1388 (2022).
[18] T. Nagatsuma, K. Oogimoto, Y. Yasuda, Y. Fujita, Y. Inubushi, S. Hisatake, A. M. Agoues, and G. C. Lopez, "300-GHz-band wireless transmission at 50 Gbit/s over 100 meters," in *Proceedings of the International Conference on Infrared, Millimeter, and Terahertz Waves* (IEEE, 2016).
[19] C. Castro, R. Elschner, T. Merkle, C. Schubert, and R. Freund, "Experimental demonstrations of high-capacity THz-wireless transmission systems for beyond 5G," IEEE Commun. Mag. **58**, 41–47 (2020).
[20] T. Harter, C. Füllner, J. N. Kemal, S. Ummethala, J. L. Steinmann, M. Brosi, J. L. Hesler, E. Bründermann, A.-S. Müller, W. Freude, S. Randel, and C. Koos, "Generalized Kramers–Kronig receiver for coherent terahertz communications," Nat. Photonics **14**, 601–606 (2020).
[21] Y. Horst, T. Blatter, L. Kulmer, B. I. Bitachon, B. Baeuerle, M. Destraz, W. Heni, S. Koepfli, P. Habegger, M. Eppenberger, E. De Leo, C. Hoessbacher, D. L. Elder, S. R. Hammond, L. E. Johnson, L. R. Dalton, Y. Fedoryshyn, Y. Salamin, M. Burla, and J. Leuthold, "Transparent optical-THz-optical link at 240/192 Gbit/s over 5/115 m enabled by plasmonics," J. Lightwave Technol. **40**, 1690–1697 (2022).
[22] P. Rodríguez-Vázquez, J. Grzyb, B. Heinemann, and U. R. Pfeiffer, "A 16-QAM 100-Gb/s 1-m wireless link with an EVM of 17% at 230 GHz in an SiGe technology," IEEE Microwave Wireless Compon. Lett. **29**, 297–299 (2019).
[23] L. Moeller, J. Federici, and K. Su, "THz wireless communications: 2.5 Gb/s error-free transmission at 625 GHz using a narrow-bandwidth 1 mW THz source," in *Proceedings of the General Assembly and Scientific Symposium* (URSI, 2011).
[24] K. Ishigaki, M. Shiraishi, S. Suzuki, M. Asada, N. Nishiyama, and S. Arai, "Direct intensity modulation and wireless data transmission characteristics of terahertz-oscillating resonant tunnelling diodes," Electron. Lett. **48**, 582–583 (2012).
[25] N. Oshima, K. Hashimoto, S. Suzuki, and M. Asada, "Terahertz wireless data transmission with frequency and polarization division multiplexing using resonant-tunneling-diode oscillators," IEEE Trans. Terahertz Sci. Technol. **7**, 593–598 (2017).

27 October 2023 05:17:16

© Author(s) 2023

[26]Y. Uemura, Y. Kawamoto, N. Shibata, L. Yi, and T. Nagatsuma, "600-GHz-band heterodyne receiver system using photonic techniques," in *Proceedings of the International Topical Meeting on Microwave Photonics* (IEEE, 2020), pp. 256–259.
[27]A. Kanno, "Advanced photonics technology for 1-THz wireless communication," in *Proceedings of the Opto-Electronics and Communications Conference and Photonics Global Conference* (IEEE, 2017).
[28]P. Sen and J. M. Jornet, "Experimental demonstration of ultra-broadband wireless communications at true terahertz frequencies," in *Proceedings of the International Workshop on Signal Processing Advances in Wireless Communications* (IEEE, 2019).
[29]T. Schneider, A. Wiatrek, S. Preussler, M. Grigat, and R.-P. Braun, "Link budget analysis for terahertz fixed wireless links," IEEE Trans. Terahertz Sci. Technol. **2**, 250–256 (2012).
[30]C. M. Armstrong, "The truth about terahertz," IEEE Spectrum **49**, 36–41 (2012).
[31]P. Haggerty, "Integrated electronics—A perspective," Proc. IEEE **52**, 1400–1405 (1964).
[32]T. L. Koch and U. Koren, "Semiconductor photonic integrated circuits," IEEE J. Quantum Electron. **27**, 641–653 (1991).
[33]J. Ma, L. Moeller, and J. F. Federici, "Experimental comparison of terahertz and infrared signaling in controlled atmospheric turbulence," J. Infrared, Millimeter, Terahertz Waves **36**, 130–143 (2015).
[34]A. Moreira, R. Valadas, and A. de Oliveira Duarte, "Performance of infrared transmission systems under ambient light interference," IEE Proc.: Optoelectron. **143**, 339–346 (1996).
[35]K. Wong and T. O'Farrell, "Spread spectrum techniques for indoor wireless IR communications," IEEE Wireless Commun. **10**, 54–63 (2003).
[36]T. Koonen, F. Gomez-Agis, F. Huijskens, K. A. Mekonnen, Z. Cao, and E. Tangdiongga, "High-capacity optical wireless communication using two-dimensional IR beam steering," J. Lightwave Technol. **36**, 4486–4493 (2018).
[37]C. Li, X. Zhang, E. Tangdiongga, X. Dai, C.-T. Tsai, H.-Y. Wang, Y. Xiang, G.-R. Lin, Z. Cao, and T. Koonen, "Cost-efficient half-duplex 10 Gbit/s all-optical indoor optical wireless communication enabled by a low-cost Fabry–Perot laser/photodetector," Opt. Lett. **44**, 1158–1161 (2019).
[38]C. E. Wamsley, J. Hoopman, and J. M. Kenkel, "Safety guidelines concerning the use of protective eyewear and gauze during laser procedures," Aesthetic Surg. J. **41**, 1179–1185 (2021).
[39]J. Strong, "Interferometry for the far infrared," J. Opt. Soc. Am. **47**, 354–357 (1957).
[40]T. Phillips, G. Neugebauer, M. Werner, and P. Huggins, "Detection of submillimeter 870-micron CO emission from the Orion molecular cloud," Astrophys. J. **217**, L161–L164 (1977).
[41]P. Jewell, J. Hollis, F. Lovas, and L. Snyder, "Millimeter- and submillimeter-wave surveys of Orion A emission lines in the ranges 200.7–202.3, 203.7–205.3, and 330–360 GHz," Astrophys. J., Suppl. Ser. **70**, 833–864 (1989).
[42]G. Stacey, N. Geis, R. Genzel, J. Lugten, A. Poglitsch, A. Sternberg, and C. Townes, "The 158 micron forbidden C II line - A measure of global star formation activity in galaxies," Astrophys. J. **373**, 423–444 (1991).
[43]D. P. Woody, *An Observation of the Submillimeter Cosmic Background Spectrum* (University of California, Berkeley, 1975).
[44]D. Muehlner, "Spectrum and isotropy of the submillimeter background radiation," in *Infrared and Submillimeter Astronomy* (Springer, 1977), pp. 143–152.
[45]C. Yu, S. Fan, Y. Sun, and E. Pickwell-MacPherson, "The potential of terahertz imaging for cancer diagnosis: A review of investigations to date," Quant. Imaging Med. Surg. **2**, 33 (2012).
[46]M. Naftaly, N. Vieweg, and A. Deninger, "Industrial applications of terahertz sensing: State of play," Sensors **19**, 4203 (2019).
[47]S. Busch, M. Weidenbach, M. Fey, F. Schäfer, T. Probst, and M. Koch, "Optical properties of 3D printable plastics in the THz regime and their application for 3D printed THz optics," J. Infrared, Millimeter, Terahertz Waves **35**, 993–997 (2014).
[48]P. Nikitin, "A review of non-polar liquids as materials for bulk acousto-optic devices operating with terahertz radiation," J. Phys.: Conf. Ser. **1421**, 012032 (2019).
[49]I. Prozheev, O. Smolyanskaya, M. Duka, A. Ezerskaya, V. Orlov, E. Strepitov, N. Balbekin, and M. Khodzitsky, "Study of penetration depth dispersion of THz radiation in human pathological tissues," Prog. Electromag. Res. **1537**, 1536–1539 (2014).
[50]A. Dobroiu, R. Wakasugi, Y. Shirakawa, S. Suzuki, and M. Asada, "Absolute and precise terahertz-wave radar based on an amplitude-modulated resonant-tunneling-diode oscillator," Photonics **5**, 52 (2018).
[51]H. Matsumoto, I. Watanabe, A. Kasamatsu, and Y. Monnai, "Integrated terahertz radar based on leaky-wave coherence tomography," Nat. Electron. **3**, 122–129 (2020).
[52]L. Yi, R. Kaname, R. Mizuno, Y. Li, M. Fujita, H. Ito, and T. Nagatsuma, "Ultra-wideband frequency modulated continuous wave photonic radar system for three-dimensional terahertz synthetic aperture radar imaging," J. Lightwave Technol. **40**, 6719–6728 (2022).
[53]R. Woodward, B. Cole, V. Wallace, D. D. Arnone, R. Pye, E. Linfield, M. Pepper, and A. Davies, "Terahertz pulse imaging of in-vitro basal cell carcinoma samples," in *Proceedings of the Conference on Lasers and Electro-Optics* (IEEE, 2001), pp. 329–330.
[54]C. S. Joseph, R. Patel, V. A. Neel, R. H. Giles, and A. N. Yaroslavsky, "Imaging of *exvivo* nonmelanoma skin cancers in the optical and terahertz spectral regions Optical and Terahertz skin cancers imaging," J. Biophot. **7**, 295–303 (2014).
[55]D. D. Arnone, C. M. Ciesla, A. Corchia, S. Egusa, M. Pepper, J. M. Chamberlain, C. Bezant, E. H. Linfield, R. Clothier, and N. Khammo, "Applications of terahertz (THz) technology to medical imaging," Proc. SPIE **3828**, 209–219 (1999).
[56]B. Karagoz, H. Altan, and K. Kamburoglu, "Terahertz pulsed imaging study of dental caries," in *European Conference on Biomedical Optics* (Optica Publishing Group, 2015), p. 95420N.
[57]M. Herrmann, M. Tani, K. Sakai, and R. Fukasawa, "Terahertz imaging of silicon wafers," J. Appl. Phys. **91**, 1247–1250 (2002).
[58]T. Yang, Y. Li, R. Stantchev, Y. Zhu, Y. Qin, X. Zhou, and W. Huang, "Detection of defects on the surface of a semiconductor by terahertz surface plasmon polaritons," Appl. Opt. **55**, 4139–4144 (2016).
[59]S. Prabhu, S. Ralph, M. Melloch, and E. Harmon, "Carrier dynamics of low-temperature-grown GaAs observed via THz spectroscopy," Appl. Phys. Lett. **70**, 2419–2421 (1997).
[60]K. Su, Y.-C. Shen, and J. A. Zeitler, "Terahertz sensor for non-contact thickness and quality measurement of automobile paints of varying complexity," IEEE Trans. Terahertz Sci. Technol. **4**, 432–439 (2014).
[61]F. Ellrich, M. Bauer, N. Schreiner, A. Keil, T. Pfeiffer, J. Klier, S. Weber, J. Jonuscheit, F. Friederich, and D. Molter, "Terahertz quality inspection for automotive and aviation industries," J. Infrared, Millimeter, Terahertz Waves **41**, 470–489 (2020).
[62]N. Vieweg, F. Rettich, A. Deninger, H. Roehle, R. Dietz, T. Göbel, and M. Schell, "Terahertz-time domain spectrometer with 90 dB peak dynamic range," J. Infrared, Millimeter, Terahertz Waves **35**, 823–832 (2014).
[63]M. Ibrahim, D. Headland, W. Withayachumnankul, and C. Wang, "Nondestructive testing of defects in polymer–matrix composite materials for marine applications using terahertz waves," J. Nondestr. Eval. **40**, 37 (2021).
[64]M. Komatsu, M. Mizuno, S. Saito, K. Fukunaga, and Y. Ohki, "Terahertz spectral change associated with glass transition of poly-ε-caprolactone," J. Appl. Phys. **117**, 133102 (2015).
[65]H. Lin, Y. Dong, D. Markl, B. M. Williams, Y. Zheng, Y. Shen, and J. A. Zeitler, "Measurement of the intertablet coating uniformity of a pharmaceutical pan coating process with combined terahertz and optical coherence tomography in-line sensing," J. Pharm. Sci. **106**, 1075–1084 (2017).
[66]Z. Wang, Y. Peng, C. Shi, L. Wang, X. Chen, W. Wu, X. Wu, Y. Zhu, J. Zhang, G. Cheng, and S. Zhuang, "Qualitative and quantitative recognition of chiral drugs based on terahertz spectroscopy," Analyst **146**, 3888–3898 (2021).
[67]J.-H. Son, "Principle and applications of terahertz molecular imaging," Nanotechnology **24**, 214001 (2013).
[68]J. F. Federici, B. Schulkin, F. Huang, D. Gary, R. Barat, F. Oliveira, and D. Zimdars, "THz imaging and sensing for security applications—Explosives, weapons and drugs," Semicond. Sci. Technol. **20**, S266 (2005).
[69]A. Luukanen, R. Appleby, M. Kemp, and N. Salmon, "Millimeter-wave and terahertz imaging in security applications," in *Terahertz Spectroscopy and Imaging* (Springer, 2012), pp. 491–520.

27 October 2023 05:17:16

© Author(s) 2023

[70]K. Kawase, Y. Ogawa, Y. Watanabe, and H. Inoue, "Non-destructive terahertz imaging of illicit drugs using spectral fingerprints," Opt. Express **11**, 2549–2554 (2003).
[71]M. Leahy-Hoppa, M. Fitch, X. Zheng, L. Hayden, and R. Osiander, "Wideband terahertz spectroscopy of explosives," Chem. Phys. Lett. **434**, 227–230 (2007).
[72]C. M. Yee and M. S. Sherwin, "High-Q terahertz microcavities in silicon photonic crystal slabs," Appl. Phys. Lett. **94**, 154104 (2009).
[73]D. Headland, W. Withayachumnankul, R. Yamada, M. Fujita, and T. Nagatsuma, "Terahertz multi-beam antenna using photonic crystal waveguide and Luneburg lens," APL Photonics **3**, 126105 (2018).
[74]W. Gao, X. Yu, M. Fujita, T. Nagatsuma, C. Fumeaux, and W. Withayachumnankul, "Effective-medium-cladded dielectric waveguides for terahertz waves," Opt. Express **27**, 38721–38734 (2019).
[75]Y. Yang, Y. Yamagami, X. Yu, P. Pitchappa, J. Webber, B. Zhang, M. Fujita, T. Nagatsuma, and R. Singh, "Terahertz topological photonics for on-chip communication," Nat. Photonics **14**, 446–451 (2020).
[76]D. Headland, W. Withayachumnankul, X. Yu, M. Fujita, and T. Nagatsuma, "Unclad microphotonics for terahertz waveguides and systems," J. Lightwave Technol. **38**, 6853–6862 (2020).
[77]D. Headland, W. Withayachumnankul, M. Fujita, and T. Nagatsuma, "Gratingless integrated tunneling multiplexer for terahertz waves," Optica **8**, 621–629 (2021).
[78]A. Rivera-Lavado, M. Ali, D. Gallego-Cabo, L.-E. García-Muñoz, D. V. Lioubtchenko, and G. Carpintero, "Contactless RF probe interconnect technology enabling broadband testing to the terahertz range," IEEE Trans. Terahertz Sci. Technol. **13**, 34–43 (2023).
[79]C. Yeh, F. Shimabukuro, P. Stanton, V. Jamnejad, W. Imbriale, and F. Manshadi, "Communication at millimetre–submillimetre wavelengths using a ceramic ribbon," Nature **404**, 584–588 (2000).
[80]C. Yeh, F. Shimabukuro, and P. H. Siegel, "Low-loss terahertz ribbon waveguides," Appl. Opt. **44**, 5937–5946 (2005).
[81]R. M. Knox, "Dielectric waveguide microwave integrated circuits - An overview," IEEE Trans. Microwave Theory Tech. **24**, 806–814 (1976).
[82]B. J. Puttnam, R. S. Luis, G. Rademacher, Y. Awaji, and H. Furukawa, "1 Pb/s transmission in a 125μm diameter 4-core MCF," in *Proceedings of the Conference on Lasers and Electro-Optics* (Optica Publishing Group, 2022).
[83]G. Rademacher, R. S. Luís, B. J. Puttnam, N. K. Fontaine, M. Mazur, H. Chen, R. Ryf, D. T. Neilson, D. Dahl, J. Carpenter, P. Sillard, F. Achten, M. Bigot, J. Sakaguchi, and H. Furukawa, "1.53 Peta-bit/s C-band transmission in a 55-mode fiber," in *Proceedings of the European Conference on Optical Communication* (IEEE, 2022).
[84]R. Thomas, R. J. Rapp, M. A. Spalding, R. K. Stix, M. E. Kordahi, and N. S. Bergano, "Technology in undersea cable systems: 50 years of progress," Mar. Technol. Soc. J. **49**, 88–109 (2015).
[85]Z. S. Bischof, R. Fontugne, and F. E. Bustamante, "Untangling the world-wide mesh of undersea cables," in *Proceedings of the ACM Workshop on Hot Topics in Networks* (Association for Computing Machinery, 2018), pp. 78–84.
[86]J. Ballato and P. Dragic, "Glass: The carrier of light - A brief history of optical fiber," Int. J. Appl. Glass Sci. **7**, 413–422 (2016).
[87]H. Schnitger and H.-G. Unger, "Circular waveguide system for trunk communications," IEEE Trans. Commun. **22**, 1374–1377 (1974).
[88]W. Menzel, "50 years of millimeter-waves: A journey of development," Microwave J. **51**, 28 (2008); available at https://www.microwavejournal.com/articles/6708-50-years-of-millimeter-waves-a-journey-of-development
[89]T. Yoneyama and S. Nishida, "Nonradiative dielectric waveguide for millimeter-wave integrated circuits," IEEE Trans. Microwave Theory Tech. **29**, 1188–1192 (1981).
[90]S. Shindo and T. Itanami, "Low-loss rectangular dielectric image line for millimeter-wave integrated circuits," IEEE Trans. Microwave Theory Tech. **26**, 747–751 (1978).
[91]M. M. Chrepta and H. Jacobs, "Self-oscillating mixers in dielectric waveguide," Technical Report No. ADA044128, Army Electronics Command Fort, Monmouth, NJ, 1977.
[92]H. Jacobs and M. M. Chrepta, "Electronic phase shifter for millimeter-wave semiconductor dielectric integrated circuits," IEEE Trans. Microwave Theory Tech. **22**, 411–417 (1974).
[93]P. Toulios, "Image line millimeter integrated circuits directional coupler design," in National Electronics Conference, 1970.
[94]W. V. McLevige, T. Itoh, and R. Mittra, "New waveguide structures for millimeter-wave and optical integrated circuits," IEEE Trans. Microwave Theory Tech. **23**, 788–794 (1975).
[95]K. Solbach, "Electric probe measurements on dielectric image lines in the frequency range of 26-90 GHz," IEEE Trans. Microwave Theory Tech. **26**, 755–758 (1978).
[96]F. Kuroki, H. Ohta, and T. Yoneyama, "Transmission characteristics of NRD guide as a transmission medium in THz frequency band," in *Proceedings of the Joint International Conference on Infrared and Millimeter Waves and the International Conference on Terahertz Electronics* (IEEE, 2005), Vol. 2, pp. 331–332.
[97]R. Knox, P. Toulios, and J. Howell, "Radiation losses in curved dielectric image waveguides of rectangular cross section," in *Proceedings of the International Microwave Symposium* (IEEE, 1973), pp. 25–27.
[98]Y. Shiau, "Dielectric rod antennas for millimeter-wave integrated circuits (short papers)," IEEE Trans. Microwave Theory Tech. **24**, 869–872 (1976).
[99]A. Kaurs, "A tunable bandpass ring filter for rectangular dielectric waveguide integrated circuits (short papers)," IEEE Trans. Microwave Theory Tech. **24**, 875–876 (1976).
[100]J. Paul and Y.-W. Chang, "Millimeter-wave image-guide integrated passive devices," IEEE Trans. Microwave Theory Tech. **26**, 751–754 (1978).
[101]T. Hisatsugu, S. Yamamura, S. Yokogawa, Y. Hirachi, A. Miura, and A. Shibatomi, "A 160mW 65GHz Gunn diode," in *Proceedings of the International Electron Devices Meeting* (IEEE, 1976), pp. 94–97.
[102]M. Chrepta and H. Jacobs, "Millimeter wave integrated circuits," in *Proceedings of the International Microwave Symposium* (IEEE, 1974), p. 198.
[103]T. Itoh and F.-J. Hsu, "Distributed Bragg reflector Gunn oscillators for dielectric millimeter-wave integrated circuits," IEEE Trans. Microwave Theory Tech. **27**, 514–518 (1979).
[104]M. Lazarus, E. Bullimore, and S. Novak, "A sensitive millimeter wave self-oscillating Gunn diode mixer," Proc. IEEE **59**, 812–814 (1971).
[105]J. Kietzer, A. Kaurs, and B. Levin, "A V-band communication transmitter and receiver system using dielectric waveguide integrated circuits," IEEE Trans. Microwave Theory Tech. **24**, 797–803 (1976).
[106]D. Headland, Y. Monnai, D. Abbott, C. Fumeaux, and W. Withayachumnankul, "Tutorial: Terahertz beamforming, from concepts to realizations," APL Photonics **3**, 051101 (2018).
[107]G. Kramer, M. De Andrade, R. Roy, and P. Chowdhury, "Evolution of optical access networks: Architectures and capacity upgrades," Proc. IEEE **100**, 1188–1196 (2012).
[108]P. E. Green, "Fiber to the home: The next big broadband thing," IEEE Commun. Mag. **42**, 100–106 (2004).
[109]W. Klaus, P. J. Winzer, and K. Nakajima, "The role of parallelism in the evolution of optical fiber communication systems," Proc. IEEE **110**, 1619–1654 (2022).
[110]M. Smit, K. Williams, and J. van der Tol, "Past, present, and future of InP-based photonic integration," APL Photonics **4**, 050901 (2019).
[111]P. Drude, "Zur elektronentheorie der metalle," Ann. Phys. **306**, 566–613 (1900).
[112]T.-I. Jeon and D. Grischkowsky, "Nature of conduction in doped silicon," Phys. Rev. Lett. **78**, 1106 (1997).
[113]D. Hashimshony, I. Geltner, G. Cohen, Y. Avitzour, A. Zigler, and C. Smith, "Characterization of the electrical properties and thickness of thin epitaxial semiconductor layers by THz reflection spectroscopy," J. Appl. Phys. **90**, 5778–5781 (2001).
[114]D. Pines and D. Bohm, "A collective description of electron interactions: II. Collective vs individual particle aspects of the interactions," Phys. Rev. **85**, 338 (1952).
[115]M. A. Ordal, R. J. Bell, R. W. Alexander, L. L. Long, and M. R. Querry, "Optical properties of fourteen metals in the infrared and far infrared: Al, Co, Cu, Au, Fe, Pb, Mo, Ni, Pd, Pt, Ag, Ti, V, and W," Appl. Opt. **24**, 4493–4499 (1985).
[116]S. Lucyszyn, "Evaluating surface impedance models for terahertz frequencies at room temperature," PIERS Online **3**, 554–559 (2007).

27 October 2023 05:17:16

© Author(s) 2023

[117]J. Dai, J. Zhang, W. Zhang, and D. Grischkowsky, "Terahertz time-domain spectroscopy characterization of the far-infrared absorption and index of refraction of high-resistivity, float-zone silicon," J. Opt. Soc. Am. B **21**, 1379–1386 (2004).
[118]G. Baccarani and P. Ostoja, "Electron mobility empirically related to the phosphorus concentration in silicon," Solid State Electron. **18**, 579–580 (1975).
[119]D. Headland, S. Nirantar, W. Withayachumnankul, P. Gutruf, D. Abbott, M. Bhaskaran, C. Fumeaux, and S. Sriram, "Terahertz magnetic mirror realized with dielectric resonator antennas," Adv. Mater. **27**, 7137–7144 (2015).
[120]T. W. Crowe, W. L. Bishop, D. W. Porterfield, J. L. Hesler, and R. M. Weikle, "Opening the terahertz window with integrated diode circuits," IEEE J. Solid-State Circuits **40**, 2104–2110 (2005).
[121]T. W. Crowe, B. Foley, S. Durant, K. Hui, Y. Duan, and J. L. Hesler, "VNA frequency extenders to 1.1 THz," in *Proceedings of the International Conference on Infrared, Millimeter, and Terahertz Waves* (IEEE, 2011).
[122]J. L. Hesler, W. R. Hall, T. W. Crowe, R. Weikle, B. Deaver, R. F. Bradley, and S.-K. Pan, "Fixed-tuned submillimeter wavelength waveguide mixers using planar Schottky-barrier diodes," IEEE Trans. Microwave Theory Tech. **45**, 653–658 (1997).
[123]H. Li, A. R. Kerr, J. L. Hesler, H. Xu, and R. M. Weikle, "A ring-centered waveguide flange for millimeter- and submillimeter-wave applications," in *Proceedings of the International Microwave Symposium* (IEEE, 2010), pp. 604–607.
[124]D. M. Pozar, *Microwave Engineering* (John Wiley & Sons, 2011).
[125]IEEE standard for rectangular metallic waveguides and their interfaces for frequencies of 110 GHz and above–Part 1: Frequency bands and waveguide dimensions," IEEE Std 1785.1-2012 (2013).
[126]N. Ridler and R. Ginleyt, "A review of the IEEE 1785 standards for rectangular waveguides above 110 GHz," in *Proceedings of the ARFTG Microwave Measurement Conference* (IEEE, 2017).
[127]I. Stil, A. Fontana, B. Lefranc, A. Navarrini, P. Serres, and K. Schuster, "Loss of WR10 waveguide across 70–116 GHz," in Proceedings of the International Symposium on Space Terahertz Technology, 2012.
[128]B. Zhang and H. Zirath, "Metallic 3-D printed rectangular waveguides for millimeter-wave applications," IEEE Trans. Compon., Packag., Manuf. Technol. **6**, 796–804 (2016).
[129]P. Kirby, D. Pukala, H. Manohara, I. Mehdi, and J. Papapolymerou, "Characterization of micromachined silicon rectangular waveguide at 400 GHz," IEEE Microwave Wireless Compon. Lett. **16**, 366–368 (2006).
[130]C. Jung-Kubiak, T. J. Reck, J. V. Siles, R. Lin, C. Lee, J. Gill, K. Cooper, I. Mehdi, and G. Chattopadhyay, "A multistep DRIE process for complex terahertz waveguide components," IEEE Trans. Terahertz Sci. Technol. **6**, 690–695 (2016).
[131]T. J. Reck, C. Jung-Kubiak, J. Gill, and G. Chattopadhyay, "Measurement of silicon micromachined waveguide components at 500–750 GHz," IEEE Trans. Terahertz Sci. Technol. **4**, 33–38 (2014).
[132]W. Otter, N. Ridler, H. Yasukochi, K. Soeda, K. Konishi, J. Yumoto, M. Kuwata-Gonokami, and S. Lucyszyn, "3D printed 1.1 THz waveguides," Electron. Lett. **53**, 471–473 (2017).
[133]S. Liu, J. Hu, Y. Zhang, Z. Zheng, Y. Liu, R. Xu, and Q. Xue, "1 THz micromachined waveguide band-pass filter," J. Infrared, Millimeter, Terahertz Waves **37**, 435–447 (2016).
[134]B. B. Yang, M. Kirley, and J. H. Booske, "Theoretical and empirical evaluation of surface roughness effects on conductivity in the terahertz regime," IEEE Trans. Terahertz Sci. Technol. **4**, 368–375 (2014).
[135]M. Kirley and J. H. Booske, "Terahertz conductivity of copper surfaces," IEEE Trans. Terahertz Sci. Technol. **5**, 1012–1020 (2015).
[136]Y. Nishida, N. Nishigami, S. Diebold, J. Kim, M. Fujita, and T. Nagatsuma, "Terahertz coherent receiver using a single resonant tunnelling diode," Sci. Rep. **9**, 18125 (2019).
[137]X. Yu, J.-Y. Kim, M. Fujita, and T. Nagatsuma, "Efficient mode converter to deep-subwavelength region with photonic-crystal waveguide platform for terahertz applications," Opt. Express **27**, 28707–28721 (2019).
[138]X. Yu, T. Ohira, J.-Y. Kim, M. Fujita, and T. Nagatsuma, "Waveguide-input resonant tunnelling diode mixer for THz communications," Electron. Lett. **56**, 342–344 (2020).
[139]S. Iwamatsu, Y. Nishida, M. Fujita, and T. Nagatsuma, "Terahertz coherent oscillator integrated with slot-ring antenna using two resonant tunneling diodes," Appl. Phys. Express **14**, 034001 (2021).
[140]K. J. Herrick, T. A. Schwarz, and L. P. Katehi, "Si-micromachined coplanar waveguides for use in high-frequency circuits," IEEE Trans. Microwave Theory Tech. **46**, 762–768 (1998).
[141]L. Cao, A.-S. Grimault-Jacquin, N. Zerounian, and F. Aniel, "Design and VNA-measurement of coplanar waveguide (CPW) on benzocyclobutene (BCB) at THz frequencies," Infrared Phys. Technol. **63**, 157–164 (2014).
[142]N. Zerounian, W. Aouimeur, A.-S. Grimault-Jacquin, G. Ducournau, C. Gaquière, and F. Aniel, "Coplanar waveguides on BCB measured up to 760 GHz," J. Electromagn. Waves Appl. **35**, 2051–2061 (2021).
[143]M. de Dood, A. Polman, T. Zijlstra, and E. van der Drift, "Amorphous silicon waveguides for microphotonics," J. Appl. Phys. **92**, 649–653 (2002).
[144]A. K. Mukherjee, M. Xiang, and S. Preu, "Broadband terahertz photonic integrated circuit with integrated active photonic devices," Photonics **8**, 492 (2021).
[145]H. Amarloo, N. Ranjkesh, and S. Safavi-Naeini, "Terahertz silicon–BCB–quartz dielectric waveguide: An efficient platform for compact THz systems," IEEE Trans. Terahertz Sci. Technol. **8**, 201–208 (2018).
[146]N. Ranjkesh, S. Gigoyan, H. Amarloo, M. Basha, and S. Safavi-Naeini, "Broadband single-mode THz suspended silicon-on-glass waveguide," IEEE Microwave Wireless Compon. Lett. **28**, 185–187 (2018).
[147]H. Amarloo and S. Safavi-Naeini, "Terahertz line defect waveguide based on silicon-on-glass technology," IEEE Trans. Terahertz Sci. Technol. **7**, 433–439 (2017).
[148]N. Ranjkesh, H. Amarloo, S. Gigoyan, N. Ghafarian, M. A. Basha, and S. Safavi-Naeini, "1.1 THz U-silicon-on-glass (U-SOG) waveguide: A low-loss platform for THz high-density integrated circuits," IEEE Trans. Terahertz Sci. Technol. **8**, 702–709 (2018).
[149]N. Ranjkesh, M. Basha, A. Taeb, A. Zandieh, S. Gigoyan, and S. Safavi-Naeini, "Silicon-on-glass dielectric waveguide—Part I: For millimeter-wave integrated circuits," IEEE Trans. Terahertz Sci. Technol. **5**, 268–279 (2015).
[150]R. Soref and J. Lorenzo, "Single-crystal silicon: A new material for 1.3 and 1.6 μm integrated-optical components," Electron. Lett. **21**, 953–954 (1985).
[151]R. Soref, "The past, present, and future of silicon photonics," IEEE J. Sel. Top. Quantum Electron. **12**, 1678–1687 (2006).
[152]A. Malekabadi, S. A. Charlebois, D. Deslandes, and F. Boone, "High-resistivity silicon dielectric ribbon waveguide for single-mode low-loss propagation at F/G-bands," IEEE Trans. Terahertz Sci. Technol. **4**, 447–453 (2014).
[153]K. Tsuruda, M. Fujita, and T. Nagatsuma, "Extremely low-loss terahertz waveguide based on silicon photonic-crystal slab," Opt. Express **23**, 31977–31990 (2015).
[154]W. Gao, W. S. Lee, X. Yu, M. Fujita, T. Nagatsuma, C. Fumeaux, and W. Withayachumnankul, "Characteristics of effective-medium-clad dielectric waveguides," IEEE Trans. Terahertz Sci. Technol. **11**, 28–41 (2021).
[155]R. Koala, R. Maru, K. Iyoda, L. Yi, M. Fujita, and T. Nagatsuma, "Ultra-low-loss and broadband all-silicon dielectric waveguides for WR-1 band (0.75–1.1 THz) modules," Photonics **9**, 515 (2022).
[156]S. Atakaramians, S. Afshar V, B. M. Fischer, D. Abbott, and T. M. Monro, "Porous fibers: A novel approach to low loss THz waveguides," Opt. Express **16**, 8845–8854 (2008).
[157]K. Nielsen, H. K. Rasmussen, A. J. Adam, P. C. Planken, O. Bang, and P. U. Jepsen, "Bendable, low-loss Topas fibers for the terahertz frequency range," Opt. Express **17**, 8592–8601 (2009).
[158]V. Setti, L. Vincetti, and A. Argyros, "Flexible tube lattice fibers for terahertz applications," Opt. Express **21**, 3388–3399 (2013).
[159]S. Atakaramians, S. Afshar V, T. M. Monro, and D. Abbott, "Terahertz dielectric waveguides," Adv. Opt. Photonics **5**, 169–215 (2013).
[160]X. Yu, T. Miyamoto, K. Obata, Y. Hosoda, J.-Y. Kim, M. Fujita, and T. Nagatsuma, "Direct terahertz communications with wireless and fiber links," in *Proceedings of the International Conference on Infrared, Millimeter, and Terahertz Waves* (IEEE, 2019).
[161]A. V. Mazur and M. M. Gasik, "Thermal expansion of silicon at temperatures up to 1100 °C," J. Mater. Process. Technol. **209**, 723–727 (2009).

27 October 2023 05:17:16

© Author(s) 2023

[162]G. A. Slack, "Nonmetallic crystals with high thermal conductivity," J. Phys. Chem. Solids **34**, 321–335 (1973).
[163]M. Offenberg, F. Larmer, B. Elsner, H. Munzel, and W. Riethmuller, "Novel process for a monolithic integrated accelerometer," in *Proceedings of the International Solid-State Sensors and Actuators Conference* (IEEE, 1995), Vol. 1, pp. 589–592.
[164]F. Laerme, A. Schilp, K. Funk, and M. Offenberg, "Bosch deep silicon etching: Improving uniformity and etch rate for advanced MEMS applications," in *Proceedings of the International Conference on Micro Electro Mechanical Systems* (IEEE, 1999), pp. 211–216.
[165]F. Laermer and A. Urban, "Challenges, developments and applications of silicon deep reactive ion etching," Microelectron. Eng. **67–68**, 349–355 (2003).
[166]W. Noell, P.-A. Clerc, S. Jeanneret, A. Hoogerwerf, P. Niedermann, A. Perret, and N. de Rooij, "MEMS for a watches," in *Proceedings of the International Conference on Micro Electro Mechanical Systems* (IEEE, 2004).
[167]Y. Fu, G. Ma, and R. Du, "Design and optimization of silicon bridges in a tourbillon watch," in *Proceedings of the International Conference on Mechatronics and Automation* (IEEE, 2014), pp. 84–89.
[168]H. J. Gardeniers, R. Luttge, E. J. Berenschot, M. J. de Boer, S. Y. Yeshurun, M. Hefetz, R. van't Oever, and A. van den Berg, "Silicon micromachined hollow microneedles for transdermal liquid transport," J. Microelectromech. Syst. **12**, 855–862 (2003).
[169]Z. Ma, S. M. Hanham, P. Albella, B. Ng, H. T. Lu, Y. Gong, S. A. Maier, and M. Hong, "Terahertz all-dielectric magnetic mirror metasurfaces," ACS Photonics **3**, 1010–1018 (2016).
[170]D. Headland, E. Carrasco, S. Nirantar, W. Withayachumnankul, P. Gutruf, J. Schwarz, D. Abbott, M. Bhaskaran, S. Sriram, J. Perruisseau-Carrier, and C. Fumeaux, "Dielectric resonator reflectarray as high-efficiency nonuniform terahertz metasurface," ACS Photonics **3**, 1019–1026 (2016).
[171]W. S. Lee, R. T. Ako, M. X. Low, M. Bhaskaran, S. Sriram, C. Fumeaux, and W. Withayachumnankul, "Dielectric-resonator metasurfaces for broadband terahertz quarter- and half-wave mirrors," Opt. Express **26**, 14392–14406 (2018).
[172]G. Chattopadhyay, T. Reck, C. Lee, and C. Jung-Kubiak, "Micromachined packaging for terahertz systems," Proc. IEEE **105**, 1139–1150 (2017).
[173]A. A. Generalov, D. V. Lioubtchenko, J. A. Mallat, V. Ovchinnikov, and A. V. Räisänen, "Millimeter-wave power sensor based on silicon rod waveguide," IEEE Trans. Terahertz Sci. Technol. **2**, 623–628 (2012).
[174]A. Rivera-Lavado, S. Preu, L. E. García-Muñoz, A. Generalov, J. Montero-de Paz, G. Döhler, D. Lioubtchenko, M. Méndez-Aller, F. Sedlmeir, M. Schneidereit, H. G. L. Schwefel, S. Malzer, D. Segovia-Vargas, and A. Räisänen, "Dielectric rod waveguide antenna as THz emitter for photomixing devices," IEEE Trans. Antennas Propag. **63**, 882–890 (2015).
[175]X. Yu, J.-Y. Kim, M. Fujita, and T. Nagatsuma, "Highly stable terahertz resonant tunneling diode oscillator coupled to photonic-crystal cavity," in *Proceedings of the Asia-Pacific Microwave Conference* (IEEE, 2018), pp. 114–116.
[176]X. Yu, T. Miyamoto, K. Obata, J. Kim, M. Fujita, and T. Nagatsuma, "Direct terahertz communications with wireless and fiber links," in *Proceedings of the International Conference on Infrared, Millimeter, and Terahertz Waves* (IEEE, 2019).
[177]A. E. Torres-García, J. M. Pérez-Escudero, J. Teniente, R. Gonzalo, and I. Ederra, "Silicon integrated subharmonic mixer on a photonic-crystal platform," IEEE Trans. Terahertz Sci. Technol. **11**, 79–89 (2021).
[178]X. Yu, D. J. Headland, Y. Nishida, R. A. Koala, J. Kim, M. Fujita, and T. Nagatsuma, "Hybrid integration between resonant tunneling diodes and unclad microphotonic diplexer for dual-channel coherent terahertz receiver," IEEE J. Sel. Top. Quantum Electron. **28**, 8500210 (2022).
[179]D. J. Headland, Y. Nishida, X. Yu, M. Fujita, and T. Nagatsuma, "Terahertz oscillator chips backside-coupled to unclad microphotonics," IEEE J. Sel. Top. Quantum Electron. **29**, 8500111 (2023).
[180]T. Tamir, G. Griffel, and H. L. Bertoni, *Guided-Wave Optoelectronics: Device Characterization, Analysis, and Design* (Springer Science & Business Media, 2013).
[181]E. A. Marcatili, "Dielectric rectangular waveguide and directional coupler for integrated optics," Bell Syst. Tech. J. **48**, 2071–2102 (1969).
[182]W. J. Westerveld, S. M. Leinders, K. W. van Dongen, H. P. Urbach, and M. Yousefi, "Extension of Marcatili's analytical approach for rectangular silicon optical waveguides," J. Lightwave Technol. **30**, 2388–2401 (2012).
[183]J. W. Goodman, *Introduction to Fourier Optics*, 3rd ed. (Roberts and Company Publishers, 2005).
[184]T. Fukazawa, F. Ohno, and T. Baba, "Very compact arrayed-waveguide-grating demultiplexer using Si photonic wire waveguides," Jpn. J. Appl. Phys. **43**, L673 (2004).
[185]H. Takahashi, Y. Hibino, and I. Nishi, "Polarization-insensitive arrayed-waveguide grating wavelength multiplexer on silicon," Opt. Lett. **17**, 499–501 (1992).
[186]F. Horst, W. M. Green, B. J. Offrein, and Y. A. Vlasov, "Silicon-on-insulator echelle grating WDM demultiplexers with two stigmatic points," IEEE Photonics Technol. Lett. **21**, 1743–1745 (2009).
[187]D. Halliday and D. Kiely, "Dielectric-rod aerials," Proc. Inst. Electr. Eng., Part 3 **94**, 610–618 (1947).
[188]C. Chandler, "An investigation of dielectric rod as wave guide," J. Appl. Phys. **20**, 1188–1192 (1949).
[189]S. Kobayashi, R. Mittra, and R. Lampe, "Dielectric rod antennas of rectangular cross section," in *Proceedings of the Antennas and Propagation Society International Symposium* (IEEE, 1980), Vol. 18, pp. 27–30.
[190]D. Lioubtchenko, S. Dudorov, J. Mallat, J. Tuovinen, and A. Räisänen, "Low-loss sapphire waveguides for 75-110 GHz frequency range," IEEE Microwave Wireless Compon. Lett. **11**, 252–254 (2001).
[191]D. Kiely, "Dielectric aerials with shaped radiation pattern," Wireless Eng. **28**, 177–178 (1951).
[192]V. Sudramaniam, "Some investigations on dielectric rod waveguide-Part II," J. Indian Inst. Sci. **45**, 109–125 (1963).
[193]A. Elhawil, L. Zhang, J. Stiens, C. De Tandt, N.-A. Gotzen, G. Assche, and R. Vounckx, "A quasi-optical free-space method for dielectric constant characterization of polymer materials in mm-wave band," in *Proceedings of the Annual Symposium of the IEEE/LEOS Benelux Chapter* (IEEE, 2007), Vol. 66, pp. 187–190.
[194]T. Trinh, J. Malherbe, and R. Mittra, "A metal-to-dielectric waveguide transition with application to millimeter-wave integrated circuits," in *Proceedings of the International Microwave Symposium* (IEEE, 1980), pp. 205–207.
[195]D. V. Lioubtchenko, S. N. Dudorov, and A. V. Räisänen, "Development of rectangular open dielectric waveguide sections for the frequency range of 75-110 GHz," in *Proceedings of the European Microwave Conference* (IEEE, 2001).
[196]S. Pal and C. Jacob, "Silicon—A new substrate for GaN growth," Bull. Mater. Sci. **27**, 501–504 (2004).
[197]J. Pousi, D. V. Lioubtchenko, S. N. Dudorov, J. A. Mallat, and A. Räisänen, "High permittivity dielectric rod waveguide antenna for 110-150 GHz," in *Proceedings of the European Conference on Antennas and Propagation* (IEEE, 2006).
[198]A. Generalov, D. Lioubtchenko, and A. V. Räisänen, "Dielectric rod waveguide antenna for 220–325 GHz," in *Proceedings of the European Conference on Antennas and Propagation* (IEEE, 2012), pp. 3551–3553.
[199]A. M. Marconnet, M. M. He, S. Sengele, S.-J. Ho, H. Jiang, N. J. Ferrier, D. W. van der Weide, V. Madhavan, N. Nelson, and J. H. Booske, "Microfabricated silicon high-frequency waveguide couplers and antennas," IEEE Trans. Electron Devices **56**, 721–729 (2009).
[200]J. P. Pousi, S. Dudorov, D. Lioubtchenko, and A. Räisänen, "Frequency selective coupler for W band based on power transfer in dielectric rod waveguides," in *Proceedings of the Fourth European Conference on Antennas and Propagation* (IEEE, 2010).
[201]D. Chicherin, M. Sterner, D. Lioubtchenko, J. Oberhammer, and A. V. Räisänen, "Analog-type millimeter-wave phase shifters based on MEMS tunable high-impedance surface and dielectric rod waveguide," Int. J. Microwave Wireless Technol. **3**, 533–538 (2011).
[202]M. Verstuyft, E. Akiki, M. Vanwolleghem, G. Ducournau, J.-F. Lampin, B. Walter, F. Bavedila, É. Lebouvier, M. Faucher, and B. Kuyken, "Short bends using curved mirrors in silicon waveguides for terahertz waves," Opt. Express **30**, 6656–6670 (2022).
[203]E. Akiki, M. Verstuyft, B. Kuyken, B. Walter, M. Faucher, J.-F. Lampin, G. Ducournau, and M. Vanwolleghem, "High-*Q* THz photonic crystal cavity on a

27 October 2023 05:17:16

© Author(s) 2023

low-loss suspended silicon platform," IEEE Trans. Terahertz Sci. Technol. **11**, 42–53 (2021).
[204]S. M. Hanham, M. M. Ahmad, S. Lucyszyn, and N. Klein, "LED-switchable high-*Q* packaged THz microbeam resonators," IEEE Trans. Terahertz Sci. Technol. **7**, 199–208 (2017).
[205]E. Yablonovitch, T. Gmitter, R. Meade, A. Rappe, K. Brommer, and J. Joannopoulos, "Donor and acceptor modes in photonic band structure," Phys. Rev. Lett. **67**, 3380 (1991).
[206]M. Fujita, S. Takahashi, Y. Tanaka, T. Asano, and S. Noda, "Simultaneous inhibition and redistribution of spontaneous light emission in photonic crystals," Science **308**, 1296–1298 (2005).
[207]E. Özbay, J. Bostak, D. M. Bloom, E. Michel, G. Tuttle, R. Biswas, and K. M. Ho, "Terahertz spectroscopy of three-dimensional photonic band-gap crystals," Opt. Lett. **19**, 1155–1157 (1994).
[208]C. Yee, N. Jukam, and M. Sherwin, "Transmission of single mode ultrathin terahertz photonic crystal slabs," Appl. Phys. Lett. **91**, 194104 (2007).
[209]P. M. Morse, "The quantum mechanics of electrons in crystals," Phys. Rev. **35**, 1310–1324 (1930).
[210]E. Yablonovitch, "Inhibited spontaneous emission in solid-state physics and electronics," Phys. Rev. Lett. **58**, 2059 (1987).
[211]S. John, "Strong localization of photons in certain disordered dielectric superlattices," Phys. Rev. Lett. **58**, 2486 (1987).
[212]T. F. Krauss, R. M. Rue, and S. Brand, "Two-dimensional photonic-bandgap structures operating at near-infrared wavelengths," Nature **383**, 699–702 (1996).
[213]M. Kanskar, P. Paddon, V. Pacradouni, R. Morin, A. Busch, J. F. Young, S. Johnson, J. MacKenzie, and T. Tiedje, "Observation of leaky slab modes in an air-bridged semiconductor waveguide with a two-dimensional photonic lattice," Appl. Phys. Lett. **70**, 1438–1440 (1997).
[214]S. Noda, M. Fujita, and T. Asano, "Spontaneous-emission control by photonic crystals and nanocavities," Nat. Photonics **1**, 449–458 (2007).
[215]C.-C. Cheng and A. Scherer, "Fabrication of photonic band-gap crystals," J. Vac. Sci. Technol. B **13**, 2696–2700 (1995).
[216]J. D. Joannopoulos, P. R. Villeneuve, and S. Fan, "Photonic crystals: Putting a new twist on light," Nature **386**, 143–149 (1997).
[217]T. F. Krauss and M. Richard, "Photonic crystals in the optical regime—Past, present and future," Progr. Quantum Electron. **23**, 51–96 (1999).
[218]T. Baba, "Slow light in photonic crystals," Nat. Photonics **2**, 465–473 (2008).
[219]M. Wada, Y. Doi, K. Inoue, and J. Haus, "Far-infrared transmittance and band-structure correspondence in two-dimensional air-rod photonic crystals," Phys. Rev. B **55**, 10443 (1997).
[220]Z. Jian, J. Pearce, and D. M. Mittleman, "Two-dimensional photonic crystal slabs in parallel-plate metal waveguides studied with terahertz time-domain spectroscopy," Semicond. Sci. Technol. **20**, S300 (2005).
[221]T. Ishigaki, M. Fujita, M. Nagai, M. Ashida, and T. Nagatsuma, "Photonic-crystal slab for terahertz-wave integrated circuits," in *Proceedings of the Photonics Conference* (IEEE, 2012), pp. 774–775.
[222]R. Kakimi, M. Fujita, M. Nagai, M. Ashida, and T. Nagatsuma, "Capture of a terahertz wave in a photonic-crystal slab," Nat. Photonics **8**, 657–663 (2014).
[223]Y. Kujime, M. Fujita, and T. Nagatsuma, "Terahertz tag using photonic-crystal slabs," J. Lightwave Technol. **36**, 4386–4392 (2018).
[224]W. Shockley, "The quantum physics of solids, I. The energies of electrons in crystals," Bell Syst. Tech. J. **18**, 645–723 (1939).
[225]W. Shockley, "Energy band structures in semiconductors," Phys. Rev. **78**, 173 (1950).
[226]E. Yablonovitch and T. Gmitter, "Photonic band structure: The face-centered-cubic case," Phys. Rev. Lett. **63**, 1950 (1989).
[227]E. Yablonovitch, "Photonic band structure," in *Photonic Band Gaps and Localization* (Springer, 1993), pp. 207–234.
[228]F. Bloch, "Über die quantenmechanik der elektronen in kristallgittern," Z. Phys. **52**, 555–600 (1929).
[229]A. S. Phani, J. Woodhouse, and N. Fleck, "Wave propagation in two-dimensional periodic lattices," J. Acoust. Soc. Am. **119**, 1995–2005 (2006).
[230]J. D. Joannopoulos, S. G. Johnson, J. N. Winn, and R. D. Meade, *Photonic Crystals: Molding the Flow of Light*, 2nd ed. (Princeton University Press, 2008).
[231]R. D. Meade, A. Devenyi, J. Joannopoulos, O. Alerhand, D. Smith, and K. Kash, "Novel applications of photonic band gap materials: Low-loss bends and high *Q* cavities," J. Appl. Phys. **75**, 4753–4755 (1994).
[232]T. Baba, N. Fukaya, and J. Yonekura, "Observation of light propagation in photonic crystal optical waveguides with bends," Electron. Lett. **35**, 654–655 (1999).
[233]S. G. Johnson, P. R. Villeneuve, S. Fan, and J. D. Joannopoulos, "Linear waveguides in photonic-crystal slabs," Phys. Rev. B **62**, 8212 (2000).
[234]M. Fujita, T. Nagatsuma, T. Ishigaki, D. Onishi, and E. Miyai, "Terahertz-wave connector and terahertz-wave integrated circuits, and wave guide and antenna structure," U.S. patent 9,188,742 (September 4, 2015).
[235]D. Headland, X. Yu, M. Nagai, M. Fujita, and T. Nagatsuma, "Packaged dish antenna for wireless terahertz photonic crystal waveguide devices," in *Proceedings of the International Symposium on Antennas and Propagation* (IEEE, 2021), pp. 15–16.
[236]A. Suminokura, T. Ishigaki, M. Fujita, and T. Nagatsuma, "Grating coupler for terahertz-wave integrated circuits," in *Proceedings of the Asia-Pacific Radio Science Conference* (URSI, 2013).
[237]T. Nagatsuma, S. Hisatake, M. Fujita, H. H. N. Pham, K. Tsuruda, S. Kuwano, and J. Terada, "Millimeter-wave and terahertz-wave applications enabled by photonics," IEEE J. Quantum Electron. **52**, 0600912 (2016).
[238]W. Withayachumnankul, R. Yamada, C. Fumeaux, M. Fujita, and T. Nagatsuma, "All-dielectric integration of dielectric resonator antenna and photonic crystal waveguide," Opt. Express **25**, 14706–14714 (2017).
[239]D. Headland, X. Yu, M. Fujita, and T. Nagatsuma, "Near-field out-of-plane coupling between terahertz photonic crystal waveguides," Optica **6**, 1002–1011 (2019).
[240]X. Yu, M. Sugeta, Y. Yamagami, M. Fujita, and T. Nagatsuma, "Simultaneous low-loss and low-dispersion in a photonic-crystal waveguide for terahertz communications," Appl. Phys. Express **12**, 012005 (2019).
[241]D. Headland, M. Fujita, and T. Nagatsuma, "Bragg-mirror suppression for enhanced bandwidth in terahertz photonic crystal waveguides," IEEE J. Sel. Top. Quantum Electron. **26**, 4900109 (2020).
[242]Y. Yamagami, X. Yu, A. Kumar, P. Pitchappa, R. Sing, M. Fujita, and T. Nagatsuma, "Ultralow-loss branch waveguide using valley photonic crystals," in Proceedings of the JSAP Autumn Meeting, 2019.
[243]J. Webber, Y. Yamagami, G. Ducournau, P. Szriftgiser, K. Iyoda, M. Fujita, T. Nagatsuma, and R. Singh, "Terahertz band communications with topological valley photonic crystal waveguide," J. Lightwave Technol. **39**, 7609–7620 (2021).
[244]Y.-L. Hong, G.-H. Tang, R.-W. Peng, R.-H. Fan, Z.-L. Ma, Z. Wang, Y. Jiang, L.-D. Chen, and M. Wang, "Direct observation of terahertz topological valley transport," Opt. Express **30**, 14839–14850 (2022).
[245]A. Kumar, M. Gupta, P. Pitchappa, N. Wang, M. Fujita, and R. Singh, "Terahertz topological photonic integrated circuits for 6G and beyond: A perspective," J. Appl. Phys. **132**, 140901 (2022).
[246]H. Yoshimi, T. Yamaguchi, R. Katsumi, Y. Ota, Y. Arakawa, and S. Iwamoto, "Experimental demonstration of topological slow light waveguides in valley photonic crystals," Opt. Express **29**, 13441–13450 (2021).
[247]C. A. Rosiek, G. Arregui, A. Vladimirova, M. Albrechtsen, B. Vosoughi Lahijani, R. E. Christiansen, and S. Stobbe, "Observation of strong backscattering in valley-Hall photonic topological interface modes," Nat. Photonics **17**, 386–392 (2023).
[248]A. V. Subashiev and S. Luryi, "Modal control in semiconductor optical waveguides with uniaxially patterned layers," J. Lightwave Technol. **24**, 1513 (2006).
[249]W. Gao, W. S. Lee, C. Fumeaux, and W. Withayachumnankul, "Effective-medium-clad Bragg grating filters," APL Photonics **6**, 076105 (2021).
[250]D. Headland, W. Withayachumnankul, M. Fujita, and T. Nagatsuma, "Unclad microphotonic waveguide bend," in *Proceedings of the International Conference on Infrared, Millimeter, and Terahertz Waves* (IEEE, 2020).
[251]H. Lees, W. Gao, and W. Withayachumnankul, "All-silicon, low-cross-talk terahertz waveguide crossing based on effective medium," Opt. Lett. **46**, 5469–5472 (2021).
[252]X. Jiang, H. Wu, and D. Dai, "Low-loss and low-crosstalk multimode waveguide bend on silicon," Opt. Express **26**, 17680–17689 (2018).

27 October 2023 05:17:16

© Author(s) 2023

[253]D. T. Moore, "Gradient-index optics: A review," Appl. Opt. **19**, 1035–1038 (1980).
[254]W. Withayachumnankul, R. Yamada, M. Fujita, and T. Nagatsuma, "All-dielectric rod antenna array for terahertz communications," APL Photonics **3**, 051707 (2018).
[255]J. Liang, W. Gao, H. Lees, and W. Withayachumnankul, "All-silicon terahertz planar horn antenna," IEEE Antennas Wireless Propag. Lett. **20**, 2181–2185 (2021).
[256]D. Headland and W. Withayachumnankul, "Continuous leakage from slow-wave structure for integrated all-dielectric uniform leaky wave antenna," in *Proceedings of the European Conference on Antennas and Propagation* (IEEE, 2022).
[257]D. Headland, A. K. Klein, M. Fujita, and T. Nagatsuma, "Dielectric slot-coupled half-Maxwell fisheye lens as octave-bandwidth beam expander for terahertz-range applications," APL Photonics **6**, 096104 (2021).
[258]D. Headland, M. Fujita, and T. Nagatsuma, "Half-Maxwell fisheye lens with photonic crystal waveguide for the integration of terahertz optics," Opt. Express **28**, 2366–2380 (2020).
[259]K. Okamoto, K. Tsuruda, S. Diebold, S. Hisatake, M. Fujita, and T. Nagatsuma, "Terahertz sensor using photonic crystal cavity and resonant tunneling diodes," J. Infrared, Millimeter, Terahertz Waves **38**, 1085–1097 (2017).
[260]P. Dechwechprasit, C. Fumeaux, and W. Withayachumnankul, "Integrated resonant cavities on substrateless terahertz dielectric waveguide platform," in *Proceedings of the International Conference on Infrared, Millimeter and Terahertz Waves* (IEEE, 2021).
[261]W. J. Otter, S. M. Hanham, N. M. Ridler, G. Marino, N. Klein, and S. Lucyszyn, "100GHz ultra-high Q-factor photonic crystal resonators," Sens. Actuators, A **217**, 151–159 (2014).
[262]S. Hanham, C. Watts, W. Otter, S. Lucyszyn, and N. Klein, "Dielectric measurements of nanoliter liquids with a photonic crystal resonator at terahertz frequencies," Appl. Phys. Lett. **107**, 032903 (2015).
[263]A. Kumar, M. Gupta, P. Pitchappa, Y. J. Tan, N. Wang, and R. Singh, "Topological sensor on a silicon chip," Appl. Phys. Lett. **121**, 011101 (2022).
[264]J. Xie, X. Zhu, X. Zang, Q. Cheng, L. Chen, and Y. Zhu, "Terahertz integrated device: High-Q silicon dielectric resonators," Opt. Mater. Express **8**, 50–58 (2018).
[265]S. Yuan, L. Chen, Z. Wang, W. Deng, Z. Hou, C. Zhang, Y. Yu, X. Wu, and X. Zhang, "On-chip terahertz isolator with ultrahigh isolation ratios," Nat. Commun. **12**, 5570 (2021).
[266]S. A. Hosseini Farahabadi, M. Entezami, H. Abouali, H. Amarloo, M. Poudineh, and S. Safavi-Naeini, "Sub-terahertz silicon-based on-chip absorption spectroscopy using thin-film model for biological applications," Sci. Rep. **12**, 17747 (2022).
[267]D. Headland, M. Ali, D. C. Gallego, and G. Carpintero, "Broadband liquid sensing of sealed microfluidic channel using mm-wave dielectric rod waveguide," in *Proceedings of the International Conference on Infrared, Millimeter, and Terahertz Waves* (IEEE, 2022).
[268]M. Fujita, "Photonic-crystal slab for terahertz-wave technology platform," Proc. SPIE **9757**, 97570W (2016).
[269]A. Kumar, M. Gupta, P. Pitchappa, T. C. Tan, U. Chattopadhyay, G. Ducournau, N. Wang, Y. Chong, and R. Singh, "Active ultrahigh-Q (0.2×10^6) THz topological cavities on a chip," Adv. Mater. **34**, 2202370 (2022).
[270]M. Yata, M. Fujita, and T. Nagatsuma, "Photonic-crystal diplexers for terahertz-wave applications," Opt. Express **24**, 7835–7849 (2016).
[271]A. Kumar, M. Gupta, P. Pitchappa, N. Wang, P. Szriftgiser, G. Ducournau, and R. Singh, "Phototunable chip-scale topological photonics: 160 Gbps waveguide and demultiplexer for THz 6G communication," Nat. Commun. **13**, 5404 (2022).
[272]N. Shibata, Y. Uemura, Y. Kawamoto, L. Yi, M. Fujita, and T. Nagatsuma, "Silicon dielectric diplexer module for 600-GHz-band frequency-division multiplexing wireless communication," IEEE Trans. Terahertz Sci. Technol. **12**, 334–344 (2022).
[273]X. Yu, R. Asif, M. Piels, D. Zibar, M. Galili, T. Morioka, P. U. Jepsen, and L. K. Oxenløwe, "400-GHz wireless transmission of 60-Gb/s Nyquist-QPSK signals using UTC-PD and heterodyne mixer," IEEE Trans. Terahertz Sci. Technol. **6**, 765–770 (2016).
[274]K. Takiguchi, "40 Gsymbol/s channel-based Nyquist wavelength division multiplexing communication in a terahertz-band using optical-domain reception signal processing," OSA Continuum **3**, 2308–2319 (2020).
[275]W. Withayachumnankul, M. Fujita, and T. Nagatsuma, "Integrated silicon photonic crystals toward terahertz communications," Adv. Opt. Mater. **6**, 1800401 (2018).
[276]K. Iyoda, M. Fujita, and T. Nagatsuma, "Terahertz multiplexers based on valley photonic crystals," in *Proceedings of the International Conference on Infrared, Millimeter and Terahertz Waves* (IEEE, 2022).
[277]Y. Kawamoto, T. Yoshioka, N. Shibata, D. Headland, M. Fujita, R. Koma, R. Igarashi, K. Hara, J.-i. Kani, and T. Nagatsuma, "300-GHz-band diplexer module for frequency-division multiplexed wireless communication," in IEICE Transactions on Electronics, 2023, Vol. E106-C.
[278]L. Mach, "Ueber einen interferenzrefraktor," Z. Intsrum. **12**, 89–93 (1892).
[279]L. Liao, D. Samara-Rubio, M. Morse, A. Liu, D. Hodge, D. Rubin, U. D. Keil, and T. Franck, "High speed silicon Mach-Zehnder modulator," Opt. Express **13**, 3129–3135 (2005).
[280]K. Murano, I. Watanabe, A. Kasamatsu, S. Suzuki, M. Asada, W. Withayachumnankul, T. Tanaka, and Y. Monnai, "Low-profile terahertz radar based on broadband leaky-wave beam steering," IEEE Trans. Terahertz Sci. Technol. **7**, 60–69 (2016).
[281]B. S.-Y. Ung, J. Li, H. Lin, B. M. Fischer, W. Withayachumnankul, and D. Abbott, "Dual-mode terahertz time-domain spectroscopy system," IEEE Trans. Terahertz Sci. Technol. **3**, 216–220 (2013).
[282]T. Sagisaka, R. Kaname, M. Kikuchi, N. Kukutsu, D. Headland, L. Yi, M. Fujita, and T. Nagatsuma, "Integrated terahertz optics with effective medium for 600-GHz-band imaging," in *Proceedings of the International Topical Meeting on Microwave Photonics* (IEEE, 2020), pp. 62–65.

27 October 2023 05:17:16

© Author(s) 2023